Dissertations   Theses and Dissertations

Spring 4-2017

The Development, Evaluation and Applications of a Neuromechanical Control Model of Human Locomotion

Seungmoon Song
Carnegie Mellon University

Follow this and additional works at: http://repository.cmu.edu/dissertations

The Development, Evaluation and Applications of a Neuromechanical Control Model of Human Locomotion

Seungmoon Song

CMU-RI-TR-17-24

April, 2017

*Submitted in partial fulfillment of the
requirements for the degree of
Doctor of Philosophy in Robotics*

Robotics Institute
Carnegie Mellon University
Pittsburgh, PA 15213

Thesis Committee:
Hartmut Geyer, Chair
Christopher G. Atkeson
Stelian Coros
Auke J. Ijspeert, EPFL

Abstract

The neural control of human locomotion is not fully understood. As current experimental techniques provide only partial and indirect access to the neural control network, our understanding remains fragmentary with large gaps between detectable neural circuits and measurable behavioral data. Neuromechanical simulation studies can help bridging these gaps. By testing a hypothesized controller in neuromechanical simulations, one can evaluate the plausibility of the controller and propose experimental studies which can further investigate the hypothesis. Better understanding the control of human locomotion will change the way we design rehabilitation treatment and engineer assistive devices.

This thesis first investigates how much of human locomotion control can be explained by spinal reflexes using neuromechanical simulations. It is known that the spinal control is essential in generating locomotion behaviors in humans, which leads to two central questions: "how does the lower layer controller in the spinal cord generate the motor stimulations?" and "how is this lower layer controller modulated by the higher layer brain control to realize different locomotion tasks?" To investigate these questions, we propose a hierarchical control model with two layers, where the lower-layer control consists of spinal reflexes, and the higher-layer sends a few commands to modulate this lower layer control. In neuromechanical simulations, this model can generate diverse human locomotion behaviors, including walking and running, adapting to slopes and stairs, and changing locomotion directions and speeds. Furthermore, its reactions to a range of unexpected disturbances during normal walking are remarkably similar to those observed in human experiments. The simulation results suggest following answers to the central questions: "the motor stimulations of many human locomotion behaviors can be generated by chains of reflexes" and "different locomotion behaviors can be realized by a reflex-based unified controller that is modulated by the higher-layer control."

The latter part of this thesis presents three studies of using the neuromechanical control model either as a simulation testbed for studying human locomotion or as a robotic controller for legged machines. First, the neuromechanical model is used to study human foot biomechanics. The walking simulations with different foot designs suggest that the windlass mechanism in human feet saves metabolic cost during walking, and this saving does not come from the compliance of the feet, which is one component of this mechanism. Second, the age-related skeletal, muscular, and neural changes are applied to the model to investigate why the metabolic cost increases and the regular walking speed reduces in elderly people. The increase of metabolic cost of the elderly model is mostly attributed to weakened muscles, and we find muscle fatigue as a plausible performance criterion that suggests slower walking speed for the elderly model. In the last study, we adapt the neuromechanical model for a bipedal robot ATRIAS. With the controller, ATRIAS could walk on a rough terrain with unknown height changes of $\pm$ 20 cm in a sagittal plane physics simulation.

Acknowledgments

Contents

List of Figures

List of Tables

List of Abbreviations

2D 2-dimensional. 23, 36, 40, 50, 51, 56, 115, 120

3D 3-dimensional. 2, 3, 21, 23–25, 49, 51, 114, 121

BE buffer elastic element. 28, 30, 31

BFSH short head of biceps femoris. 31, 46, 48, 52, 66

CE contractile element. 28, 30, 34, 38, 116

CMA-ES covariance matrix adaptation evolution strategy. 39–41, 67, 118

CNS central nervous system. 5, 6, 12

COM center of mass. 18, 23, 29, 44, 45, 49, 58, 113

COT cost of transport. 91, 98, 102, 104, 105, 107–111

CPG central pattern generator. 1, 2, 6, 7, 9–11, 14, 15, 19–23, 43, 59, 75, 84–87, 125, 126

DOF degree of freedom. 9, 11, 21, 31, 52, 56, 115

EMG electromyography. 13, 20, 22, 23, 52, 53, 77, 81

FOT fatigue of transport. 109–112

GAS gastrocnemius. 31, 46, 52, 66, 81, 84, 107

GLU glutei. 31, 46, 48, 65

GRF ground reaction force. 13, 18, 19, 36–38, 50, 119

GRM ground reaction moment. 14

H-reflex Hoffman reflex. 15–17

HAB hip abductor. 31, 46, 48, 53, 64

HAD hip adductor. 31, 46, 48, 51, 52, 64

HAM hamstring. 31, 46, 48, 53, 65, 87

HFL hip flexor. 31, 46, 48, 52, 58, 65

MLR mesencephalic locomotor region. 8

Chapter 1

Introduction

1.1 Problem Statement

The neural control of human locomotion is not fully understood. Locomotion is prevalently treated as a basic motor control task and is extensively studied in animals including humans [196, 205, 216, 229]. Fully understanding the control of human locomotion can have profound impacts across various fields. For instance, the understanding can lead us to new rehabilitation treatment and assistive devices. Furthermore, the knowledge of human locomotion control can be transferred to designing and controlling legged machines.

Much of our current knowledge about human locomotion control relies on experimental studies. However, due to the lack of experimental techniques that can identify full neural control networks, the knowledge remains fragmentary with large gaps between detectable neural circuits and measurable behavioral data. For instance, although different neural control mechanisms of the spinal cord, such as central pattern generators (CPGs) and reflex pathways, are observed in animal experiments, the specific roles and contributions of each mechanism remain unclear, especially in human locomotion control. Neuromechanical simulation studies may help to bridge these gaps. By neuromechanical simulations we mean physics simulations that model the human neuro-musculo-skeletal properties involved in locomotion. Control models hypothesized based

on experimental observations can be investigated in these neuromechanical simulations. Such investigations are useful in studying human locomotion since they allow to assess control results at the behavioral level which involve complex muscle and segment dynamics. For example, if a certain control algorithm inherently cannot generate stable walking it is unlikely that such control algorithm is encoded in the human neural network. Similarly, simulation studies may propose neural circuits, which seem to be necessary for realizing certain control function, as guides for experimental search.

However, existing computational neuromechanical models of human locomotion barely generate normal walking and have limited predictive ability. Only the most advanced models can generate steady walking and running in 3-dimensional (3D) [103], and how the models can be extended for diverse locomotion behaviors is not clear. In addition, few models generate human-like kinematics, dynamics and muscle activations for normal walking, which is probably a basic requirement as a predictive testbed. Moreover, most neuromechanical models consist of both CPGs and reflex circuits without analyzing the contributions of each control mechanism to the generation of locomotion behaviors [103, 247].

1.2 Approach

This thesis investigates how much of the control of human locomotion can be explained with spinal reflexes. Although CPGs are often assumed to play important roles in human locomotion, it is not clear if they even exist in humans [24, 156, 187]. On the other hand, the responses against unexpected disturbances within a short time delay clearly show the existence of spinal reflexes, and that these responses change in different locomotion phases and tasks suggest that the reflex pathways are modulated in a functionally useful way [38, 231]. However, the specific functionalities of each reflex pathway remain speculative, and how the interplay of different reflex pathways contributes in the overall locomotion behaviors is not understood. In this thesis, a spinal control network consisting of solely reflex pathways is proposed, and how much of

human locomotion behaviors can be generated and predicted by the proposed model is tested.

To this end, a previously proposed sagittal plane reflex-based model [88] is extended into 3D with a neural control circuitry organized in 10 functional spinal-reflex modules. It is first tested whether the control parameters optimized for energy efficient walking, which is widely accepted as a primary criterion of human locomotion [3, 287], result in kinematics, dynamics and muscle activations observed in normal human walking. Furthermore, the capability of the proposed model in explaining diverse human locomotion behaviors is assessed by optimizing the control parameters in different environments and for different locomotion tasks. The plausibility of the proposed model is further investigated by comparing its reactions to a range of unexpected disturbances with those of humans during normal walking.

In addition, this thesis presents three example studies of using the neuromechanical model: two studies use the model as simulation testbeds for studying human locomotion and one study adapts the model to control a bipedal robot. In the first study, the model is used to study human foot biomechanics. The model is adapted to walk with different biomechanical foot designs, and the resulting energetic costs are analyzed. The second study investigates the physiological origin of elderly gait. Age-related skeletal, muscular and neural properties are applied to the model, and the resulting simulations are analyzed to explain why the metabolic cost during walking increases and the preferred walking speed reduces in elderly people. The last study adapts the neuromechanical model to a locomotion controller for bipedal robots. The robustness of the adapted controller, which maps the neuromechanical model to a robot topology and emulates it to generate desired motor torques, is investigated in a high-fidelity simulation of the bipedal robot ATRIAS.

1.3 Contributions

This thesis proposes a neuromechanical control model that can explain diverse human locomotion behaviors, evaluates the plausibility of the proposed model using a range of unexpected

3

disturbances, and demonstrate how the model can be adapted to a simulation testbed for studying humans and to a robotic controller for leg machines. To our knowledge, the presented model is so far the only neuromechanical control model that demonstrates such diverse locomotion behaviors and is evaluated by its responses against a range of unexpected disturbances. Moreover, the studies of using the model as simulation testbeds provide scientific insights into human foot biomechanics and elderly gait performance, and the adaptation of the model into a robotic controller provides an alternative locomotion controller for legged machines. More implications are discussed in Chapter 7.

1.4   Thesis Overview

We first review what is known about human locomotion motor control and explain how neuromechanical modeling studies may contribute to extending our knowledge (Chapter 2). Then, we describe our human neuromechanical simulation environment, including the human musculoskeletal model and the control parameter optimization process (Chapter 3). In this simulation environment, we propose a neuromechanical control model that can generate diverse locomotion behaviors of humans (Chapter 4). We further investigate the plausibility of this control model by comparing its reactions to a range of unexpected disturbances with those of humans during walking (Chapter 5). Next, we present how we use this neuromechanical model as simulation testbeds to study the effects of changes in different physiological properties to gait and as a robotic controller for legged machines (Chapter 6). Finally, we conclude this thesis by summarizing the studies and discussing their contributions (Chapter 7).

Chapter 2

Background

The central question of this thesis for developing human locomotion control is "**how does the neural control system of humans generate the muscle activation stimulations for locomotion?**" Since locomotion is a basic motor control task for animals and is considered to involve the fundamental mechanisms of the central nervous system (CNS), the neural control of locomotion in a number of species has been extensively studied. For some species with relatively simple neural systems, such as certain mollusks, the neural locomotion controllers have been investigated at the behavioral and the circuitry levels [196]. However, understanding the motor control at the circuitry level and interpreting the role of each circuit at the behavioral level are difficult in more complex species, such as humans. Therefore, much of our knowledge about the locomotion control of humans relies on extrapolating from what is known in simpler animals [39, 196].

This chapter reviews the current understanding and computational models of human locomotion. Section 2.1 reviews the basic neural control mechanisms observed in animal experiments, and Section 2.2 explains how these mechanisms extrapolate to human locomotion control. Most of the current knowledge on the locomotion control of animals and humans relies on experimental studies and has large gaps between detectable neural circuits and measurable gait data. Section 2.3 introduces computer simulation studies of neural control models, including the model

this thesis presents, which may be used to bridge these gaps.

2.1 Observations of Neural Controls in Animals

The current understanding of neural controls in animals is reviewed in this section. First, experimental studies on a marine mollusk, Clione limacina, is reviewed as an example of a detailed investigation from the cellular level to the behavior level of the locomotion control in a simple animal (Sec. 2.1.1). In more complex animals, however, such detailed investigation is not feasible, and many aspects of the neural locomotion control remain unexplained. Still, some structural and basic components of the locomotion control seem to be shared in many animals, which are explained in the following sections. It is explained that the locomotion controllers in most animals can be interpreted as a hierarchical structure that consists of two layers (Sec. 2.1.2). Then are explained the neural control mechanisms that are considered as the basic components of the lower layer of the locomotion controllers: reflexes, CPGs, and muscle synergies (Sec. 2.1.3 and Sec. 2.1.4).

2.1.1 Experimental Studies in Cliones

The swimming control of the *Clione limacina*, a few centimeters long marine mollusk (Fig. 2.1-A), has been thoroughly studied at the behavioral and the circuitry levels. *Only* a few hundred neurons of a Clione's CNS participate in the control, which allows researchers to experimentally investigate the control system in detail [196]. Experiments in Cliones have been conducted with intact animals, whole animal preparations, and isolated groups of neurons and individual neurons. For example of experiments with intact animals, it is observed that a mechanical disturbance on the tail stimulates the locomotion system to increase the swimming speed, which is known as the escape reaction [19]. In experiments at more detailed level, individual neuron activations are probed with microelectrodes while other neurons were electrically stimulated to

A. Clione limacina   B. Whole-animal preparation   C. Isolated ganglia
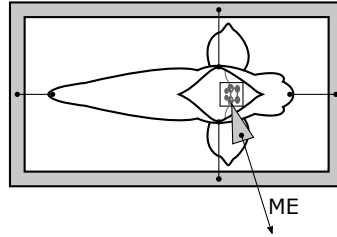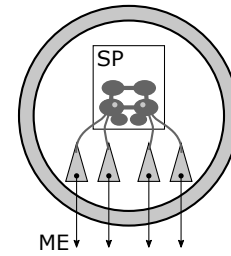
Figure 2.1: Experimental studies in Cliones. Clione is a few centimeters long marine mollusk (A, adapted from [50]). The swimming control of Cliones have been conducted both in *in vivo* (B, adapted from [15]) and *in vitro* (C, adapted from [60]). (ME: microelectrode; SP: supporting platform)

test the properties of each neuron and their connections; these experiments are conducted in restrained Cliones with the body cavity opened (Fig. 2.1-B) and in isolated ganglia (Fig. 2.1-C). For instance, Arshavsky et al. measured the activations of 400 individual neurons on the surface of each pedal ganglion and found that about 60 neurons show rhythmic activities as the swim cycle and about 20 of them are efferent (motor) neurons [16]. Other experimental methods include inactivating selected neurons with photoinactivation [17] and blocking certain neural transmissions with chemical treatments [200].

Such experiments have revealed the basic swimming control system of Cliones down to the cellular level. A Clione usually maintains vertical orientation with its head up and maintains its depth or swims upward by flapping its two wings. The wings are driven by somehow independent wing controllers, where each controller interacts with the other to synchronize. The wing controller consists of CPGs that generate most of the motor outputs, and sensory feedback from the wing does not play a noticeable role [15]. The rhythmic neural patterns in CPGs are generated both by individual neurons and by interactions between neurons [18]. Gravitational sensory data from the statocysts are used to maintain the upright posture by flexing the tail and swinging one wing larger than the other [60]. When water temperature is high, this feedback loop reconfigures to reverse the actions (i.e. the tail flexes to the opposite direction and vice versa) and the

Clione inverts its orientation and swims downward.

2.1.2 Hierarchical Control

The locomotion controllers in most animals can be interpreted as a hierarchical structure with two layers, where the lower layer generates the basic motor patterns for locomotion and the higher layer sends simple commands, such as desired speed and direction, to the lower layer [196] (Fig. 2.2). In some vertebrates, it is known that the neural network at the spinal cord is capable of conducting the lower layer control with simple modulation signals from the supraspinal system. For example, a decerebrate cat can walk on a treadmill with body-weight support if the mesencephalic locomotor region (MLR) of the brain stem is electrically stimulated. Furthermore, it can make speed and gait transitions as the MLR stimulation changes [13]. Similar observations are made in other decerebrate vertebrates such as salamanders [35] and rats [96]. Moreover, asymmetric stimulation between the left and right MLR modulates the swimming direction of decerebrate lampreys [233]. Such observations verify that the lower layer controller, located at
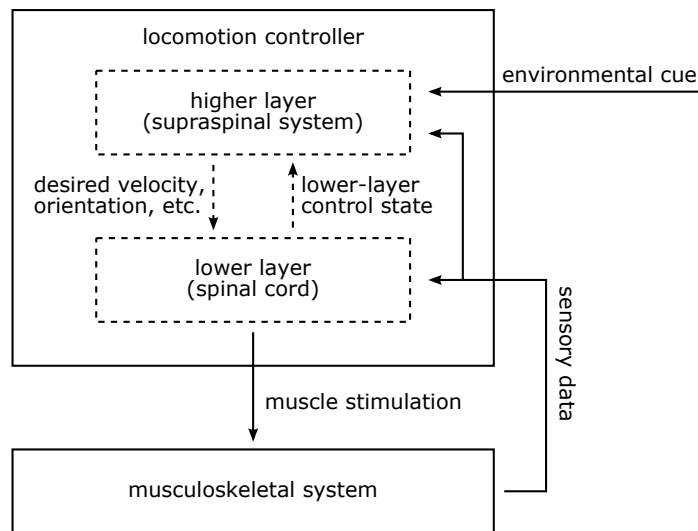
Figure 2.2: Hierarchical structure of animal locomotion controllers. The locomotion controller in most animals can be interpreted as a hierarchical structure with two layers. The higher layer sends simple commands to the lower layer based on the environmental cue and locomotion goals, and the lower layer generates muscle stimulations.

the spinal cord in case of vertebrates, is capable of the basic motor control of locomotion and can be modulated by simple signals from the higher layer controller.

Based on the observations that the lower layer controller contributes substantially to generating locomotion behaviors, the central question on the locomotion control can be rephrased into two questions on the lower layer controller: "**how does the lower layer controller generate the motor stimulations?**" and "**how is the lower layer controller modulated by the higher layer control to realize different locomotion tasks?**" Several neural control mechanisms have been hypothesized in pursuit of these questions and most of them can be categorized into mainly two mechanisms: reflexes and CPGs. In control engineering terminologies, reflexes and CPGs nearly correspond to feedback and feedforward control, respectively. Muscle synergy is another broadly studied neural control mechanism that co-activates multiple muscles by a single neural command. It has been proposed to simplify the control of high degrees of freedom (DOFs) motor systems. Studies on reflexes, CPGs and muscle synergies are reviewed below.

2.1.3 Reflex and Central Pattern Generator

A reflex pathway generates motor commands based on sensory data [48, 117] (Fig. 2.3-A). Therefore, the rhythmic neural output of a reflex pathway during locomotion is driven by the cyclic sensory data. On the other hand, a CPG is a neuron or a group of neurons that produces rhythmic neural signals without any rhythmic inputs [119, 156] (Fig. 2.3-B). The roles and contributions of reflexes and CPGs in generating the rhythmic motor patterns of locomotion have been extensively studied over the past century.

In the early 1900s, Sherrington proposed that locomotion is generated by chains of reflexes. His findings of reflex pathways in decerebrate cats and the coordination of muscles that emerges from the interplay of different reflex pathways supported his idea [229, 230]. Around the same time, Brown suggested that the rhythmic motor commands for locomotion are generated by the spinal cord without sensory inputs, and sensory feedback only plays a regulatory role. Brown
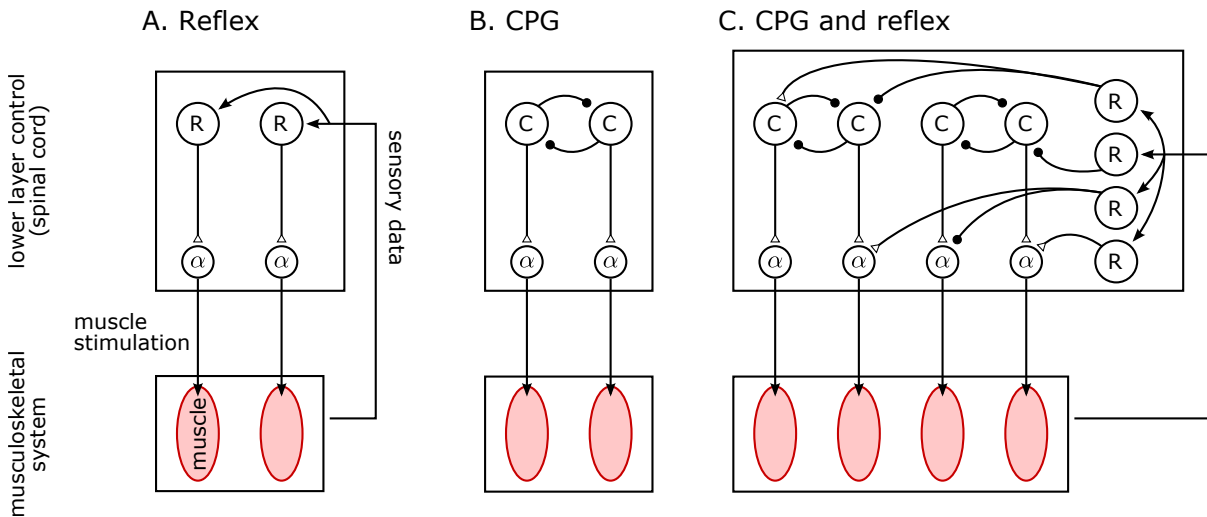
Figure 2.3: Conceptual diagrams of reflexes and CPGs. Reflexes generate motor outputs in response to sensory data (A), while CPGs generate rhythmic outputs without any rhythmic inputs (B). The current view on the lower layer of the locomotion control is that CPGs generate the basic motor commands and reflexes modulate the behavior of the CPGs and the motor commands (C). (open triangles: excitatory connections; filled circles: inhibitory connections)

observed that the rhythmic motor commands from the decerebrate cat's spinal cord persist when the sensory inputs are removed (or deafferented) [32]. He proposed a neural mechanism called half-centers which is a popular way to model CPGs to this day [33, 160, 162]. It was designed as the simplest model for generating cyclic outputs [33], wherein two groups of neurons mutually inhibit each other. Despite Brown's compelling evidence for the existence of CPGs, reflexes were considered as the key elements of locomotion control for the following few decades [48, 117]. More reflex pathways such as recurrent inhibition [73], and pathways from muscle spindles [72] and Golgi tendons [148] were discovered during this period. In the 1960s, however, Brown's studies were rediscovered and the concept of CPGs emerged [48]. In the following decades, clear evidence of the existence of CPGs in the spinal cord in many vertebrates, including lampreys, salamanders, cats, as well as some non-human primates, was found; isolated spinal cords of these vertebrates, when electrically or chemically stimulated, can produce neural outputs that are similar to intact locomotion which is called fictive locomotion [80, 95, 217]. Today, a widely

accepted view of the lower layer of the locomotion controller is that CPGs generate the basic motor commands and reflexes modulate the behavior of both the CPGs and the motor commands [116, 119, 162] (Fig. 2.3-C).

2.1.4 Muscle Synergy

A muscle synergy is a neural mechanism wherein multiple muscles get co-activated by a single neural command while each muscle can belong to multiple different synergies [24, 146] (Fig. 2.4). It has been proposed as a mechanism for reducing the DOFs of the controller relative to the number of muscles so that the control space becomes tractable. In a typical model of muscle synergies, each muscle activation is constructed by a linear combination of basic activation patterns, where the basic patterns can be generated by reflexes or CPGs, or both [43, 121]. (note: In this thesis, the term muscle synergy is not used to indicate the low dimensionality of the muscle activations, which might be the case in other literature. Instead, the term is used to indicate the neural encoding of the control mechanism.)
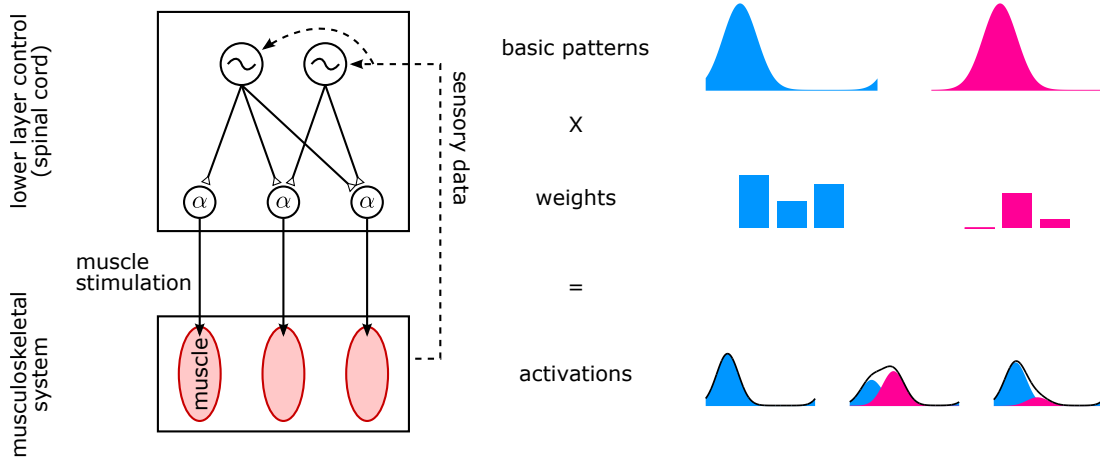
Figure 2.4: Conceptual diagram of muscle synergies. Multiple muscles get co-activated by a single neural command and each muscle can belong to multiple different synergies. The plot on the right shows a typical model of muscle synergies, where each muscle activations are constructed by linear combinations of basic activation patterns. (open triangles: excitatory connections)

Most studies on muscle synergies, across different behaviors and species, focus on inferring the basic patterns that underlie the muscle activations using factorization methods [40, 66, 120]. For example, it is found that the muscle activations during human walking and running at different speeds can be factorized into about 5 basic patterns with time shifts [40]. The basic patterns observed in locomotions of rats, cats and monkeys are similar to each other and not much different from humans [66]. These studies suggest humans and animals use a small number of muscle synergies driven by similar basic patterns to control locomotion. One critique of these studies is that the results only reveal the low dimensionality of the investigated behaviors, which is somewhat expected given the experimental task constraints [145, 257]. In addition, it is known that humans can train to control individual muscles [20], indicating that, at least in humans, muscle synergies are not the smallest control units of the CNS.

More compelling evidence supporting muscle synergies is found in rats and frogs [25]. Electrically stimulating a locus of the spinal cord generates a consistent force field of the hind limb, which is a mapping of the positions and the produced forces. Stimulating different loci generates different groups of force fields, and simultaneously stimulating two loci results in a linear summation of the individual force fields. These observations show that multiple muscles can be recruited in a functionally relevant manner by a single stimulation at the spinal cord.

2.2 Extrapolation to Human Locomotion Control

Much of the current understanding of human locomotion control relies on experimental studies of simpler animals [39, 196]. However, the control of human locomotion may be much different from that of other animals [39, 187, 196]. For example, humans locomote bipedally with an erect posture, which is dynamically unstable [143, 225] and, therefore, may require special control strategies. This section first describes the control of human locomotion at the behavioral level (Sec. 2.2.1) and then reviews how the neural control mechanisms observed in animal locomotion extrapolate to those in humans (Sec. 2.2.2).

2.2.1 Behavioral Level

The kinematics and dynamics of the human skeletal system are the product of the neural controller at the behavioral level. The skeletal system is actuated by muscles, whose activations are the immediate output of the neural controller. Kinematic, dynamic and muscle activation data of human locomotion are measurable with gait analysis techniques. Kinematic data such as the joint angles are acquired from motion capture systems, ground reaction forces (GRFs) are measured from force plates, joint torques are calculated by solving the inverse dynamics from the kinematic data and the GRFs, and muscle activations are obtained from electromyography (EMG) signals. (Such data during normal walking [205] and running [40, 189] are reported in the literature and are not reviewed in this thesis.) Unfortunately, the muscle activations and the behavioral data do not fully describe the underlying control algorithm. To further understand the behavioral level algorithm encoded in the neural controller, researchers apply disturbances to or impose constraints on walking and running subjects and interpret their reactions [49, 76, 112, 161].

There are different ways of describing human gaits [189, 205, 246]; here, I explain human walking and running at a very abstract level based on the functionalities that are speculated to be important (Fig. 2.5). The head, which includes the visual and vestibular system, is stabilized
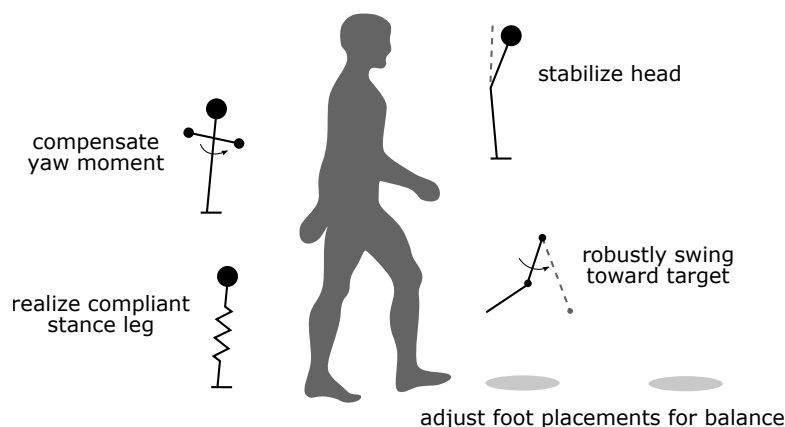
Figure 2.5: Functional explanation of human gaits. The figure visualizes the functional explanation of human walking and running.

during walking and running [209]. To this end, the trunk segment is mostly upright [111], while it is sometimes modulated, for example, to effectively change speed [189] or to carry load [139]. The arms swing in opposite phase with their ipsilateral legs, which reduces the ground reaction moment (GRM) around the vertical axis [49, 109]. In addition, about 10% of vertical propulsion during running can be generated by swinging the arms [110]. The legs, during stance phase, show compliant behavior for both walking and running [79, 136] to moderate ground contact impacts [2]. During swing phase, the legs swing robustly toward the next foot placement [76]. Placing the swing foot at an appropriate position is considered as a primary strategy for maintaining balance during locomotion [112, 274]. During walking, humans seem to plan for two to three footsteps ahead [161, 201]. It is widely accepted that all of these functionalities are realized in an energy efficient way [3, 287].

2.2.2   Neural Circuitry Level

Simply extrapolating the understanding in other animals, the neural control of human locomotion is often assumed to have the hierarchical structure, where the higher layer controller sends simple commands, and the lower layer generates the detailed motor patterns (Fig. 2.2). It is further assumed that, in the lower layer, CPGs generate the basic neural patterns, reflexes modulate the behavior of the CPGs and the neural patterns [116, 196] (Fig. 2.3-C), and the neural patterns may combine and distribute to the muscles using muscle synergies [40] (Fig. 2.4). However, observations in humans suggest that the control structure of humans is different from that of other animals at least in two aspects.

First, the role and contribution of each the higher layer (brain) and the lower layer (spinal cord) controllers in human locomotion are less clear. The higher layer controller seems to play a more important role in humans than in other animals. There is evidence of the higher layer controller, or the brain, directly modulating muscle activations in human walking. Corticomotoneuronal cells, which are only found in primates, are in the motor cortex (in the brain) and

directly modulate the motoneurons in the spinal cord. It has been observed using transcranial magnetic stimulation that, in human walking, corticomotoneuronal cells modulate the soleus (SOL) and tibialis anterior (TA) activations [206]. On the other hand, other observations suggest that the lower layer control still plays an important role. For example, spinal cord injured patients, although difficult to induce, are able to generate stepping behaviors [65], and the activity of the primary motor cortex during active pedaling is not much different from that during passively driven pedaling motion [44].

Second, although they are often assumed to play crucial roles, it is not clear if CPGs and muscle synergies exist in humans [24, 156, 187]. Fictive locomotion, which would be a direct evidence of CPGs, has not been observed in humans [170]. One of the closest evidence is the oscillatory hip movements observed in a chronic incomplete spinal cord injured patient with the hip anesthetized [36]. Similarly, direct evidence for the neural origin of muscle synergies in humans is not found. To the best of my knowledge, all studies on muscle synergies in human locomotion only reveal the low dimensionality of the investigated muscle activation patterns rather than their neural origins [40, 120].

Different from CPGs and muscle synergies, it is clear that spinal reflexes play a role in controlling human locomotion. A direct evidence is that motor commands are modulated in response to unexpected disturbances before the supraspinal control can react considering the neural transmission delays between the brain and the muscles [220]. Based on observations that the activations of reflexes are task dependent as well as phase dependent (e.g. Hoffman reflex (H-reflex) of the SOL is different for walking and running and is larger during stance than during swing [38, 231]), it is often assumed that reflexes are modulated in a functionally useful way. Various reflexes are observed during human locomotion. Different types of disturbances ranging from whole body disturbances (e.g. tripping [76, 221] and slipping [22, 47, 234, 270]) to electrical (e.g. H-reflex [37, 231] and cutaneous reflex [183, 269]) and mechanical (e.g. stretch reflex [55, 232, 284] and tendon tap reflexes [64, 78]) stimulations on specific muscles and body parts

reflex	observation	speculation / note
SOL H-reflex	much larger during stance than swing	contributes much to ankle extensors during stance [38]
	larger during running than walking	the opposite is reported in [38], see [231] for discussion
	smaller in beam walking	high reflex gain may cause instability [153]
SOL stretch reflex	correlations between reflex activation and sensory data during walking	velocity feedback accounts for most of the reflex pathway and contributes about 45% of the SOL activation [284]
SOL load receptor reflex	correlation between the force feedback and muscle load	SOL may be activated by positive force feedback at late stance [94]
cutaneous reflex	tibial nerve reflexes and reflex reversals	cutaneous reflex may be important in withdrawal responses [283], cutaneous reflex may be related to activating other reflex pathways [68]

Table 2.1: Spinal reflexes of human locomotion. Some of the reflexes that are observed during human locomotion and their speculated functionalities are summarized. Refer the cited papers for details.

are used to probe the activation of different reflex pathways. The functional roles and the contributions of the reflexes are interpreted based on their reactions to these disturbances (some are selected and summarized in Table 2.1, more are reviewed in [288]). More evidence is necessary to verify these interpretations [288].

2.3   Simulation Neural Control Models of Human Locomotion

Current experimental techniques do not fully reveal the neural control of human locomotion. To decode a neural control from the cellular level up to the behavioral level, one need to understand the operation of a neural network from the individual neurons (e.g. discharge properties) and their connections (e.g. synaptic properties), and the interaction between the neural network and the mechanical musculoskeletal system. Although stimulating neurons and recordings their activations using microelectrodes partially reveal the neural control network, it is not feasible to

identify the full neural network in complex animals [113, 190]. For instance, even in studies of Cliones, where only a few hundred neurons participate in locomotion control, the full properties of the neural network have not been identified [16] (Sec. 2.1.1). In comparison, there are about hundred million neurons in the human spinal cord [131]. Another way of studying the neural control is exploring the functional role or capability of groups of neurons by isolating them, such as decerebration and deafferentation. Limitations of such approach are that it is difficult to investigate interactions between the isolated group of neurons and the rest of the system, and that the observations made in isolated conditions do not necessarily generalize to their normal behaviors [39, 156]. In addition, many techniques used in investigating animals' neural control are not applicable in studying humans. Restrictively in patients, are applied invasive methods and are observed isolated neural circuitries. Experimental techniques that are used in normal humans, such as H-reflex and transcranial stimulation experiments (Sec. 2.2.2), only probe selective neural pathways. Therefore, the knowledge of the neural control of human locomotion obtained through experiments is fragmentary with large gaps between detectable circuits and measurable behavioral data.

Simulation studies of neuromechanical control models may compensate for the limitations of experimental studies. Neural control models hypothesized based on experimental observations can be investigated in physics simulation. Such investigations are especially valuable in studying human locomotion since physics simulation allows to assess control results at the behavioral level which involves complex muscle and segment dynamics. For example, if a certain control algorithm inherently cannot generate stable walking with physiologically plausible neural transmission delays, it is unlikely that such control algorithm is encoded in the human neural network. Similarly, simulation studies may propose neural circuits that seem to be necessary for realizing certain control function, providing a useful guide for experimental search.

There are many studies using computational models to better understanding the dynamics and control of human locomotion at the behavioral level. For instance, the inverted-pendulum model,
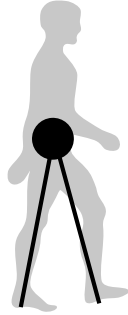
Figure 2.6: Point-mass models of human locomotion. The inverted-pendulum model describes the human body as a point mass at the COM and the legs as two massless rigid segments (A). The human body is similarly modeled in the spring-mass model except that the legs are represented as two massless linear springs (B).

where the simplest version consists of a point-mass trunk and massless rigid legs (Fig. 2.6-A), provided explanations for human standing and walking including the balancing strategies during standing and walking [274], the walk to run transition speeds [141], the speed and step-length relationship [144], and the energetic cost of human walking [67]. Similarly, the spring-mass model, which has compliant legs instead of rigid ones (Fig. 2.6-B), explains human walking and running behaviors, such as the stance leg behavior during walking and running [26, 90], the swing leg retraction in running [228], and stride frequency of running [79]. In addition, the fact that the center of mass (COM) dynamics of both walking and running can be explained by the spring-mass model suggests that humans may be using a unified controller to generate walking and running [90]. (Note that the inverted-pendulum model [135] and the spring-mass model [159], along with the linear inverted-pendulum model [129], are widely used in controlling legged robots, which is out of the scope of this review.) Although these models provide insights at the behavioral level, they are too simplified to study the human control at the circuitry level.

Plausible neural circuitries can be tested in more detailed computational models, the so-called neuromechanical models. A typical neuromechanical model consists of a skeletal system, muscle actuators, and a neural controller (Fig. 2.7). The skeletal system represents human body parts, such as the trunk, thighs, shanks, and feet, and interacts with the ground through GRFs. The
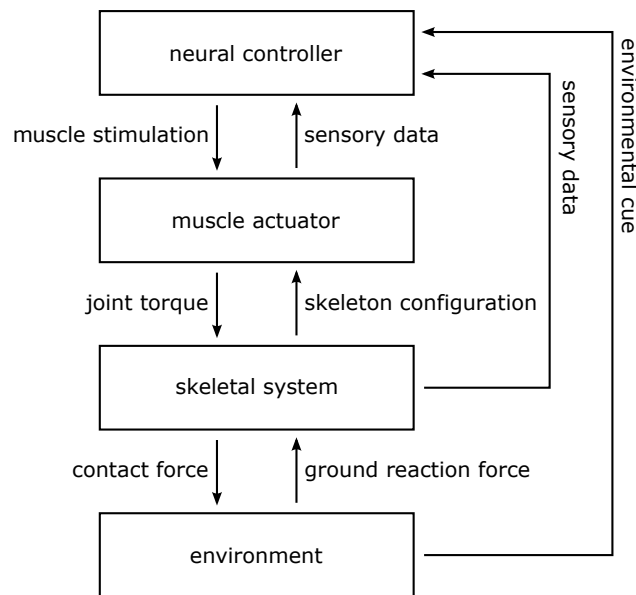
Figure 2.7: Outline of a typical neuromechanical simulation model. Neuromechanical models usually consist of a neural controller, muscle actuators and, a skeletal system. Physics simulations also model the interactions between the neuromechanical model and the environment, such as the GRFs.

joints of the skeletal system are actuated by muscle actuators, the states of which are updated based on the configuration of the skeletal system. The muscle actuators exert contraction forces based on their states and the muscle stimulation signals they receive from the neural controller. The neural controller represents the control hypothesis of human locomotion that one wants to test. Neuromechanical models are simulated in physics simulation to demonstrate that the hypothesized neural controller is capable of generating stable walking, which is not trivial to achieve but is a basic requirement for a valid locomotion controller.

There are several neuromechanical human models that demonstrate stable bipedal locomotion in physics simulation (Table 2.2). (Models which optimize the time-trajectory of muscle activations [4, 5, 99] are excluded from the review since they do not propose a neural control mechanism that generates the trajectories.) A pioneering control model of human locomotion was proposed by Taga et al. [171, 247, 248, 249]. They proposed a *CPG-based* controller, wherein CPGs generate the basic activation patterns for each joint. It was demonstrated with

model (all versions)	mechanics	control			locomotion behaviors	robustness	EMG correlation
		strategy	reflex delay	world frame			
Taga et al. [247] (1991-1998, [171, 247, 248, 249])	2D, 7 seg, 6 torques	CPG + reflex	0	all segments	walk (run [249], obst [248])	25 Ns BW push, +15 kg at pelvis	not applicable
Hase et al. [103] (1999-2011, [101, 102, 103, 138, 191, 194])	3D, 14 seg, 60 muscles	CPG + reflex	0 (5 ms [191])	all segments	walk, run	±0.5 cm ground (±2 cm ground [138])	not reported
Ogihara et al. [193] (2001)	2D, 7 seg, 18 muscles	CPG + reflex	0	none	walk	not tested	not quantified (not good)
Günther et al. [97] (2003)	2D, 11 seg, 28 muscles	reflex (λ-model)	0	trunk	stand→walk	$-2°\sim0.5°$ slopes, $0.07\sim3\times$ gravity	not quantified (not good)
Jo et al. [126] (2004-2008, [123, 124, 125, 126])	2D, 7seg, 18 muscles	CPG-mSyn +reflex	realistic	trunk	stand→walk (kick, obst [124])	15 Ns pushes +15 kg at trunk	not quantified (not bad)
Aoi et al. [11] (2008-2016, [8, 9, 10, 11, 12])	2D, 7 seg, 18 muscles	CPG-mSyn + reflex	realistic	trunk	walk	10 Ns FW/BW push, +3.2 kg at trunk, $-7.4°\sim1.2°$ slopes	not quantified (not bad)
Geyer et al. [88] (2010)	2D 7 seg 14 muscles	reflex	realistic	trunk	walk	±4 cm ground	51%-99%

(seg: segments; obst: stepping over obstacles; FW: forward; BW: backward; push: external pushes are applied to the trunk segment; $\pm$h cm ground indicates a terrain with height changes of $\pm$h cm; not good/bad: visually assessed; stand→walk: walking starts from standing pose; mSyn: muscle synergy, use predefined basic patterns; kick: kicking motion while walking)

Table 2.2: Comparison of neuromechanical models. The control columns compare the control strategy, implementation of realistic neural control delays (reported to range from 5 ms to 25 ms from proximal to distal leg muscles in humans [93, 140, 164]), and the dependence on measuring the segment orientations with respect to the world frame. The robustness column compares the reported disturbances the models can tolerate. The last column shows the correlations between the muscle activations generated by the models and the corresponding human EMG data.

simple skeletal models (e.g. a point-mass trunk, joint torque actuators, no neural transmission delay) that stable locomotion can emerge from the entrainment between the CPGs and the skeletal system, which are linked to each other by sensory feedback pathways and joint actuations. In addition, the proposed model could generate walking and running at different speeds by changing a simple constant input to the lower layer controller, as in decerebrate animals. Taga's model was extended by different research groups to include more physiological components [103, 193].

On the other hand, *reflex-based* models demonstrated that stable walking can be generated without encoding any temporal characteristics, or CPGs, in the controller [88, 97], suggesting that CPGs may not be playing a critical role in human locomotion. In other studies, the lower layer controller was simplified to use predefined basic activation patterns and muscle synergies to investigate specific parts of the control (e.g. phase resetting mechanism [10, 11], sensory mechanisms of stance to swing transition [12], and feedback control of the higher layer controller [126]). Most of the studies investigated only sagittal plane walking.

In the remainder of this section, one of each CPG-based and reflex-based models are discussed in more detail. The model proposed by Hase et al. [103], which is extended from Taga's model and is one of the most advanced neuromechanical models generating walking and running in 3D, is selected from the CPG-based models (Sec. 2.3.1). The model proposed by Geyer et al. [88], one of the few reflex-based models, is then discussed since it generates perhaps the most human-like walking among the existing neuromechanical models (Sec. 2.3.2).

2.3.1 Example of CPG-based Models

Hase et al. have extended Taga's model to include more physiological details [103]. The 3D musculoskeletal system consists of 14 segments, 19 internal DOFs, and 60 muscle actuators. There are one CPG per joint that generates joint activation patterns, and the joint activation patterns are distributed to individual muscle activation signals in a way that minimizes muscle fatigue. Each CPG consists of a couple of mutually inhibiting neurons generating an oscillatory neural output, or a joint activation, which is a limit cycle. Each neuron takes two types of external inputs: sensory feedback signals that modulate the CPG to adapt to external changes; and a stimulus signal from the higher layer controller that regulates the activation level of the CPG. Stable locomotion emerges from the entrainment between the CPGs and the skeletal system. The model can walk and run at different speeds with different sets of control parameters.

Although the model is one of the most advanced neuromechanical models, it has four main

limitations. First, the model does not seem to be very robust to internal and external disturbances. For instance, without modifying the CPG-based controller in a somewhat robotic way, the controller cannot tolerate neural transmission delays of more than 2 ms [191] and ground height changes of more than 5 mm [138] (cf. the closed loop delay between the ankle and spinal cord in humans are about 20 ms [93], and terrains that humans recognize as flat likely have more height changes than 5 mm). Second, although the joint angle and torque data of the model are comparable with human walking data [102], the muscle activation data are not reported. Comparing the model predicted muscle activations to the EMG data measured from humans is instructive since muscle activations are the immediate output of the neural controller. Other CPG-based models [10, 193] generate muscle activations that are comparable with human EMG data but are not as close as those produced by the Geyer's reflex-based model [88]. Third, the reflex pathways, which modulate the CPG, are chosen based on a burdensome trial-and-error process [103], and their contribution in the entire controller is not clear. Researchers have attempted to automatize the process of selecting the reflex pathways using genetic programming, but the procedure did not result in a successful controller (i.e. the resulting controller does not generate stable walking) [194]. Fourth, how the controller can be extended for diverse locomotion behaviors is not clear. The studies that extended the CPG-based models to generate more locomotion behaviors than steady walking and running have proposed to add task specific movement generators [124, 248]. While the added movement generators allowed the model to make kicking motions and to step over obstacles, how the movement generators for all different behaviors can be encoded in the neural circuitry remains unclear.

2.3.2 Example of Reflex-based Models

A neuromechanical model that consists mostly local muscle reflexes and no CPGs have been proposed by Geyer et al. [88]. The reflex pathways are selected to encode functional principles of legged locomotion. For example, the leg extensor muscles during stance are controlled

by positive force feedback pathways, which generates compliant leg behaviors [89] and thus human-like COM dynamics during walking and running [90]. As positive force feedback, most reflex pathways use local sensory data (i.e. state of its own muscle). Exceptionally, the hip muscle reflexes use the global trunk angle to balance the trunk, and some of the reflex pathways are modulated by the loads on the ipsilateral and contralateral legs. Plausible neural transmission delays are modeled for all reflex pathways. The interactions of the reflex pathways and the musculoskeletal system generate stable human-like walking. The model generates muscle activations that correlate between 51%-99% with human EMG data. Although the control parameters were hand-tuned to match human kinematic data, the EMG correlation is high compared to other models [10, 193]. Since the model can generate human-like locomotion, it has been adapted to a graphical character that generates human-like walking and running motions [273]. Although the study on the graphical character focuses on generating human-like motion instead of proposing neurophysiologically plausible controller (e.g. using torque actuators instead of muscles for the added joints), it reveals the potential of reflex-based models in describing more details of human locomotion.

Geyer's model suggests that most functionalities of normal human walking can be realized by reflexes. However, the model is insufficient to answer more specific questions. First, the model is a 2-dimensional (2D) planar model. The extension into 3D and the robustness of the 3D locomotion behavior are not addressed. Second, the control parameters that generate human-like muscle activations were tuned to match human kinematic data. Whether the model makes such prediction without prior human data, which is an essential feature for a predictive model, is unclear. Third, as the CPG-based models, it is not clear how the controller can be extended to generate diverse locomotion behaviors. Fourth, the model only represents the spinal control leaving unexplained how it can be modulated by the higher layer control.

23

2.3.3 Model of this thesis

The primary goal of the human locomotion control model of this thesis is to investigate to what extent the central questions of "**how does the lower layer controller generate the motor stimulations?**" and "**how is the lower layer controller modulated by the higher layer control to realize different locomotion tasks?**" can be answered with a reflex-based neuromechanical model. To this end, we extend and investigate Geyer's reflex-based model to explain more than sagittal plane normal walking. The extension of the model to generate diverse 3D human locomotion behaviors are covered in Chapter 3 and Chapter 4, and the plausibility of the model is evaluated in Chapter 5.

Chapter 3

Neuromechanical Simulation Methods

Part of the material of this chapter has been published in:

- Song and Geyer. Generalization of a muscle-reflex control model to 3d walking. *IEEE EMBC*, 2013. [239]

- Song and Geyer. A neural circuitry that emphasizes spinal feedback generates diverse behaviours of human locomotion. *The Journal of physiology*, 2015. [240].

This chapter presents the neuromechanical simulation environment, the platform used to investigate neural control models. First, the simulation environment (Sec. 3.1) and the latest 3D musculoskeletal model are explained (Sec. 3.2). Delays and noise in the neural transmissions (Sec. 3.3) and the foot-ground contact model (Sec. 3.4) are described as well. In addition, the physiologically based performance criteria (Sec. 3.5) and a parameter optimization technique used for tuning the neural control parameters (Sec. 3.6) are presented.

3.1   Simulation Environment

The neuromechanical model is implemented and simulated in MATLAB/Simulink (Fig. 3.1). The mechanical dynamics of the skeletal system are modeled in SimMechanics. A variable-time-step solver ode15s is used with the maximum step size of 10 ms, relative error tolerance

of 10^{-3}, and absolute error tolerance of 10^{-4}. In Rapid Accelerator mode, which generates and runs a standalone C code, the 3D neuromechanical model runs at about 120% of real-time on a 3.4 GHz CPU machine.

3.2 Human Musculoskeletal System

The musculoskeletal model consists of rigid skeletal segments and muscle-tendon units (MTUs) (Fig. 3.2). The properties of the skeletal segments (Sec. 3.2.1) and the MTUs (Sec. 3.2.2) are set to approximate physiological data. The musculoskeletal attachments define the relationship between the lengths (l_{mtu}) and forces ($\boldsymbol{F}_{mtu}$) of MTUs and the joint angles ($\boldsymbol{\varphi}_j$) and torques ($\boldsymbol{\tau}_j$) of the skeletal system (Sec. 3.2.3). The musculoskeletal attachment parameters are set based on physiological data and to ensure the range of motion (ROM) of every joint and muscle.

3.2.1 Skeletal Segments

The skeletal segment properties (Fig. 3.3) are set based on physiological data to model a $h_{MS} = 1.8$ m tall male who weighs $m_{MS} = 80$ kg [42, 88, 97]. The skeleton system consists seven segments representing the trunk as well as the thighs, shanks, and feet. The trunk segment represents the whole upper body including the pelvis. Each segment is modeled as a single rigid body. An exception is the thigh segments, which is explained below in more detail. The segments are connected by revolute joints. The dimensions and inertial properties of each joint are summarized in Table 3.1.

Different from other body parts, each thigh consists of two rigid bodies connected by a prismatic joint. A nonlinear spring-damper force acts on the prismatic joint as

$$F_{thigh} = -k_{thigh}\Delta x_{thigh}\left(1 + \text{sign}\left(\Delta x_{thigh}\right)\Delta \dot{x}_{thigh}/\Delta \dot{x}_{thigh,max}\right) \tag{3.1}$$

where Δx_{thigh} and $\Delta \dot{x}_{thigh}$ are the displacement between the rigid bodies and its rate, respectively, $k_{thigh} = m_{trunk} \cdot g/0.005$ Nm^{-1} is the stiffness coefficient ($g = 9.81$ ms^{-2} is gravity),

26
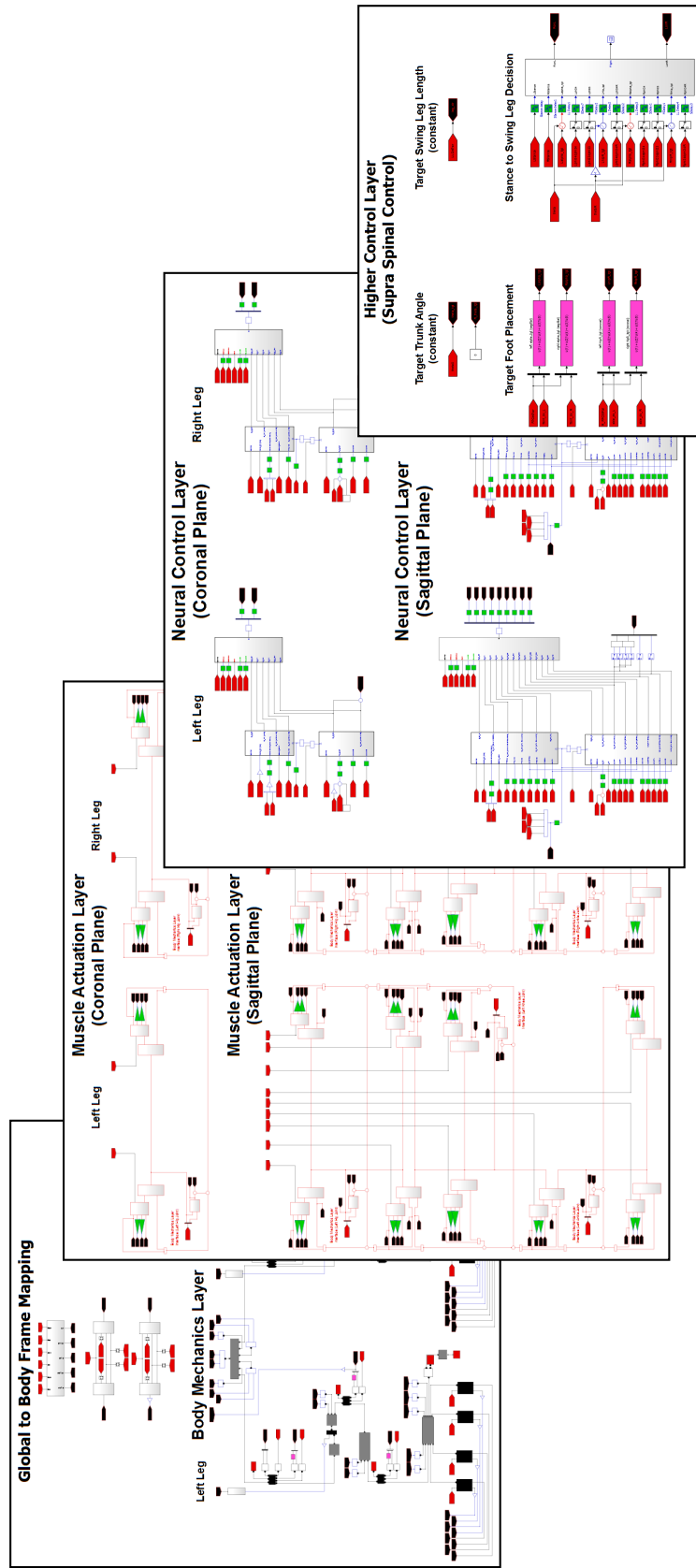
Figure 3.1: Simulink implementation of the neuromechanical model. Simulink is a block diagram environment for modeling and simulating dynamic systems.

The full model is archived at `http://www.cs.cmu.edu/~smsong/nmsModel/nmsModel.html`
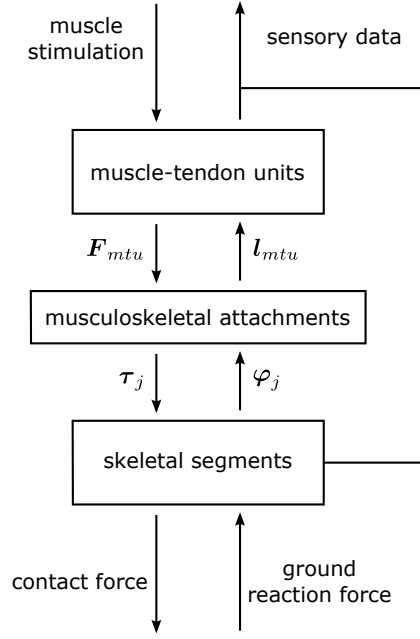
Figure 3.2: Outline of the human musculoskeletal model. The musculoskeletal system provides sensory data to and takes muscle stimulation from the neural controller, while interacts with the environment through contact forces (Fig. 2.7).

and $\Delta\dot{x}_{thigh,max} = 0.5$ ms^{-1} scales the displacement rate. k_{thigh} is high enough so that the thigh segments do not deflect much, and Δx_{thigh} is used in the neural controller to estimate the load along the thigh segment.

3.2.2 Muscle-Tendon Units

The MTU model is identical to the one developed in [88], which consists of a contractile element (CE), a parallel elastic element (PE), a series elastic element (SE), and a buffer elastic element (BE) (Fig. 3.4-A). The MTU's contraction force is

$$F_{mtu} = F_{se} = F_{ce} + F_{pe} - F_{be}. \tag{3.2}$$

The CE, which is the only active component in the MTU, exerts contraction force as

$$F_{ce} = A_m \, F_{max} \, f_l \, (l_{ce}) \, f_v \, (v_{ce}) \,, \tag{3.3}$$

28
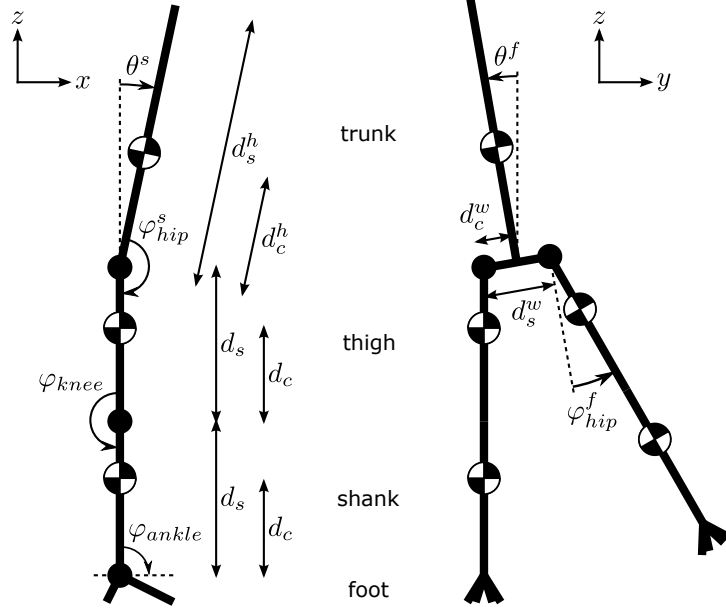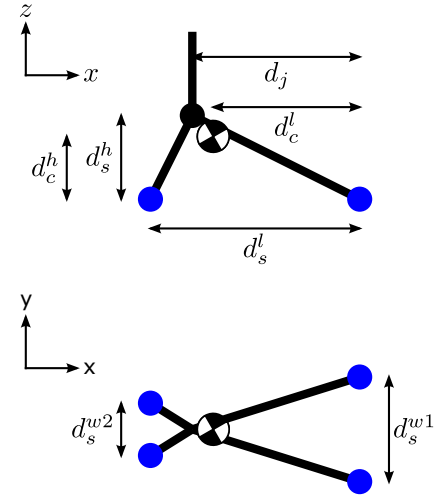
Figure 3.3: Human skeletal model. The plot on the left shows the human skeletal model and the parameters that define the system (A). Details of the foot segments are shown at the right (B). The COM of each segment, the revolute joints (black solid circles), and contact points (blue solid circles) at the heel and ball are also shown. (Details about the foot-ground contact are described in Section 3.4.)

	trunk	**thigh**	**shank**	**foot**
d_S [cm]	80(h), 20(w)	46	46	20(l), 8(h), 10(w1), 5(w2)
d_J [cm]	-	-	-	16
d_G [cm]	35(h), 10(w)	28	28	14(l), 6(h)
m_S [kg]	53.5	8.5	3.5	1.25
Θ_x [kg· m^2]	4.0	0.15	0.05	0.0007
Θ_y [kg· m^2]	2.5	0.15	0.05	0.005
Θ_z [kg· m^2]	1.0	0.03	0.003	0.005

Table 3.1: Skeletal segment parameters. m_S is the mass and Θ_x, Θ_y and Θ_z are the moments of inertia around the principal axes. Other parameters are defined as shown in Fig. 3.3.
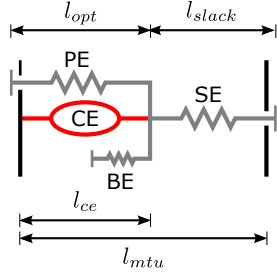
A. Muscle-tendon unit   **B. Force properties**
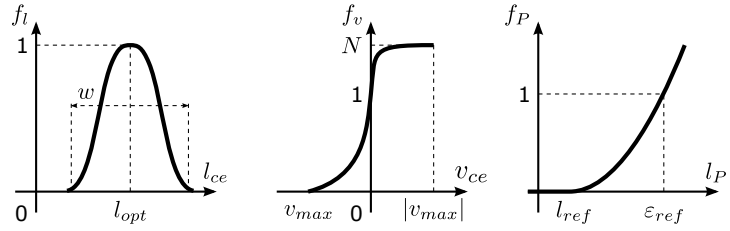
Figure 3.4: Muscle-tendon unit model. The MTUs model is shown on the left (A). The plots on the right show the force properties of the CE and passive elastic elements (B). f_P shows the piecewise quadratic force-length relationship of the passive elements.

parameter / description		value	parameter / description		value
w	CE force-length curve width	$0.56\, l_{opt}$	ε_{pe}	PE reference strain	w
K	CE force-velocity curvature	5	ε_{se}	SE reference strain	$0.04\, l_{slack}$
N	CE force-velocity enhancement	1.5	ε_{be}	BE reference compression	w/2

Table 3.2: Common MTU parameters.

where A is a muscle activation signal from the neural controller, F_{max} is the maximum isometric force, and $f_l\,(l_{ce})$ and $f_v\,(v_{ce})$ are the force-length and force-velocity relationships of the CE, respectively. The CE's force-length relationship is modeled as

$$f_l\,(l_{ce}) = \exp\left(\ln(0.05)\left|\frac{l_{ce} - l_{opt}}{w}\right|^3\right), \tag{3.4}$$

where l_{ce} is the length of the CE, l_{opt} is the optimum CE length, and w is a constant value defining the width of the force-length relationship curve. The force-velocity relationship is modeled as

$$f_v\,(v_{ce}) = \begin{cases} \frac{v_{max}-v_{ce}}{v_{max}+Kv_{ce}}, & \text{if } v_{ce} < 0 \\ N + (N-1)\frac{v_{max}+v_{ce}}{7.56Kv_{ce}-v_{max}}, & \text{o.w.} \end{cases}, \tag{3.5}$$

where $v_{ce} = \frac{\mathrm{d}}{\mathrm{d}t}l_{ce}$ is the rate of the CE's length change, $v_{max} < 0$ is the maximum contraction velocity, and K and N are constant values that define the relationship curve. The PE and SE

passively generate contraction forces when stretched as

$$F_{pe}\left(l_{ce}\right) = \begin{cases} F_{max}\left(\frac{l_{ce}-l_{opt}}{\varepsilon_{pe}}\right)^2 f_v\left(v_{ce}\right), & \text{if } l_{ce} > l_{opt} \\ 0, & \text{o.w.} \end{cases} \tag{3.6}$$

and

$$F_{se}\left(l_{se}\right) = \begin{cases} F_{max}\left(\frac{l_{se}-l_{slack}}{\varepsilon_{se}}\right)^2, & \text{if } l_{se} > l_{slack} \\ 0, & \text{o.w.} \end{cases}, \tag{3.7}$$

respectively. ε_{pe} and ε_{se} are the reference strains, and l_{slack} is the slack length of the SE. Since $F_{pe} \propto f_v\left(v_{ce}\right)$, eq. (3.2) can be reformulated as $f_v\left(v_{ce}\right) = \frac{F_{se}+F_{be}}{AF_{max}f_l(l_{ce})+F_{pe}^*}$, where $F_{pe}^* = \frac{F_{pe}}{f_v(v_{ce})}$, and this reformulation allows all the MTU states to be updated by resolving the inner DOF l_{ce} without numerical issues (e.g. $f_v\left(v_{ce}\right) > 0$ is guaranteed). The BE passively generates expansion force when compressed, keeping the MTU from collapsing, as

$$F_{be}\left(l_{ce}\right) = \begin{cases} F_{max}\left(\frac{l_{ce}-(l_{opt}-w)}{\varepsilon_{be}}\right)^2, & \text{if } l_{ce} < (l_{opt} - w) \\ 0, & \text{o.w.} \end{cases}, \tag{3.8}$$

where ε_{be} is the reference compression of the BE. The force properties of eqs. (3.4) to (3.8) are depicted in Fig. 3.4-B. The parameter values that define the common MTUs properties are set to reflect data from the literature [267, 268, 276] (Table 3.2).

Each leg of the human musculoskeletal model consists of 11 MTUs (Fig. 3.5). They are the hip abductor (HAB); the hip adductor (HAD); the hip flexor (HFL); the glutei (GLU), a hip extensor; the hamstring (HAM), a biarticular hip extensor and knee flexor; the rectus femoris (RF), a biarticular hip flexor and knee extensor; the vastii (VAS), a knee extensor; the short head of biceps femoris (BFSH), a knee flexor; the gastrocnemius (GAS), a biarticular knee flexor and ankle extensor; SOL, an ankle extensor; and the TA, an ankle flexor. All individual muscle parameters are set based on the physiological data in the literature [14, 88, 281] (Table 3.3). The length parameters l_{opt} and l_{slack} are estimated directly from the reported data. The remaining parameters are calculated as $F_{max} = 25[\text{Ncm}^{-2}] \times \text{PCSA}[\text{cm}^2]$, $m_m = 1.06 \times 10^{-3}[\text{kg cm}^{-3}] \times$
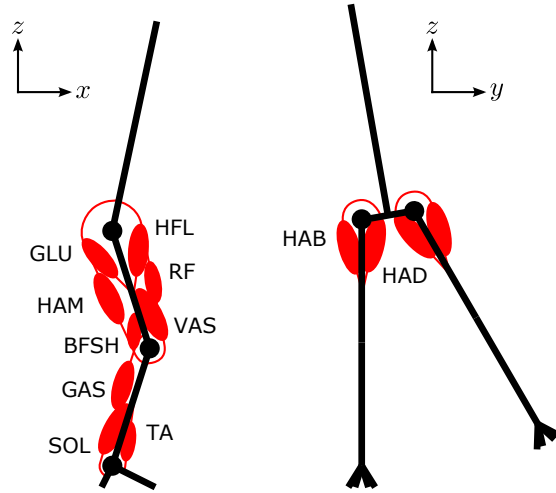
Figure 3.5: Human musculoskeletal model. Each leg of the model consists of 11 MTUs. Nine of them generate torques around the sagittal joints, and the other two act around the lateral joints.

	HAB	**HAD**	**HFL**	**GLU**	**HAM**	**RF**	**VAS**	**BFSH**	**GAS**	**SOL**	**TA**
F_{max} [N]	3000	4500	2000	1500	3000	1200	6000	350	1500	4000	800
l_{opt} [cm]	9	10	11	11	10	8	8	12	5	4	6
v_{max} [$l_{opt}\mathrm{s}^{-1}$]	-12	-12	-12	-12	-12	-12	-12	-12	-12	-6	-12
l_{slack} [cm]	7	18	10	13	31	35	23	10	40	26	24
m_m [kg]	1.14	1.91	0.95	0.70	1.25	0.40	2.05	0.15	0.30	0.70	0.20
p_{ft}	0.5	0.5	0.45	0.50	0.40	0.55	0.50	0.35	0.50	0.25	0.30

Table 3.3: Individual MTU parameters.

$l_{opt}[\text{cm}] \times \text{PCSA}[\text{cm}^2]$, $p_{ft} = \frac{\%FOG + \%FG}{\%SO + \%FOG + \%FG}$, and v_{max} is set to $-6\, l_{opt}\text{s}^{-1}$ if $p_{ft} < 0.3$ and to $-12\, l_{opt}\text{s}^{-1}$ otherwise; where PCSA is the reported physiological cross-sectional area, and %SO, %FOG and %FG are the reported proportion of slow oxidative, fast oxidative glycolytic, and fast glycolytic muscle fibers.

The muscle activation state, A_m (eq. (3.3)), is driven by the muscle stimulation siganls, S_m, which is the output of the neural controller. The relationship between A_m and S_m, the so-called excitation-contraction coupling is modeled as

$$\dot{A}_m = \frac{S_m - A_m}{\tau_{act/dact}}, \tag{3.9}$$

where the time constants is $\tau_{act} = 10$ ms when $S_m \geq A_m$ and $\tau_{dact} = 40$ ms otherwise [255, 277].

3.2.3 Musculoskeletal Attachments

The interactions between the skeletal segments and MTUs are defined by the moment arms $(r_{mtu}(\varphi_j))$ between the joints and the MTUs. A joint torque produced by an MTU is calculated as

$$\tau_{mtu} = r_{mtu}(\varphi_j)\, F_{mtu}, \tag{3.10}$$

and an MTU's length change is calculated as

$$\Delta l_{mtu}(\varphi_j) = \rho_{mtu} \int_{\varphi_0}^{\varphi_j} r_{mtu}(\varphi)\, d\varphi, \tag{3.11}$$

where ρ_{mtu} is a scaling factor. The resulting lengths of monoarticular and biarticular muscles are $l_{mtu} = l_{opt} + l_{slack} + \Delta l_{mtu}$ and $l_{mtu} = l_{opt} + l_{slack} + \Delta l_{mtu1} + \Delta l_{mtu2}$, respectively, where Δl_{mtu1} and Δl_{mtu2} are the length changes from the joints the biarticular muscles span.

Based on physiology data (hip joint: [14, 88]; knee joint: [271]; ankle joint: [163]), a moment arm is designed either as a constant value or as a variable depending on its joint angle. Constant moment arms

$$r_{mtu} = r_0, \tag{3.12}$$

are used for HAB, HAD, HFL, GLU, HAM_{hip}, HAM_{knee}, RH_{hip}, BFSH (where the subscripts specify the joint in case of biarticular muscles). Therefore, the MTU length changes caused by the movement of these joints are

$$\Delta l_{mtu}\left(\varphi_j\right) = \pm \rho_{mtu} r_0 \left(\varphi_j - \varphi_0\right). \tag{3.13}$$

Variable moment arms, used for RF_{knee}, VAS, GAS_{knee}, $\text{GAS}_{\text{ankle}}$, SOL, TA, are modeled as

$$r_{mtu} = r_{max} \cos\left(k_{arm}\left(\varphi_j - \varphi_{max}\right)\right), \tag{3.14}$$

	hip						knee					ankle		
	HAB	HAD	HFL	GLU	HAM	RF	HAM	RF	VAS	BFSH	GAS	GAS	SOL	TA
r_0 [cm]	6	3	8	8	8	8	5	-	-	4	-	-	-	-
r_{max} [cm]	-	-	-	-	-	-	-	6	5	-	5	6	6	4
r_{min} [cm]	-	-	-	-	-	-	-	4	3	-	2	2	2	1
φ_{max} [deg]	-	-	-	-	-	-	-	165	165	-	140	100	100	80
φ_{min} [deg]	-	-	-	-	-	-	-	45	45	-	45	180	180	180
φ_0 [deg]	10	15	160	120	140	170	180	125	125	160	165	80	90	110
ρ_{mtu}	0.7	1	0.5	0.5	0.5	0.3	0.7	0.3	0.3	0.7	0.7	0.7	0.5	0.7

Table 3.4: Musculoskeletal attachment parameters.
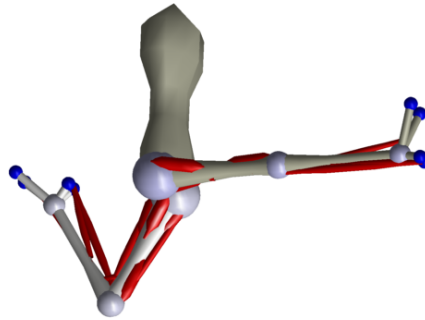
Figure 3.6: ROM test. The plot shows an exemplary pose where the ROM of the musculoskeletal model are tested. Muscle attachment parameters are defined so that the lengths of all CEs remain in a reasonable range (e.g. $l_{ce} < 1.3 l_{opt}$) in extreme poses.

and the resulting length changes are

$$\Delta l_{mtu} \left(\varphi_j \right) = \pm \frac{\rho_{mtu} r_{max}}{k_{arm}} \left\{ \sin \left(k_{arm} \left(\varphi_j - \varphi_{max} \right) \right) - \sin \left(k_{arm} \left(\varphi_0 - \varphi_{max} \right) \right) \right\}, \qquad (3.15)$$

where $k_{arm} = \frac{1}{\varphi_{min} - \varphi_{max}} \cos^{-1} \left(\frac{r_{min}}{r_{max}} \right)$ is a scaling constant. The variable moment arms are defined by their maximum and minimum values (r_{max} and r_{min}) and the corresponding joint angles (φ_{max} and φ_{min}). The parameters of all the moment arms are shown in Table 3.4.

Once all the MTU and moment arm parameters are set, the musculoskeletal attachment parameters φ_0 and ρ_{mtu} are tuned (Table 3.4) considering the ROMs of the joints and the MTUs (Fig. 3.6). φ_0 is the angle of the joints when $\Delta l_{mtu} = 0$, and ρ_{mtu} is the scaling factor in eq. (3.11). (note: Ideally, a musculoskeletal model would be defined solely by reported physiology data. For example, the scaling factor ρ_{mtu} should be defined based on pennation angles of the muscles. However, setting ρ_{mtu} based on reported pennation angles, in our case, does not allow reasonable ROMs for the musculoskeletal model.)

3.3 Neural Transmission Delay and Noise

Not many neuromechanical models include neural transmission delays (Table 2.2). However, from the control theory standpoint, control delays are considered to have profound effects on the resulting behaviors. In this thesis, all neural connections of the neuromechanical models are time delayed to reflect physiological constraints on neural transmission speed [93, 140, 164] (Fig. 3.7). The one-way delay between the supraspinal system and the spinal cord is set to $t_{ss} = 15$ ms. The delays projecting between the spinal cord and the areas of the hip, knee and ankle are set to short, medium and long delays with $t_s = 2.5$ ms, $t_m = 5$ ms, and $t_l = 10$ ms. The total delay of a neural pathway is the sum of the delays of its individual connections. For example, the delay of a spinal-reflex pathway of an ankle muscle is $t_l + t_l = 20$ ms, and the delay of a long-loop reflex pathway of an ankle muscle is $t_l + t_{ss} + t_{ss} + t_l = 50$ ms.

In addition, sensory and motor noises are added to the neural signals. The noises are modeled

35
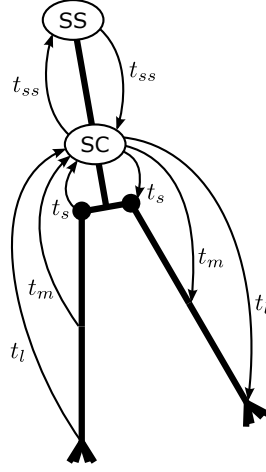
Figure 3.7: Neural transmission delays. The neuromechanical models of this thesis include neural transmission delays. (SS: supraspinal system; SC: spinal cord)

as additive white Gaussian noise. Specifically, each motor and sensory noise is drawn from $n_s \sim N\left(0, \sigma_\varphi^2\right)$ and $n_m \sim N\left(0, \sigma_\tau^2 + S_m^2\sigma_S^2\right)$, respectively, where S_m is the muscle stimulation signal. The specific values $\sigma_\varphi = \sqrt{6 \times 10^{-4}}$ deg, $\sigma_\tau = \sqrt{0.15}$ Nm, and $\sigma_S = \sqrt{1.6 \times 10^{-6}}$ are adopted from [262] which are estimated to fit human sway during standing. All the noise values are scaled for each afferent and efferent signal based on the corresponding muscle configurations.

3.4 Ground Contact Dynamics

The musculoskeletal model interacts with the ground via four compliant contact models on each foot (Fig. 3.3). The contact points are located at the edges of the foot segment in the sagittal plane representing the heel as well as the ball and toe region of a human foot. In the frontal plane, the contact points are 10 cm apart at the ball and 5 cm apart at the heel.

The point contact model extends the 2D model developed in [88]. If the contact point at a foot touches the ground, GRFs act on the foot segment at that point. The normal GRF is calculated as

$$F_n = \begin{cases} k_n\Delta d_n \left(1 + \frac{\Delta \dot{d}_n}{v_{ctc,max}}\right), & \text{if } \Delta d_n > 0 \text{ and } \Delta \dot{d}_n > -v_{ctc,max} \\ 0, & \text{o.w.} \end{cases}, \tag{3.16}$$
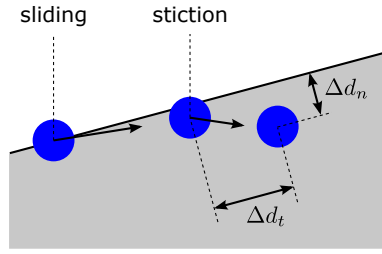
| A. Point contact model | B. Contact models in 3D terrain |
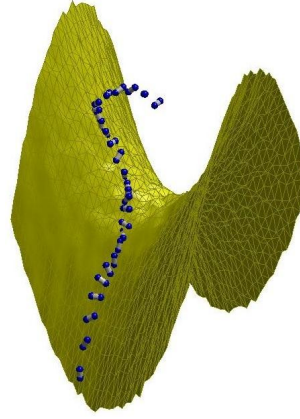
Figure 3.8: Point contact model. On the left is shown a conceptual diagram of a point contact model at three different time steps moving from left to right (A, the ground is colored in gray). The ground contact starts at sliding mode then switches to stiction mode. During stiction, the tangential distance Δd_t is defined relative to the position where stiction mode started. The right figure shows a simulation of a rigid body with two contact points colliding and sliding down a rough surface (B).

where Δd_n and $\Delta \dot{d}_n$ are the ground penetration depth and velocity along the normal axis (Fig. 3.8-A), $k_n = 39.24 \, \text{kN m}^{-1}$ is the ground stiffness, and $v_{ctc,max} = 0.03 \, \text{m s}^{-1}$ is the maximum recovery rate of the ground (while elastic or inelastic collision can be modeled by setting $v_{ctc,max} = \infty$ or 0, respectively). The k_n value is set to allow 5 mm of ground penetration deformation when standing at one foot, which can be considered as the deformation of the foot sole. ($k_n = \frac{\text{body-weight}}{0.005 \times \#\text{contact}} = \frac{80 * 9.81}{0.005 \times 4} = 39.24 \, \text{kN m}^{-1}$). The tangential GRF acts in either static or sliding mode (Fig. 3.8-A). A contact starts at sliding mode, switches to stiction mode if $\left| \Delta \dot{d}_t \right| < 0.01$ m s^{-1}, and switches back to sliding mode if $|F_t| > \mu_{st} F_n$, where $\mu_{st} = 0.9$. Sliding friction is calculated as

$$F_t = F_{t,sl} = -\text{sign}\left(\Delta \dot{d}_t\right) \mu_{sl} F_n, \tag{3.17}$$

where $\mu_{sl} = 0.8$, and stiction force is modeled as

$$F_t = F_{t,st} = -k_t \Delta d_t \left(1 + \text{sign}\left(\Delta d_t\right) \frac{\Delta \dot{d}_t}{v_{ctc,max}}\right), \tag{3.18}$$

37

where $k_t = k_n$. A rough terrain can be modeled by a polygon mesh, where the GRFs are calculated from the normal vectors of the faces (Fig. 3.8-B).

3.5 Physiologically Based Performance Criteria

Metabolic energy consumption [1, 6, 168, 169, 258] and muscle fatigue [1, 6, 169, 255] are widely used performance criteria in simulation studies of human locomotion. As they quantify a simulated gait into a performance measure without any human gait data, these performance criteria can also be used as an optimization cost and produce predictive simulations.

The metabolic energy expenditure of an MTU is calculated as presented in [258, 259], which is proposed based on mammalian and human data. The expenditure rate in W kg^{-1} is

$$\dot{E}_m = \dot{h}_{AM} + \dot{h}_{SL} + \dot{w}_{CE} \tag{3.19}$$

$$= c_{aer} A^{0.6} \left(0.4\dot{h}_{am} + 0.6\dot{h}_{am}\tilde{f}_l \right) \tag{3.20}$$

$$+ \begin{cases} c_{aer} A^2 \tilde{f}_l \left[-\frac{100 v_{ce}\left(1 - p_{ft}\right)}{v_{ce,max-st}} - \frac{153 v_{ce} p_{ft}}{v_{ce,max-ft}} \right] - \frac{F_{ce}\tilde{v}_{ce}}{m_m}, & \text{if } v_{ce} \leq 0 \\ c_{aer} A \tilde{f}_l \frac{30 v_{ce}}{v_{ce,max-st}}, & \text{o.w.} \end{cases} \tag{3.21}$$

where $c_{aer} = 1.5$ (suggested to use either $c_{aer} = 1$ or $c_{aer} = 1.5$ for primarily anaerobic and aerobic conditions, respectively), $\dot{h}_{am} = 128 p_{ft} + 25$ is the activation and maintenance heat rate, $\tilde{f}_l = f_l$ if $l_{ce} > l_{opt}$ and $\tilde{f}_l = 1$ otherwise, $\tilde{v}_{ce} = v_{ce} l_{opt}$ is the CE's velocity in ms^{-1}, m_m is the mass of the MTU, p_{ft} is the proportion of fast twitch muscle fibers, and $v_{ce,max-st} = 4.8$ and $v_{ce,max-st} = 12$ are the maximum contraction rate of slow twitch and fast twitch fibers in l_{opt}s^{-1}. The three terms represent the activation and maintenance heat rates, $\dot{h}_{AM}$, shortening/lengthening heat rate, $\dot{h}_{SL}$, and mechanical work rate, $\dot{w}_{CE}$, respectively. The total energy consumption is then calculated as the sum of the energy used by the muscles and the energy consumed by the remaining body parts (assigned as the energy rate for standing, $\dot{E}_s = 1.2$ W Kg^{-1}) as

$$E_M = \sum_m \left(m_m \int \dot{E}_m dt \right) + \left(m_{total} - \sum_m m_m \right) \int \dot{E}_s dt. \tag{3.22}$$

Muscle fatigue is another performance criterion that is widely used in simulation studies. It is defined as an inverse of muscle endurance, which is the maximum time duration of maintaining target force. It is estimated based on either muscle force, as $\sum_i^m \left(\int \bar{F}_i^p dt \right)$, or muscle fatigue, as $\sum_i^m \left(\int A_i^p dt \right)$. The normalized muscle force, $\bar{F}_m = \frac{F_m}{F_{max}}$, is used to equally account for the small muscles, and the power term, p is tuned to fit experimental data, which normally ranges between 1.5~5.0. We calculate muscle fatigue as

$$FTG = \sum_m \left(\int A_m{}^2 dt \right),$$
(3.23)

which is one of the most widely used formula in human gait simulations [6, 169, 254].

More analysis on the muscular energy consumption and fatigue calculations can be found in Section 6.2 and Figures 6.13 and 6.15.

3.6 Control Parameter Optimization

The neuromechanical models consist of many control parameters. For example, the neural controller presented in Chapter 4 has 82 control parameters. As in many other studies, I use an optimization technique to set these parameter values. Using parameter optimization techniques has advantages over hand-tuning, in that it is an automated process and the full capability of a given system can be explored. In addition, a resulting behavior of parameter optimization has a clear implication since it explicitly minimizes a given cost function.

Covariance matrix adaptation evolution strategy (CMA-ES) [100], a stochastic optimization technique, is used to optimize the parameters of the neuromuechanical model. CMA-ES is widely used in policy based walking controllers [87, 272] since it is designed for non-linear and non-convex optimization problems. The process of CMA-ES is described in Fig. 3.9. In one generation, λ_{cma} number of parameter sets are randomly sampled from a multivariate normal distribution. The cost of each new parameter set is evaluated by running a neuromechanical simulation with the parameter set. Then, the half of the parameter sets with lowest costs are used to

update the mean and the covariance matrix of the multivariate normal distribution, which is used to sample new parameter sets in the next generation. This process is iterated for n_{cma} generations. The mean vector and the covariance matrix of the initial normal distribution, $\boldsymbol{m}_{cma,1}$ and $\boldsymbol{C}_{cma,1}$, are set by the user. CMA-ES provides a novel way of updating the covariance matrix with few assumptions on the nature of the cost function. In addition, CMA-ES only uses the order of the cost function values in selecting the parameter sets with low costs, so neither derivatives nor the cost function values themselves are required. In this thesis, a typical CMA-ES trial runs with $\lambda_{cma} = 64$ and $n_{cma} = 400$, where the initial parameter set $\boldsymbol{m}_{cma,1}$ is hand-tuned to make at least 2~3 steps before falling down and $\boldsymbol{C}_{cma,1}$ is a diagonal matrix with the diagonal values set to 1% of $|\boldsymbol{m}_{cma,1}|$. The CMA-ES trial takes about a day on a 4-core modern desktop.

As an example of using, the neural control parameters can be optimized for energy-efficient normal walking. Since CMA-ES uses only the order of costs, a cost function only needs to assign lower costs for more desirable behaviors. Such cost function used for energy-efficient walking consists of three parts,

$$
J = \begin{cases}
2c_0 - x_{fall}, & \text{if fall} & \text{(3.24a)} \\
c_0 + d_{steady}, & \text{if non-steady walk} & \text{(3.24b)} \\
100 \left\| \boldsymbol{v}_{avg} - \boldsymbol{v}_{tgt} \right\| + C_E, & \text{if steady walk} & \text{(3.24c)}
\end{cases}
$$

with the first two parts encouraging the model not to fall down first (eq. (3.24a), x_{fall} is the distance traveled before falling) and then to achieve steady locomotion (eq. (3.24b)). The steadiness measure d_{steady} is the summed differences of the relative cartesian positions of the segment edges at heel strike. Based on sufficient tests, the model is considered in steady locomotion if this sum is smaller than 10 cm for six consecutive steady steps (3 cm for sagittal plane 2D models). The last part (eq. (3.24c)) encourages energy efficient locomotion (energetic cost C_E) at a target velocity $\boldsymbol{v}_{tgt} = [v_{tgt,x}, v_{tgt,y}]$, where the frontal plane target speed $v_{tgt,y} = 0$, and $\boldsymbol{v}_{avg}$ is the average velocity. The constant $c_0 = 10^3$ ensures eq. (3.24a) > eq. (3.24b) > eq. (3.24c). The energetic cost is calculated as $C_E = \frac{E_M}{m_{MS} \| (\Delta x_{COM}, \Delta y_{COM}) \|}$, where the metabolic energy E_M is obtained by
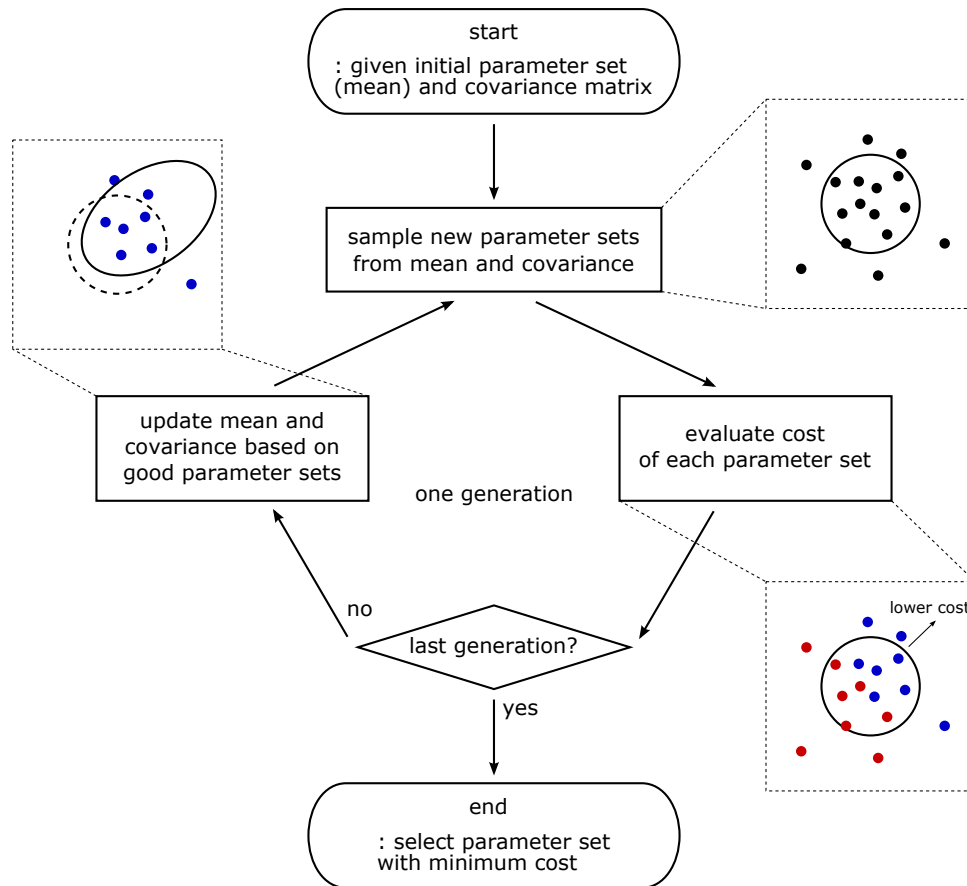
Figure 3.9: Outline of CMA-ES. CMA-ES samples new parameter sets, or samples, using a covariance matrix which evolve over generations. Each generation consists of three steps (square boxes). Schematic diagrams (dotted boxes) are shown for a generation, where the covariance matrix is updated toward lower costs in the parameter space. (circular line: covariance matrix; black solid circle: candidate samples; blue solid circle: samples with lower costs; red solid circle: samples with higher costs)

integrating eq. (3.22), and $\|(\Delta x_{COM}, \Delta y_{COM})\|$ is the distance traveled in the horizontal plane. The values of $\boldsymbol{v}_{avg}$ and C_E are calculated over the last six consecutive steps of steady walking.

Chapter 4

Neural Control Model that Generates Diverse Human Locomotion Behaviors

Most of the material of Sections 4.1 and 4.2 has been published in:

- Song and Geyer. A neural circuitry that emphasizes spinal feedback generates diverse behaviours of human locomotion. *The Journal of physiology*, 2015. [240],

and the discussion in Section 4.4 is based on the works published in:

- Song and Geyer. Regulating speed and generating large speed transitions in a neuromuscular human walking model. *IEEE ICRA*, 2012. [238]

- Song and Geyer. Regulating speed in a neuromuscular human running model. *IEEE Humanoids*, 2015. [241]

- Song. Towards a hierarchical neuromuscular control model with reflex-based spinal control - study with a simple running model. *ISIS*, 2015. [235].

This chapter presents a spinal-reflex-based control model that can generate diverse human locomotion behaviors in the neuromechanical simulation environment described in the previous chapter. The main purpose is to investigate to what extent the central questions of "how does the lower layer controller generate the motor stimulations?" and "how is the lower layer controller modulated by the higher layer control to realize different locomotion tasks?" postulated in Chapter 2 can be answered with a spinal-reflex-based neuromechanical model with no CPG. We first

describe the details of the reflex-based neural control model (Sec. 4.1) and the locomotion behaviors the model can generate (Sec. 4.2). Then we discuss the implications of the model related to the central questions (Sec. 4.3) and suggest future directions (Sec. 4.4)

4.1 Neural Control Model

The proposed neural circuitry is organized into spinal reflex modules combined with a supraspinal layer. The spinal modules realize individual limb functions essential to legged systems with decentralized feedback control. The supraspinal layer adjusts the desired foot placements and modulates some of the spinal reflexes (Fig. 4.1). The inputs to this hierarchical control structure include the muscle states such as the length, velocity or force of the contractile elements, the ground contact information, as well as the trunk's COM position and velocity relative to the stance foot, and the leg angles and the global trunk lean. The outputs are the muscle stimulations $\boldsymbol{S}_m = [S_{HAB}^L, ..., S_{TA}^L, S_{HAB}^R, ..., S_{TA}^R]$ of the left (L) and right (R) generated by the spinal reflex modules.

4.1.1 Spinal Reflex Control Modules

Each leg's muscles are controlled by 10 reflex modules M_1 to M_{10} based on their functional role in stance (M_1 to M_5) or swing (M_5 to M_{10}) (Fig. 4.1-A). In addition, if a leg is selected by the supraspinal layer to switch from stance control to swing control during the transitional double support phase, some of the stance control modules are inhibited (M_1 and M_2) and some of the swing control modules are excited (M_6 and M_7) in proportion to contralateral leg loading. For most muscles, the resulting net stimulation is generated by several control modules that can be active simultaneously. The functions of each module and their computational implementation are described in this subsection.

The stance control is taken from [88] with modifications for some modules and an extension

A. Control overview
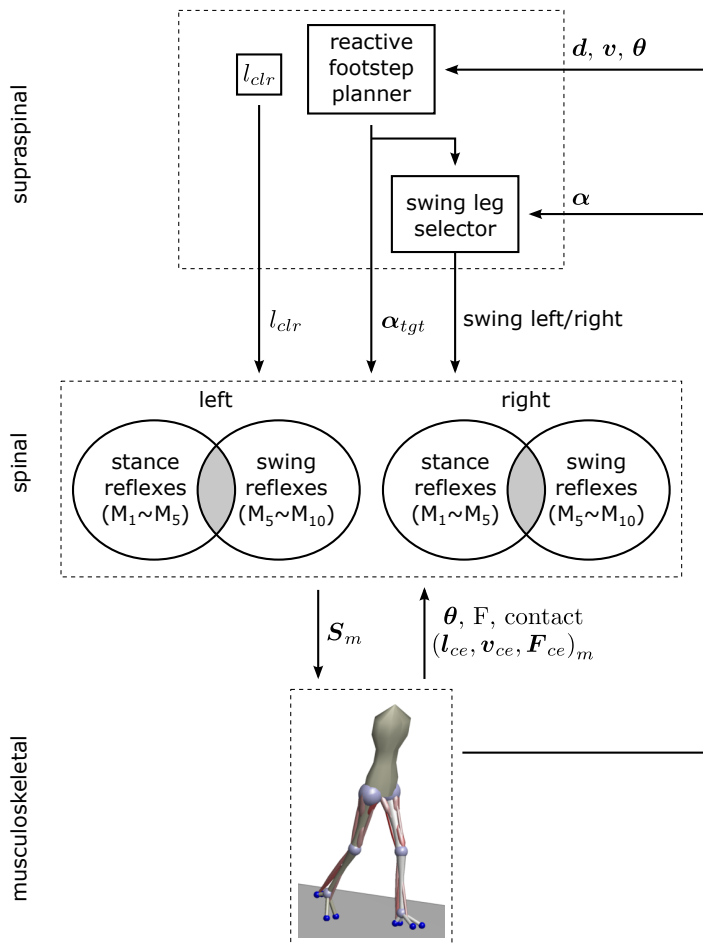
B. Reactive foot placement

$$\theta^s \quad v^s \qquad \theta^f \quad v^f$$

$$\alpha_{tgt}^{w,s} \qquad \alpha_{tgt}^{w,f}$$

$$d^s \qquad d^f$$

sagittal plane   frontal plane

C. Next swing leg

$$\boldsymbol{\alpha}_{tgt}$$

$$\|\alpha_{tgt,L} - \alpha_L\| > \|\alpha_{tgt,R} - \alpha_R\| \qquad \alpha$$

yes: swing left
no: swing right

supraspinal

reactive footstep planner

l_{clr}

$\boldsymbol{d}, \boldsymbol{v}, \boldsymbol{\theta}$

swing leg selector

$\boldsymbol{\alpha}$

l_{clr} $\boldsymbol{\alpha}_{tgt}$ swing left/right

spinal

left

right

stance reflexes ($M_1 \sim M_5$)

swing reflexes ($M_5 \sim M_{10}$)

stance reflexes ($M_1 \sim M_5$)

swing reflexes ($M_5 \sim M_{10}$)

$\boldsymbol{S}_m$

$\boldsymbol{\theta}$, F, contact
$(\boldsymbol{l}_{ce}, \boldsymbol{v}_{ce}, \boldsymbol{F}_{ce})_m$

musculoskeletal
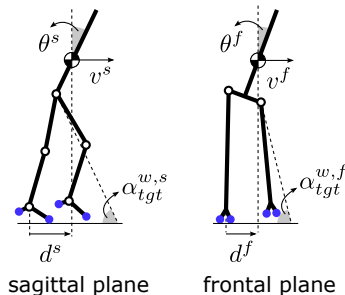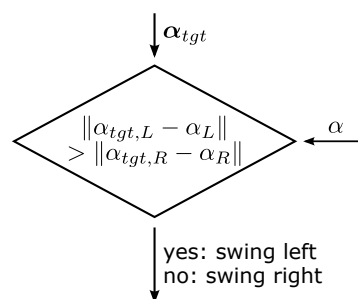
Figure 4.1: Neural control organization. The control is organized in spinal and supraspinal layers (A). The spinal layer consists of 10 reflex modules (M_1 to M_{10}) for each leg, which are active in stance or swing. The supraspinal layer adjusts the desired foot placements ($\boldsymbol{\alpha}_{tgt}$) and desired minimum swing leg length (l_{clr}), and selects which leg should transition into swing control during double support. Desired foot placement is calculated as target leg angles α_{tgt}^s and α_{tgt}^f for sagittal (s) and frontal (f) plane motions based on the velocity $v^{s,f}$ of the COM and its distance to the stance leg ankle, $d^{s,f}$ (B). In double support, swing control is initiated for the leg whose angle α is farther from the target (C).

for lateral trunk balance (Fig. 4.2). The first key function of the stance control is to robustly generate compliant leg behavior. Module M_1 realizes compliant leg behavior using positive force feedbacks (F^+) of the leg extensors (GLU, VAS and SOL). As compliant behavior of segmented legs is prone to buckling [227], M_2 prevents knee hyperextension by positive force feedbacks of the biarticular knee flexors (HAM and GAS) throughout stance and by exciting the monoarticular knee flexor (BFSH) while reciprocally inhibiting the knee extensor (VAS) with muscle length feedbacks ($L^\pm$) if the knee approaches hyperextension. The second key function of the stance control is to maintain trunk balance. M_3 is the main module realizing this behavior by activating the hip antagonists in the sagittal (HFL, GLU and HAM) and frontal planes (HAB and HAD) based on an assumed vestibular or visual feedback of the trunk pitch (θ_s) and roll (θ_f) in the world frame. (S^+ in the M_3 panel of Fig. 4.2-A indicates that HAM is co-stimulated in proportion to the stimulation of GLU.) The intensity of the M_3 output is modulated by sensory feedback of the load F_i on the ipsilateral leg to prevent it from slipping due to exaggerated hip torques. In addition, the module M_4 compensates for the moment induced on the trunk by the contralateral swing leg by co-stimulating the ipsilateral leg's antagonist hip muscles in the sagittal plane and agonist hip muscles in the frontal plane (S^+).

The last spinal module active in stance control, M_5, is also active in swing control and serves a dual purpose. It uses muscle length feedback (L^+) of the ankle flexor (TA) to generate foot ground clearance in swing and to prevent ankle hyperextension in stance. During stance, this length feedback is inhibited reciprocally by negative force feedback (F^-) from the ankle extensor (SOL) to reduce unnecessary antagonistic activation.

The main part of the swing control composed of modules M_6 to M_{10} is adapted from [62] (Fig. 4.2). Its key functions are to generate sufficient ground clearance and to robustly place the leg into target angles in the sagittal and frontal planes. The desired minimum leg length, l_{clr}, for ground clearance and target angles $\boldsymbol{\alpha} = \left[\alpha_{tgt}^s, \alpha_{tgt}^f \right]^T$ are provided to the spinal layer by supraspinal inputs (Fig. 4.1-A). Throughout swing, module M_6 drives the hip muscles (HFL,
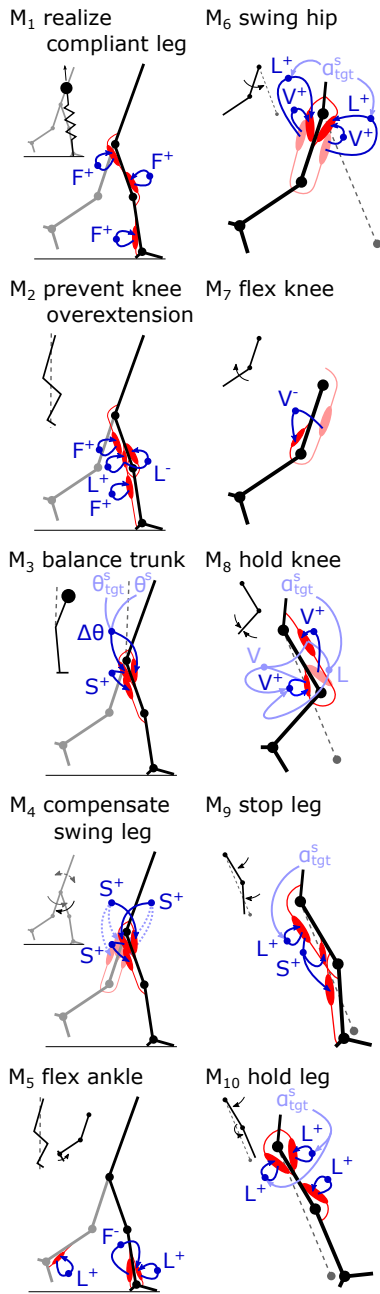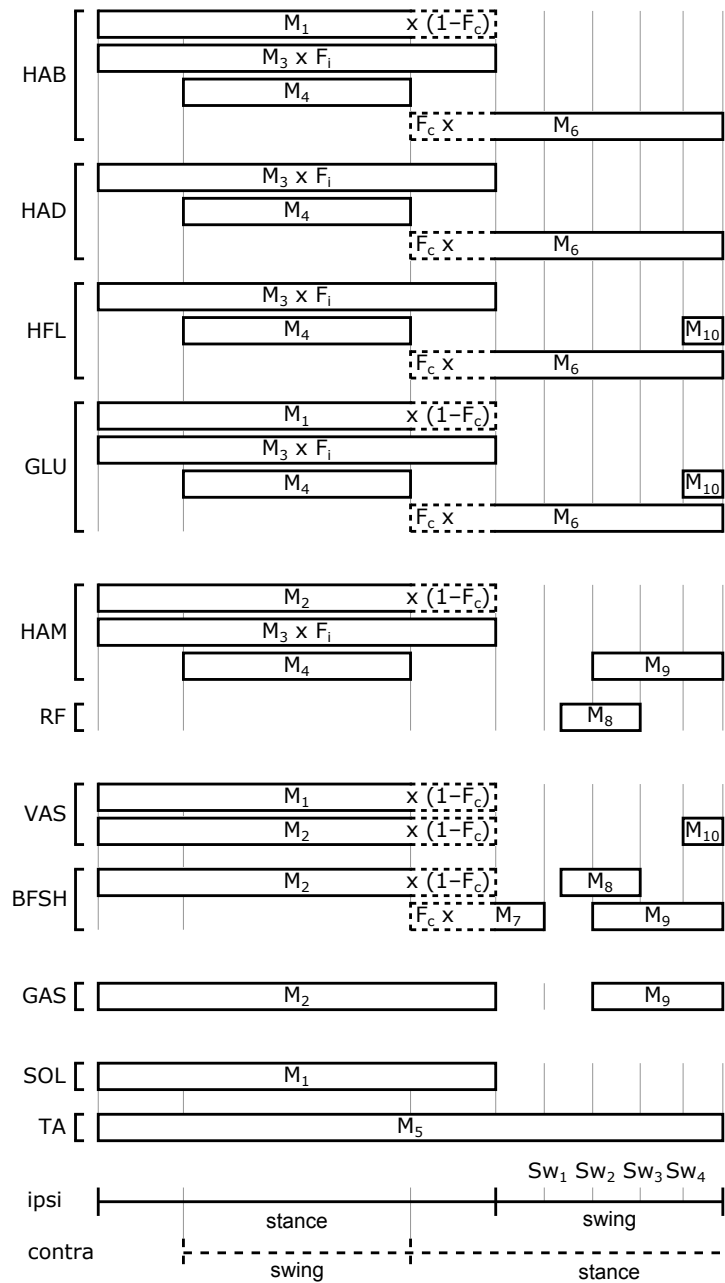
Figure 4.2: Reflex modules of the spinal control layer. 10 reflex modules realize with decentralized feedback key functions of legged systems (A). The contributions of the modules to each muscle's stimulation throughout the gait cycle is depicted at the right (B). The dotted portions indicate modules that are inhibited or excited during double support in proportion to the load F_c on the contralateral leg when transitioning from stance control to swing control. Sw_1 to Sw_4 trigger events within swing control (see text for details).

47

GLU, HAB, and HAD) in proportion to the errors in leg angles $\Delta \boldsymbol{\alpha} = \boldsymbol{\alpha}_{tgt} - \boldsymbol{\alpha}$ to control swing leg placement. For the frontal plane, the error is provided as muscle length feedback (L^-) from the hip abductor and adductor, HAB and HAD, interpreting the offset, l_{off}, in the length feedback signal $l_{ce,RF} - l_{off,RF}$ as a means to adjust the target angle via γ-motoneuron stimulation (not shown in Fig. 4.2-A). A similar length feedback (L^-) of the biarticular muscles spanning the hip and knee, HAM and RF, provides an estimate of the leg angle error in the sagittal plane (shown in Fig. 4.2-A).

The remaining swing leg modules control the knee to achieve ground clearance and return to leg extension when approaching the target angle (Fig. 4.2-A). Module M_7 uses velocity feedback from RF (estimating sagittal leg angular velocity $\dot{\alpha}^s$) to the monoarticular knee flexor BFSH to ensure initial knee flexion. Module M_8 uses length feedback of VAS (L^+) to monitor leg length, again interpreting the length offset $l_{off,VAS}$ as the desired minimum leg length l_{clr} which can be adjusted by γ-motoneuron activity. When VAS stretches past the offset (the leg shortens below l_{clr}) (Sw$_1$ in Fig. 4.2-B), M_8 deactivates M_7 and dampens the knee motion with positive velocity feedbacks (V^+) of VAS on RF and of BFSH on itself, accounting for the fact that muscles can only pull. (BFSH is further modulated by feedback from RF to allow the knee to passively extend when α^s approaches its target). The sagittal leg angle, α^s, is monitored simultaneously with length feedbacks of HAM and RF. When α^s as measured by HAM passes a threshold close to the target value α_{tgt}^s (Sw$_2$), M_9 begins to use positive length feedback (L^+) of HAM to decelerate the leg angular motion. At the same time, when α^s passes this target as measured by RF (Sw$_3$), M_8 is deactivated. Finally, once the leg starts to retract ($\dot{\alpha}^s > 0$, detected by velocity feedback of HAM; Sw$_4$), module M_{10} engages and uses positive length feedbacks (L^+) of the hip muscles (GLU and HFL) and the knee extensor (VAS) to extend the leg and hold it close to the targeted angle (GLU and HFL).

If a leg is selected by the supraspinal layer to switch from stance control to swing control during the double support phase, the outputs of modules M_1 and M_2 for the hip and knee muscles

are inhibited by proportional feedback of the contralateral leg force F_c to terminate stance (shown as a factor $1 - F_c$ in Fig. 4.2-B). (M_1 and M_2 remain unmodified for the ankle muscles to provide ankle push off.) At the same time, M_6 and M_7 are proportionally excited by the same contralateral force to initiate swing. The modulation with F_c guarantees that the transition from stance to swing control occurs only if the body weight transfers to the contralateral leg.

The actual equations and parameter values of the model's reflex pathways are presented in Appendices 4.A.1 and 4.A.2.

4.1.2 Supraspinal Control Layer

The supraspinal control layer adjusts the desired foot placements in swing. It selects the leg that is to transition into swing control in double support and provides to the spinal cord layer the desired minimum leg length l_{clr} for ground clearance and the desired foot placement in the form of target leg angles $\boldsymbol{\alpha}_{tgt}$ in the sagittal and frontal planes (Fig. 4.1-A). Several approaches have been proposed to compute desired foot placements for dynamic balance in 3D walking and running [129, 212, 279, 285]. We adapt the heuristic approach of [285] due to its simplicity. For instance, the desired leg angle of the left leg (L) in the sagittal plane (s) is calculated as $\alpha_{tgt,L}^{w,s} = \alpha_0^s - c_d^s \, d_L^s - c_v^s \, v_L^s$, where $\alpha_L^{w,s}$ is the angle that the sagittal hip-ankle line forms with the horizontal plane of the world frame w; α_0^s, c_d^s and c_v^s are positive constants; and d_L^s and v_L^s are the time-delayed horizontal position and velocity of the COM relative to the ankle of the right foot (Fig. 4.1-B). Four different target angles are computed accounting for the sagittal and frontal planes of the left and right leg. The resulting target angle vector $\boldsymbol{\alpha}_{tgt}^w = \left[\alpha_{tgt,L}^{w,s}, \alpha_{tgt,R}^{w,s}, \alpha_{tgt,L}^{w,f}, \alpha_{tgt,R}^{w,f} \right]^T$ is sent to the spinal layer in body frame coordinates, $\boldsymbol{\alpha}_{tgt} = \boldsymbol{\alpha}_{tgt}^w + \boldsymbol{\theta}$.

If the legs are in double support, the supraspinal layer additionally selects the leg whose control is to transition into swing based on the distance of the leg angles to their targets (Fig. 4.1-C). For each leg, the leg angle distance is calculated as $\|\boldsymbol{\alpha}_{tgt} - \boldsymbol{\alpha}\| = \sqrt{(\alpha_{tgt}^s - \alpha^s)^2 + (\alpha_{tgt}^f - \alpha^f)^2}$, and the next swing leg is chosen to be the one whose angle distance is larger, as the other leg is

better positioned to balance the trunk in stance. Both the swing leg selection and the target angle vector $\boldsymbol{\alpha}_{tgt}$ are updated continuously, allowing the supraspinal layer to react to disturbances throughout the gait cycle.

4.2 Generation of Human Locomotion Behaviors

Whether the proposed reflex circuitry reproduces human walking behavior is first confirmed (Sec. 4.2.1). Then the contributions of the individual control modules are explored (Sec. 4.2.2). Finally, the versatility of the reflex circuitry in generating other locomotion behaviors by supraspinal modulation is demonstrated (Sec. 4.2.3).

4.2.1 Quality of Walking Behavior

The reflex circuitry generates walking with overall human-like kinematics, dynamics and muscle activation patterns, although the metabolic energy optimization leads to a lower quality match than obtained with parameters tuned to match kinematic data in the Geyer's 2D model [88]. Fig. 4.3 shows the joint kinematics and dynamics and the GRFs obtained from optimizing the control parameters with the cost function (eq. (3.24)) for a normal human walking speed of $1.2 \mathrm{~m\,s}^{-1}$. Some differences compared to the human walking patterns are introduced by the simplified structure of the skeletal model. For instance, the reduction of the entire upper body to a rigid segment neglects soft, force-buffering structures in the human trunk and leads to higher impact forces and larger trunk motions after heel strike (Fig. 4.3-(i)). Also, the lack of a toe segment results in more plantar flexion in late stance (ii). These differences (i and ii) have also been observed in the Geyer's model [88]. However, the energy optimization introduces additional differences. The model now tends to straighten the knee early in stance (iii), known to generate more energy-efficient solutions in gait optimization [1, 258]. The early straightening induces less dorsiflexion at the ankle and excessive roll at the hip (iv). Both differences (iii) and (iv) are not

50
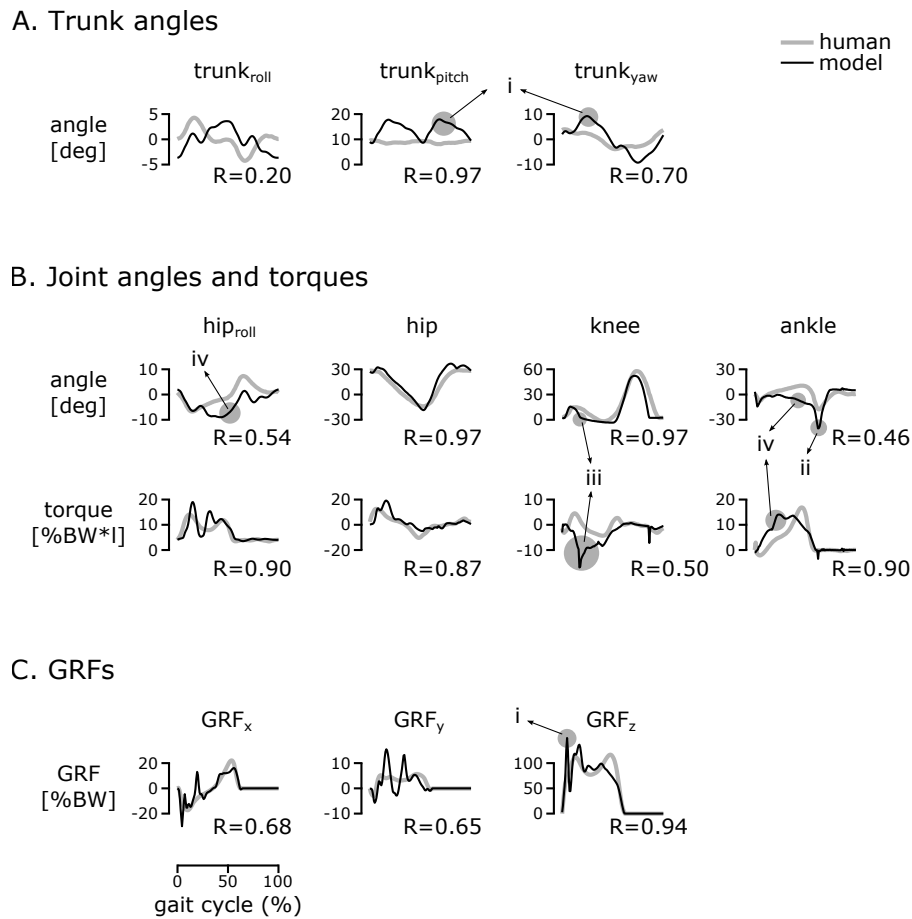
Figure 4.3: Comparison of kinematics and dynamics for walking at 1.2 m s^{-1} in humans (gray traces) and the 3D neuromechanical model (black traces) over a normalized gait cycle. Stance lasts from 0% to about 60%. The panels show the roll, pitch and yaw of the trunk with respect to the world frame (A), the leg joint angles and torques (B), and the ground reaction forces in foreaft (x), mediolateral (y), and vertical directions (z) (C). The gray areas (iiv) highlight key differences between model and human data. Human data are adapted from [216] (angles), [75] (torques) and [59] (GRFs). (R: cross-correlation values [278])

observed when the model is optimized to match the reference kinematics instead of minimizing the energetic cost (not shown).

With the exception of HAD, the correlation coefficients between predicted and observed activation patterns lie within the range found in human experiments (average $R = 0.40 \sim 0.81$ for inter-subject comparison, [278]) (Fig. 4.4-A and B). Compared to the previous 2D model, the energy optimization slightly reduces the quality of the match for the ankle muscles (SOL,

GAS and TA; $R \geq 0.80$). On the other hand, the functionally improved spinal circuitry leads to a better match for HFL throughout the gait cycle ($R = 0.86$), now generates VAS activity in stance preparation at the end of swing, and captures the overall activation patterns of the added muscles BFSH and RF, although the onset of RF activity is late by about 10% of the gait cycle. The largest difference between predicted and observed activity occurs for the added HAD ($R = 0.32$), whose exclusive action on the hip roll DOF in the model probably over-simplifies the action and control of hip adductors in humans.

While the quality of the fit improves by including, for instance, reference kinematics in the optimization goals, energy optimization provides a sufficient cost criterion to generate overall
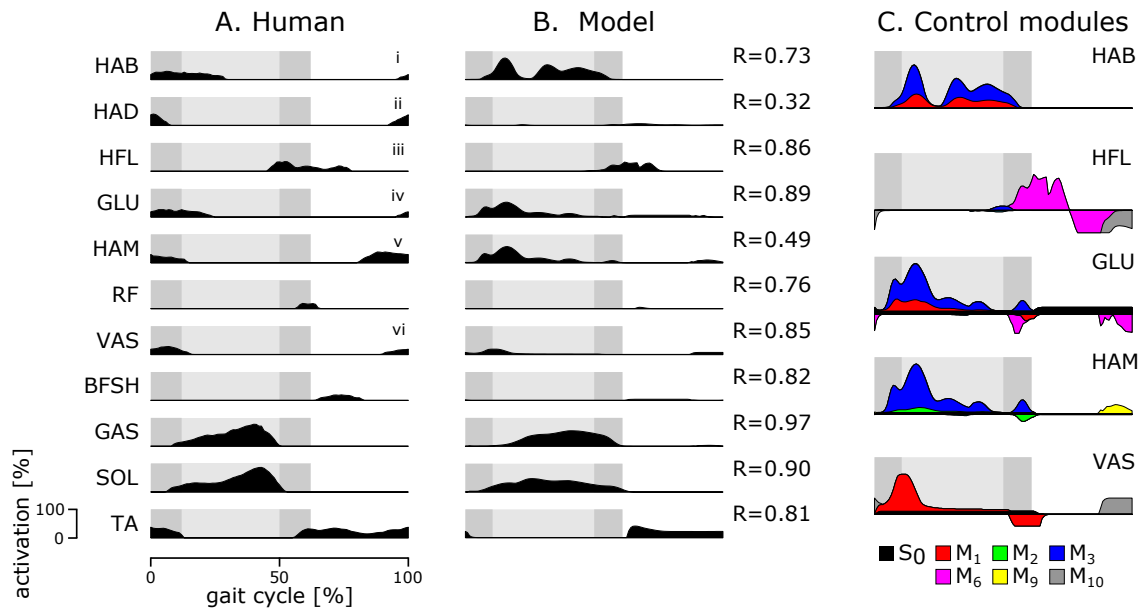
Figure 4.4: Comparison of muscle activations in normal walking. The left panel shows the human muscle activations for the 11 muscle groups of the model estimated from low-pass-filtered surface EMG (A, adapted from [205]); the center panel shows the model-predicted muscle activations with coefficients of correlation (R) between model and human data (B); and the right panel shows the contributions of individual control modules M_i to the activation of selected muscles (C). Net activation in the center panel is the sum of the contributions and saturated within 0% and 100%. Shaded backgrounds indicate stance phase with double supports in a darker hue. (Compared muscles: (i) gluteus medius, (ii) adductor magnus, (iii) adductor longus, (iv) gluteus maximus, (v) semimembranosus, (vi) vastus lateralis; R: cross-correlation value; S_0: prestimulation contribution)

human locomotion behavior without requiring reference data. It thus allows us to explore the behaviors that the spinal control circuitry can produce.

4.2.2 Contributions of Individual Reflex Modules

The spinal modules combine to shape the activation patterns of individual muscles in ways that can obscure the interpretation of EMGs in experiments (Fig. 4.4-C). Some modules contribute similarly to a muscle's activation. For instance, the modules for compliant stance leg behavior (M_1) and trunk balance (M_3) contribute similar activation profiles for HAB, suggesting that a single peak of EMG activity in humans does not have to equal a single functionality. The peak can instead result from executing multiple functional goals at the same time. Other modules compete. The HAM activity in the late double support is nearly flat (Fig. 4.4-B), because the excitation provided by the balance module M_3 is suppressed by module M_2, which protects against knee hyperextension (Fig. 4.4-C). Thus, it can be misleading to equate flat muscle EMGs with the absence of control. Finally, the late swing activities of HAM and VAS provide an example in which apparently similar activation features across muscles are generated by different control modules (the stopping module M_9 for HAM and the leg-holding module M_{10} for VAS).

Not all of the proposed control modules seem to contribute to steady walking, however. To test if they matter, the neuromechanical model is subjected to disturbances. The model is trained (or optimized) on rough terrain (Fig. 4.5; 40 m long track with random height changes up to
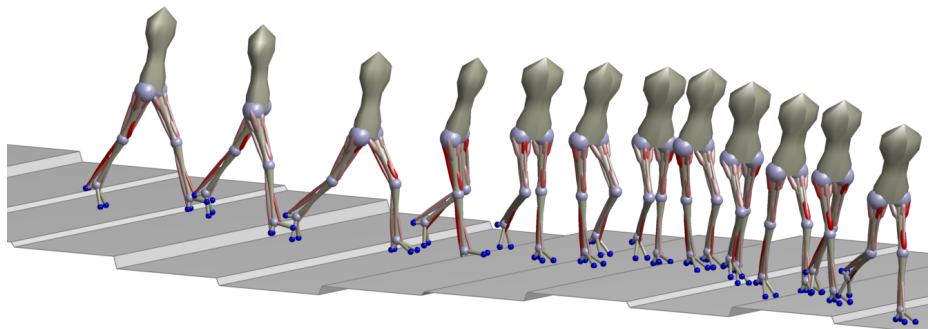
Figure 4.5: Robust walking on rough terrains. The model can walk blindly on a rough terrain with $\pm$ 10 cm.

ground tolerance

roughness [cm]	±0	±2	±4	±6	±8	±10
survival rate [%]	100	90	80	55	15	0

push resistance

time [% gait cycle]	0	10	20	30	40
forward [Ns]	54	32	52	54	72
backward	50	36	54	86	82
medial	26	12	10	24	18
lateral	12	8	10	32	50

Table 4.1: Ground tolerance and push resistance of the neuromechanical controller trained on a ±10cm-terrain. Shown are the survival rate on 20 randomly generated test terrains of different maximum step size (top) and the largest impulse (variable force, fixed time interval of 200 ms) that can be applied to the pelvis in different directions and times of the gait cycle (bottom).

±10 cm during the middle 20 m portion) with the cost function eq. (3.24), searching for energy-efficient walking that can tolerate disturbances. We find that the trained control is robust enough to let the model traverse randomly generated terrains (success rate $>50\%$ up to ±6 cm terrains) as well as withstand substantial horizontal pushes (Table 4.1) with a steady state gait that is slightly faster than before (1.4 m s^{-1} vs. 1.2 m s^{-1}) and less energy optimal (metabolic cost of 6.2 J kg^{-1} m^{-1} vs. 5.0 J kg^{-1} m^{-1}). Note that the model can be trained to walk on rougher terrain, but the resulting gait clearly deviates from normal locomotion and is not investigated here. We then subject the trained model to walking on flat and rough terrain and record the peak muscle activations that each module contributes.

The comparison shows that some swing leg modules which do not seem needed in steady walking become important when rejecting disturbances (Fig. 4.6). At no instant in steady walk-ing (gray bars) did the modules M_4, M_7 and M_{10} contribute more than 2% of activation to any muscle. All three modules are related to swing leg control with M_7 supporting early knee flex-
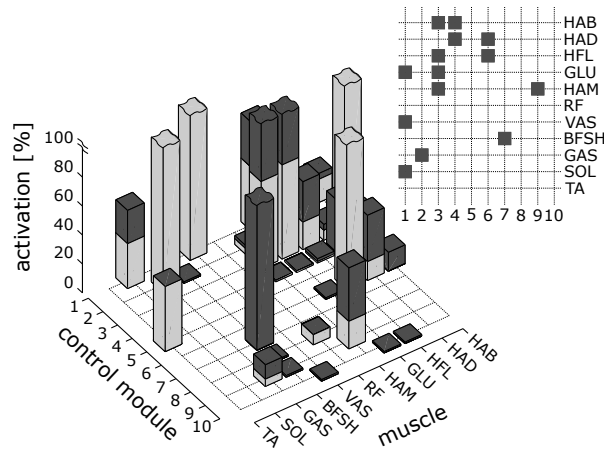
Figure 4.6: Contributions of reflex modules to individual muscle activations. The contributions of the reflex modules are investigated while walking on rough and flat terrain with same control parameters. Peak contributions of the modules to individual muscle activations in steady (gray) and disturbed walking (on rough terrain, black) are compared at the right. Control modules with peak increases of more than 20% are indicated in the right top grid.

ion, M_{10} holding the leg before stance, and M_4 compensating for moments induced on the trunk (Fig. 4.2). Their negligible activities reveal that the optimization converged on an energy-efficient solution with a nearly passive knee in swing. Although this ballistic walking style [174] makes these modules seem unneeded, they become highly active in rough terrain (black bars), playing a major part in placing the swing leg (M_7, encountered peak activation of 100%) and stabilizing the trunk (M_4, 36% peak activation). Module M_{10} is the exception. It does not meaningfully increase peak activity (1%), suggesting that the human stance preparation of hip and knee extensors [205] is not critical to gait robustness.

4.2.3 Behavior Diversity

The proposed spinal control modules are sufficient to generate a range of steady and unsteady locomotion behaviors observed in humans (Fig. 4.7). Characteristic human locomotion behaviors range from walking and running to stair and slope negotiation to turning and deliberate obstacle avoidance. Optimization for different terrains with the cost function eq. (3.24) identifies control

parameter sets that generate steady behaviors, including slope ascent ($\leq$8%) and descent ($\leq$24%) as well as stair ascent (10 cm risers with 40 cm treads). With different target speeds in eq. (3.24c), the control network further generates walking at speeds ranging from 0.8 m s^{-1} to 1.8 m s^{-1} (not shown), which covers human slow and fast walking [182], and running steps at 3 m s^{-1}, although the model falls after about 20 m (Fig. 4.7-A). In addition, using different constant parameter sets for the left and right leg (and replacing the velocity term in cost function in eq. (3.24c) with a cost term that seeks to maximize the change in trunk yaw), the control generates steady turning motions with the smallest radius of about 6.5 m. (The lack of yaw joints in the hips of the model probably prevents smaller radii as it has to slide about the stance foot to produce yaw motion. This shortcoming affects the performance of most behaviors. In humans, the internal yaw joints of the hips and trunk are used even in normal walking [245]. It is likely that adding these internal DOFs would help the model to achieve sharper turns, a larger range of walking speeds, and stable running (see below). For example, in the 2D sagittal plane, where yaw stabilization is not required, the model can generate stable running with speed changes between 2.4~4.0 ms^{-1} [241].)

To test whether the control architecture of the spinal modules produces unsteady locomotion behaviors, we allow the optimization to change the control parameter sets at heel strike between individual steps (Fig. 4.7-B). With two such step changes in the control parameters, the model can make large changes in walking speed from 0.8 m s^{-1} to 1.7 m s^{-1} and from 1.8 m s^{-1} to 1.1 m s^{-1}, and change the walking direction with a maximum turning angle of 50 deg. In both cases, the speed and direction changes appear only after the steps with the control parameter changes, suggesting that earlier steps should not be overlooked in gait analysis when studying these behaviors. Expanding the control changes to multiple steps, the model can also avoid obstacles by increasing the foot ground clearance or the step size. For example, in the sequence shown in Fig. 4.7-B, the model approaches from steady walking, passes within eight steps of altered control a 10 cm high obstacle followed by a 75 cm wide obstacle and then returns to

56

A. Steady behavior
ascend and descend slopes

8%

24%

turn

ascend stairs

40 cm

10 cm

run

3.0 ms⁻¹

20 m
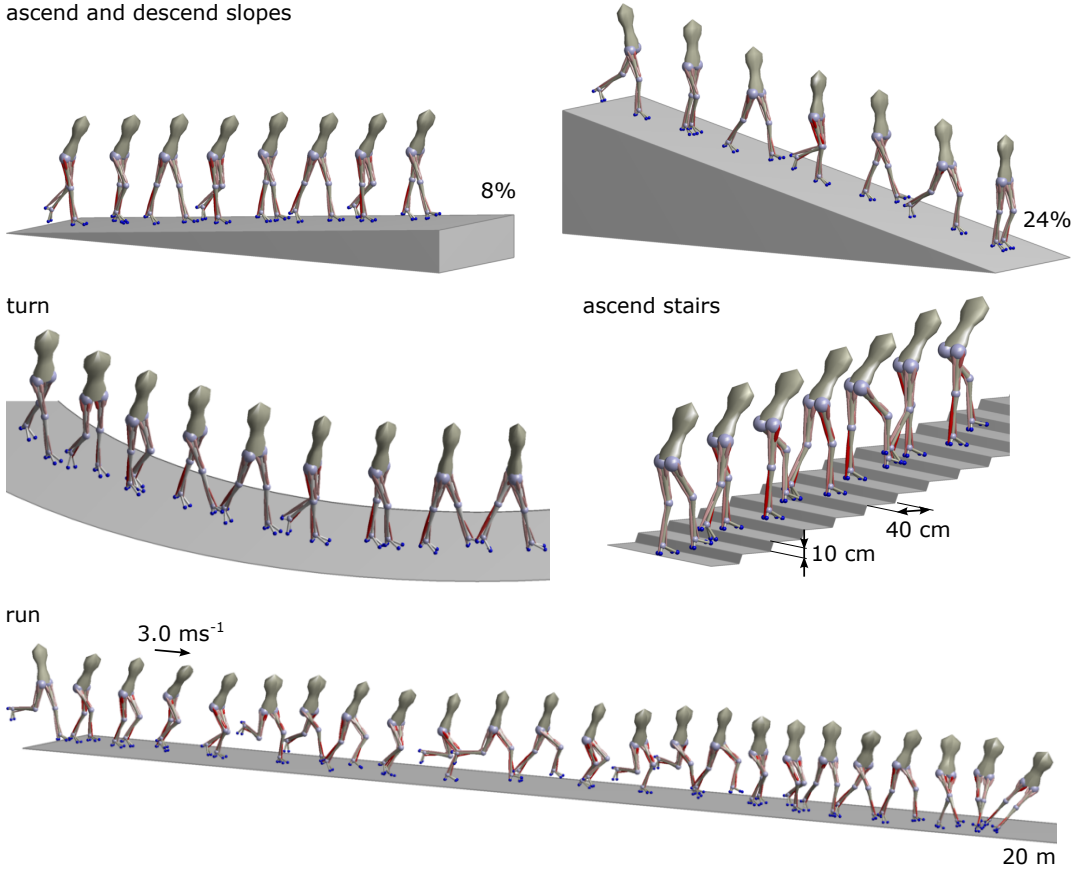
B. Step-to-step modulation
increase and decrease speed

0.8 ms⁻¹   2-step

1.7 ms⁻¹

1.8 ms⁻¹   2-step

1.1 ms⁻¹

turn

2-step

50°

avoide obstacle

8-step

10 cm

75 cm
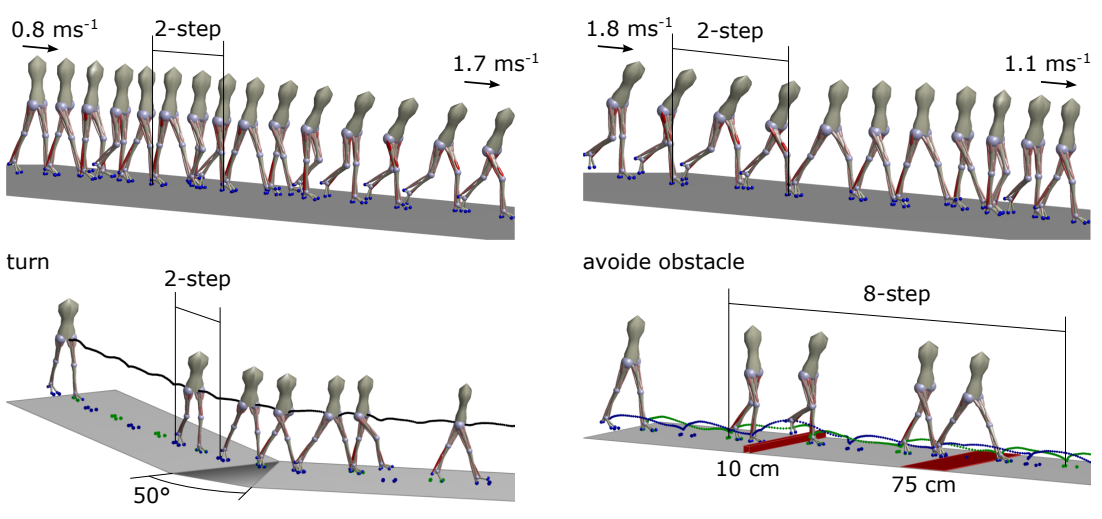
Figure 4.7: Behavior diversity. Snapshots of the human neuromechanical model during steady (A) and transitional behaviors (B) are shown.

57

steady walking.

Except for stair walking and running, all steady and unsteady behaviors have been generated without changing individual muscle reflex parameters in swing. It is sufficient to keep the swing reflex parameters used for energy-efficient walking, and to generate the different swing leg behaviors by altering the supraspinal commands of the desired minimum leg length, l_{clr}, and the desired target leg angle, α_{tgt}. (note: Since only the swing leg control is structured in a hierarchy with few supraspinal parameters, we always allowed the optimization to change all stance reflex parameters.) For instance, down slope walking was generated using the smallest desired leg length, l_{clr} = 75 cm, whereas normal walking used l_{clr} = 87 cm. Similarly, target angles ranged from α_{tgt}^s = 59 deg in fast walking to α_{tgt}^s = 72 deg for descending slopes. In contrast, for walking upstairs and running adjusting only l_{clr} and α_{tgt} was insufficient. For these behaviors, the gains of the feedback pathways which stimulate HFL in M_6 needed to be largely increased, because a stronger hip swing is required to lift the thigh up in walking upstairs and to rapidly advance the leg in running. This additional adjustment suggests that the intensity of the swing should be part of the supraspinal control layer.

The optimization did not find a solution for walking down stairs (10 cm risers and 40 cm treads), pointing to a limitation of the current stance leg control. To lower the COM down stairs, leg propulsion in late stance needs to be tempered, which could be achieved by lowering the feedback gains in module M_1 during the late stance phase. However, this gain adjustment will require organizing the stance control into a hierarchy with supraspinal modulation.

Changes in the optimized reflex gains for the different behaviors reveal several functional candidates for such a supraspinal modulation of the stance control. One candidate for supraspinal modulation is the target trunk lean, θ_{tgt}, in the balance module M_3. For instance, walking up stairs required a target trunk pitch of θ_{tgt}^s = 22 deg as compared to 2~7 deg for all other behaviors. Including the target trunk lean in the supraspinal control layer seems a natural choice given that it is related to the vestibular and vision systems. Another candidate is the modulation of the force

feedback gain of VAS, which tends to increase for walking behaviors with higher leg impacts (walking fast, on down slope, or on rough terrain). The force feedback of VAS is part of module M_1 responsible for generating compliant leg behavior. Changing the VAS gain will change the leg stiffness, a functional adaptation important to human locomotion [84, 152].

4.3 Implications of the Model

The primary goal of the model is to investigate to what extent the central questions of "**how does the lower layer controller generate the motor stimulations?**" and "**how is the lower layer controller modulated by the higher layer control to realize different locomotion tasks?**" can be answered with a spinal-reflex-based controller. The proposed controller without any time-based control component, or CPGs, generates human-like walking kinematics, dynamics and muscle activations. Furthermore, the model can generate diverse locomotion behaviors including walking and running, acceleration and deceleration, slope and stair negotiation, turning, and deliberate obstacle avoidance. The results suggest an answer to the first question: **"the motor stimulations of many human locomotion behaviors can be generated by chains of reflexes in the lower layer controller."**

The second question is addressed in part by the swing leg controller. The swing leg controller consists of two layers, where the higher-layer brain controller sends commands about where and how to place the swing foot (through the commands of desired foot placement, $\boldsymbol{\alpha}_{tgt}$, and minimum swing leg length, l_{clr}), and the lower-layer spinal controller generates muscle activations based on these commands. With this hierarchical structure, the model is able to generate different locomotion behaviors without changing the control parameters of the lower-layer swing leg controller. Such result suggests an answer to the second question: **"different locomotion behaviors can be realized by a unified spinal controller that is modulated by the higher-layer control through a few high-level commands."** This is opposed to control structures, where the higher-layer brain control is directly engaged at the level of generating muscle activations, or

59

where multiple sets of lower-layer controllers are switched for different locomotion tasks. Hierarchizing the entire lower-layer control and developing a higher-layer control that modulates the lower-layer control based on high-level tasks and environmental cues remains for future work.

4.4 Future Work

The main part that remains as future work is to complete the hierarchical controller that can generate diverse locomotion behaviors based on high-level tasks and environmental cues, as hypothesized for biological controllers (Sec. 2.1.2, Fig. 2.2). As discussed in the previous section, in the current model, only the swing leg control is partially in such hierarchical structure. Towards this goal 1) the lower-layer should be able to generate desired locomotion behaviors from a few control commands, and 2) the higher-layer should generate these few control commands accordingly to realize the high-level tasks and to adapt to the environment (Fig. 4.8).

First, we propose to select the control commands for the lower-layer control based on functional principles of legged locomotion. Previously, we constructed a walking speed controller by selecting key control parameters that show meaning trends across targeted walking speeds as the control commands [238]. With such approach, nine selected control commands enabled the model to generate rapid speed changes between $0.8 \mathrm{~m~s^{-1}}$ and $1.8 \mathrm{~m~s^{-1}}$. However, it is not clear if the same key parameters can be used to generate other behaviors such as walking up and down slopes; if not, then more parameters should be added which increases the action space. Instead of selecting from the lower layer control parameters, one can adapt the lower layer control to operate with a few parameters that functionally suffices the generation of diverse locomotion behaviors. The current swing leg control is an example, which can be modulated for many locomotion behaviors by target foot placement (α_{tgt}) and minimum swing leg length (l_{clr}). Based on our previous studies, we suggest the following control commands for the full control: desired trunk angle (θ_{tgt}) and energy change along the vertical and horizontal axes (ΔE_v and ΔE_h) for the stance leg control; target foot placement (α_{tgt}), minimum swing leg length (l_{clr}), and swing
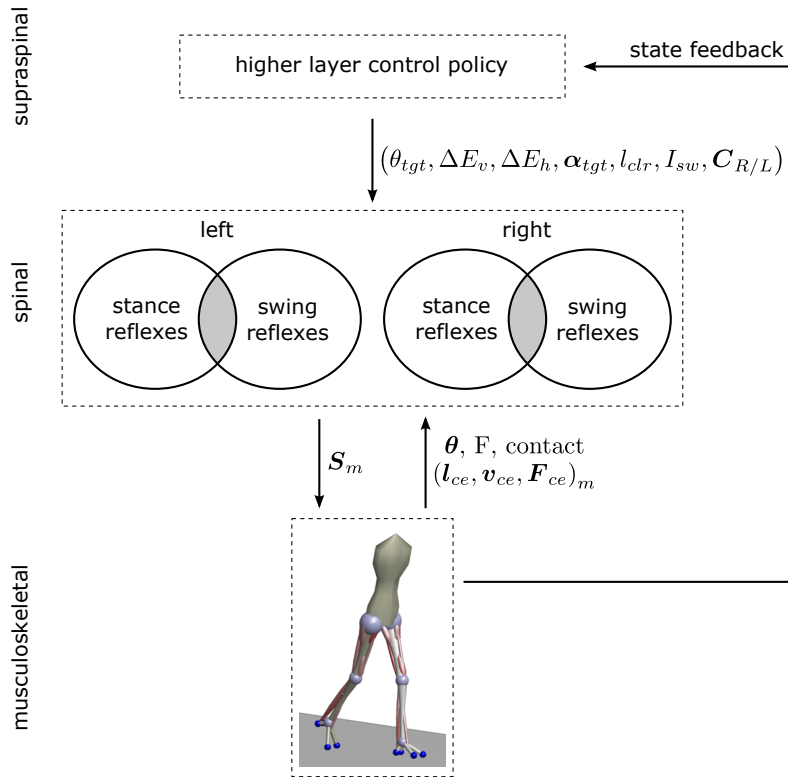
Figure 4.8: Full hierarchical neural controller. I propose to complete the hierarchical control structure and explore control policies for the higher layer controller using machine learning techniques. The targeted behaviors of the hierarchical neural controller include speed changes in and gait transitions between walking and running as well as following commanded footsteps.

intensity (I_{sw}) for the swing leg control; and the control mode of each leg ($\boldsymbol{C}_{R/L}$) (Fig. 4.8).

Given the lower-layer controller that can be modulated with a few control commands, the higher-layer controller should map specific values for these control commands to desired locomotion tasks and environmental cues. One option for this mapping is to use a giant lookup table, which we have used to successfully control running speed and height of a simple neuromechanical hopper on rough terrains [235] (Fig. 4.9-A). However, this approach is susceptible to the so-called curse of dimensionality (a generous calculation on the minimum size of the table, which neglects the environmental cues and considers simplified states with resolution of $R = 10$, results in $R^{\#S} \times R^{\#S} \times \#A \approx 10^{96}$, where $\#S \approx 47$ and $\#A \approx 100$ represent the number of states and control parameters, respectively), which limits us from applying this method to more complex
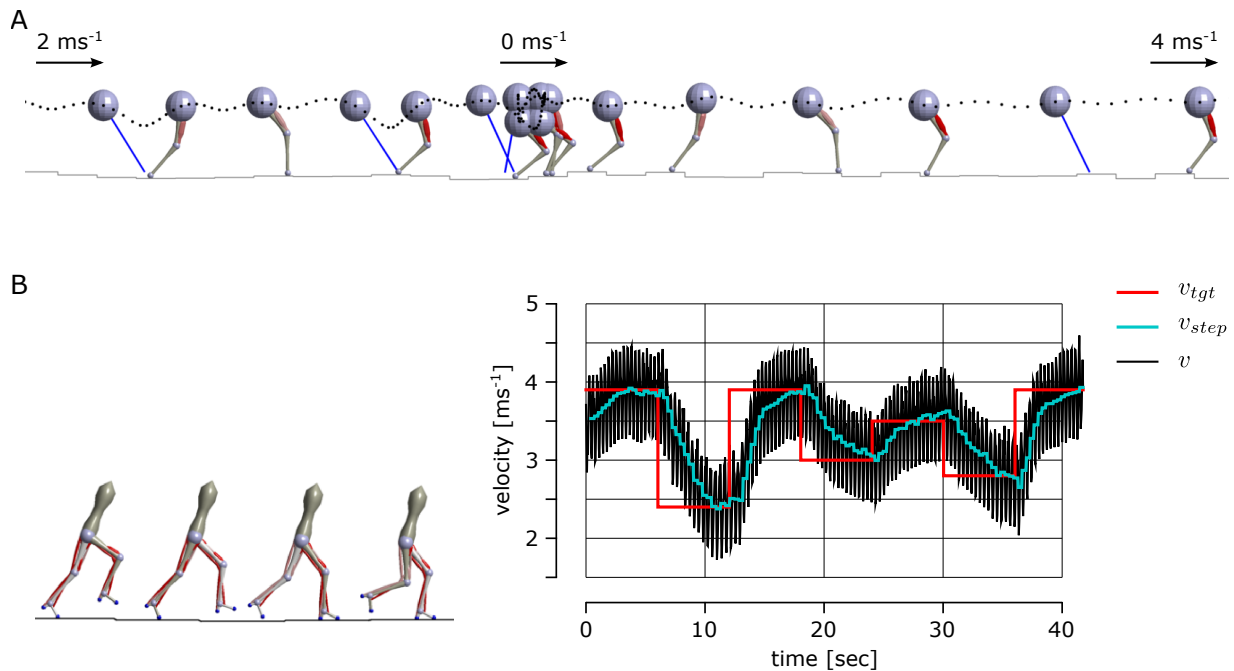
Figure 4.9: Towards a versatile higher-level control model. A. Running speed and height control of a simple neuromechanical hopper. With a lookup table that maps the full state-to-state of the simple hopper, the model can control running on unknown rough terrains. B. Running speed control of the neuromechanical model with a higher layer linear policy. The plot on the right shows the human model (on the left) tracking target velocity that arbitrarily changes every 6 seconds between 2.4 m s^{-1} and 3.9 m s^{-1}. Speed changing strategy of modulating the trunk lean is running in parallel with the linear speed adaptation policy. (v_{step}: average velocity for one step; v: instantaneous velocity)

models as our current human model. Therefore, some sort of function approximation instead of a lookup table seems necessary. We also have explored this direction using a linear function that maps desired running speeds to the lower-layer control parameters [241] (Fig. 4.9-B). With addition control components that facilitate speed changes, the human neuromechanical model could generate acceleration and deceleration of about ± 0.35 m s^{-2} between running speeds of 2.4 m s^{-1} and 4.0 m s^{-1}. However, to fully use the capacity of the lower-layer controller, a full state-action-state mapping should be explored, where the states include the state of the human system as well as the environmental cues.

Therefore, we propose to use more general function approximators such as deep neural

networks to model the higher-layer brain control. These general function approximators can be trained without human data using reinforcement learning techniques such as value iteration [208] and policy iteration [147]. These techniques have been used to control simulation legged-characters, in the graphics community [53, 203]. Especially, using deep reinforcement learning techniques [172, 173], which seem to be applicable to high-dimensional continuous action and state spaces that include detailed representation of the environment and full control parameters of the lower-layer control [204], one can first develop a black box controller with desired capabilities and reverse engineer functional principles from the developed controller (ex. the few control commands for the lower-layer controller). On the other hand, one can use supervised learning techniques to develop control models that closely reproduce existing gait data (including those generated by simulations), which have been explored for graphical characters and robots [150, 177, 178]. Moreover, incorporating human gait data using supervised learning in the development of neuromechanical control models can lead us to a new direction of studying human control [82].

4.A   Appendices

4.A.1   Reflex control equations

This appendix presents the actual equations that implement the reflex pathways described in Section 4.1.1. The values of the control parameters used for several locomotion behaviors are shown in Appendix 4.A.2.

Reflex pathways that are frequently used in the control network include force feedback ($^{F}\mathbf{p}_{SRC}^{TGT,i}$), length feedback ($^{L}\mathbf{p}_{SRC}^{TGT,i}$), velocity feedback ($^{\pm V}\mathbf{p}_{SRC}^{TGT,i}$), proportional-derivative feedback ($_{\theta_{tgt}}^{PD}\mathbf{p}_{\pm\theta}^{TGT,i}$), and co-stimulation ($^{S}\mathbf{p}_{SRC,j}^{TGT,i}$). The general structures of these pathways are

shown below:

$$
{}^{F}\mathbf{p}_{SRC}^{TGT,i} = {}^{F}G_{SRC}^{TGT,i}\bar{F}_{mtu,SRC}\left(t - \Delta t\right)
$$

$$
{}^{L}\mathbf{p}_{SRC}^{TGT,i} = {}^{L}G_{SRC}^{TGT,i}\left[\bar{l}_{ce,SRC}\left(t - \Delta t\right) - \bar{l}_{off,SRC}^{TGT,i}\right]_{+}
$$

$$
{}_{\pm\alpha_{tgt}}^{L}\mathbf{p}_{SRC}^{TGT,i} = {}_{\alpha_{tgt}}^{L}G_{SRC}^{TGT,i}\left[\bar{l}_{ce,SRC}\left(t - \Delta t\right) - \left\{1 \pm C_{SRC}^{\alpha}\left(\alpha_{tgt}\left(t - \Delta t\right) - \alpha_{0,SRC}\right)\right\}\right]_{+}
$$

$$
{}^{\pm V}\mathbf{p}_{SRC}^{TGT,i} = {}^{V}G_{SRC}^{TGT,i}\left[\pm\bar{v}_{ce,SRC}\left(t - \Delta t\right)\right]_{+}
$$

$$
{}_{\theta_{tgt}}^{PD}\mathbf{p}_{\pm\theta}^{TGT,i} = \left[\pm{}^{P}G_{\theta}^{TGT,i}\left(\theta\left(t - \Delta t\right) - \theta_{tgt}\right) \pm {}^{D}G_{\dot{\theta}}^{TGT,i}\dot{\theta}\left(t - \Delta t\right)\right]_{+}
$$

$$
{}^{S}\mathbf{p}_{SRC,j}^{TGT,i} = {}^{S}G_{SRC}^{TGT,i}S_{SRC,j}
$$

$$
{}_{S_{thr}}^{[S]_{+}}\mathbf{p}_{SRC,j}^{TGT,i} = {}^{[S]_{+}}G_{SRC}^{TGT,i}\left[S_{SRC,j} - S_{thr,SRC}\right]_{+},
$$

where the left superscript indicates the type of the pathway, the right superscript specifies the target muscle (TGT) stimulated by the pathway and the control module (i) the pathway belongs to. The right subscript shows the signal origin as either the source muscle (SRC) or the trunk lean θ. In addition, for the length and co-stimulation pathways a left subscript indicates feedback modulation by either the swing-leg target angle ($_{\pm\alpha_{tgt}}^{L}\mathbf{p}_{SRC}^{TGT,i}$) or the co-stimulation threshold ($_{S_{thr}}^{[S]_{+}}\mathbf{p}_{SRC,j}^{TGT,i}$). The symbol $[\cdots]_{+}$ indicates that only the positive values of the term in the bracket are used. The feedback data of muscle force ($\bar{F}_{mtu} = \frac{F_{mtu}}{F_{max}}$), length ($\bar{l}_{ce} = \frac{l_{ce}}{l_{opt}}$) and velocity ($\bar{v}_{ce} = \frac{v_{ce}}{v_{max}}$) are normalized to their nominal values. With this notation system, the reflex pathways that generate the muscle stimulations are given below for each muscle individually:

HAB

$$
S_{HAB,1} = {}^{F}\mathbf{p}_{HAB}^{HAB,1}
$$

$$
S_{HAB,3} = {}_{0}^{PD}\mathbf{p}_{-\theta f}^{HAB,3}
$$

$$
S_{HAB,4} = {}^{S}\mathbf{p}_{HAB_C}^{HAB,4}
$$

$$
S_{HAB,6} = {}_{\alpha_{tgt}^{f}}^{L}\mathbf{p}_{HAB}^{HAB,6}
$$

HAD

$$
S_{HAD,3} = {}_{0}^{PD}\mathbf{p}_{\theta f}^{HAD,3}
$$

$$S_{HAD,4} = {}^{S}\mathbf{p}_{HAD_C}^{HAD,4}$$

$$S_{HAD,6} = {}_{-\alpha_{tgt}^{f}}^{L}\mathbf{p}_{HAD}^{HAD,6}$$

HFL

$$S_{HFL,3} = {}_{\theta_{tgt}^{s}}^{PD}\mathbf{p}_{-\theta^{s}}^{HFL,3}$$

$$S_{HFL,4} = {}^{S}\mathbf{p}_{GLU_C}^{HFL,4} + {}^{S}\mathbf{p}_{HAM_C}^{HFL,4}$$

$$S_{HFL,6} = {}_{\alpha_{tgt}^{s}}^{L}\mathbf{p}_{RF}^{HFL,6} - {}^{-V}\mathbf{p}_{RF}^{HFL,6}$$

$$S_{HFL,10} = {}_{\alpha_{tgt}^{s}}^{L}\mathbf{p}_{HFL}^{HFL,10}$$

GLU

$$S_{GLU,1} = {}^{F}\mathbf{p}_{GLU}^{GLU,1}$$

$$S_{GLU,3} = {}_{\theta_{tgt}^{s}}^{PD}\mathbf{p}_{\theta^{s}}^{GLU,3}$$

$$S_{GLU,4} = {}^{S}\mathbf{p}_{HFL_C}^{GLU,4} + {}^{S}\mathbf{p}_{RF_C}^{GLU,4}$$

$$S_{GLU,6} = {}_{-\alpha_{tgt}^{s\Delta}}^{L}\mathbf{p}_{HAM}^{GLU,6} - {}^{-V}\mathbf{p}_{HAM}^{GLU,6}$$

$$\text{where } \alpha_{tgt}^{s\Delta} = \alpha_{tgt}^{s} + \alpha_{\Delta}^{s}$$

$$S_{GLU,10} = {}_{-\alpha_{tgt}^{s}}^{L}\mathbf{p}_{GLU}^{GLU,10}$$

HAM

$$S_{HAM,2} = {}^{F}\mathbf{p}_{HAM}^{HAM,2}$$

$$S_{HAM,3} = {}^{S}\mathbf{p}_{GLU,3}^{HAM,3}$$

$$S_{HAM,4} = {}^{S}\mathbf{p}_{GLU,4}^{HAM,4}$$

$$S_{HAM,9} = {}_{-\alpha_{tgt}^{s\Delta}}^{L}\mathbf{p}_{HAM}^{HAM,9}$$

RF

$$S_{RF,8} = {}^{V}\mathbf{p}_{VAS}^{RF,8}$$

VAS

$$S_{VAS,1} = {}^F\mathbf{p}_{VAS}^{VAS,1}$$

$$S_{VAS,2} = -{}^L\mathbf{p}_{BFSH}^{VAS,2}$$

$$S_{VAS,10} = {}^L\mathbf{p}_{VAS}^{VAS,10}$$

BFSH

$$S_{BFSH,2} = {}^L\mathbf{p}_{BFSH}^{BFSH,2}$$

$$S_{BFSH,7} = {}^{-V}\mathbf{p}_{RF}^{BFSH,7}$$

$$S_{BFSH,8} = {}^V\mathbf{p}_{BFSH}^{BFSH,8} M^L M^V$$

where $M^L = \frac{1}{C_{RF}^\alpha} \left[l_{ce,RF}(t - \Delta t_1) - \left\{ 1 + C_{RF}^\alpha \left(\alpha_{tgt}^s(t - \Delta t_2) - \alpha_{0,RF} \right) \right\} \right]_+$

and $M^V = \left[\frac{1}{C_{BFSH}^\alpha} v_{ce,BFSH}(t - \Delta t_3) + \frac{1}{C_{RF}^\alpha} v_{ce,RF}(t - \Delta t_4) \right]_+$

$$S_{BFSH,9} = {}_{S_{thr,HAM}}^{[S]_+}\mathbf{p}_{HAM,9}^{BFSH,9}$$

GAS

$$S_{GAS,2} = {}^F\mathbf{p}_{GAS}^{GAS,2}$$

$$S_{GAS,9} = {}_{S_{thr,HAM}}^{[S]_+}\mathbf{p}_{HAM,9}^{GAS,9}$$

SOL

$$S_{SOL,1} = {}^F\mathbf{p}_{SOL}^{SOL,1}$$

TA

$$S_{TA,5,st} = {}^L\mathbf{p}_{TA}^{TA,5,st} - {}^F\mathbf{p}_{SOL}^{TA,5}$$

$$S_{TA,5,sw} = {}^L\mathbf{p}_{TA}^{TA,5,sw}$$

where $S_{TA,5,st}$ and $S_{TA,5,sw}$ are active during stance and swing, respectively.

The trigger events ($\text{Sw}_1 \sim \text{Sw}_4$ in Fig. 4.2) of the swing leg control are modeled as:

$$\text{Sw}_1: \ l_{ce,BFSH}(t - t_m) \leq \left\{1 + C^\varphi_{BFSH}\left(\varphi_{knee,tgt}\left(t - (t_{ss} + t_s)\right) - \varphi_{0,BFSH}\right)\right\}$$

$$\text{Sw}_2: \ l_{ce,HAM}(t - t_s) \geq \left\{1 - C^\alpha_{HAM}\left(\alpha^{s\Delta}_{tgt}\left(t - (t_{ss} + t_s)\right) - \alpha_{0,HAM}\right)\right\}\left[\|\,\text{Sw}_1\right]$$

$$\text{Sw}_3: \ l_{ce,RF}(t - t_s) \leq \left\{1 + C^\alpha_{RF}\left(\alpha^{s}_{tgt}\left(t - (t_{ss} + t_s)\right) - \alpha_{0,RF}\right)\right\}\left[\|\,\text{Sw}_1\right]$$

$$\text{Sw}_4: \ v_{ce,HAM}(t - t_s) \leq 0 \left[\|\,\text{Sw}_2\right],$$

where $\varphi_{knee,tgt}$ is calculated from l_{clr}, and $[\|\,\text{Sw}_1]$ in Sw_2, for example, indicates that Sw_2 gets triggered only if Sw_1 is already triggered in the swing phase.

4.A.2   Control parameter values

This appendix presents the control parameter values used for locomotion behaviors of normal walking (Sec. 4.2.1), robust walking (Sec. 4.2.2), fast and slow walking, walking on inclined and declined slopes, and running (Sec. 4.2.3). The control parameter values are reported in Table 4.2, where their usages can be found in Appendix 4.A.1. The initial configurations of the human model for the locomotion behaviors are reported in Table 4.3. Since not all of the reported parameters are found to *robustly* generate the targeted behaviors (and that the reported values are rounded to the third decimal points), they may not successfully generate the locomotion behaviors depending on the simulation environment. Instead, these values can be used to quickly find successful parameter sets. For instance, when initializing CMA-ES with the reported parameter sets, most of the desired behaviors can be found within a few (< 10) CMA-ES generations.

	walk	robust walk	fast walk	slow walk	ascend slope	descend slope	run
supraspinal control parameters							
α_0^f [deg]	-0.295	-3.761	-0.833	-0.813	-0.692	-0.954	-0.784
c_d^f [deg m^{-1}]	26.404	0.000	17.139	19.590	15.636	20.760	7.579
c_v^f [deg (m s^{-1})$^{-1}$]	14.830	13.629	10.175	9.083	12.090	10.822	12.237
θ_{tgt}^s [deg]	2.594	7.062	3.133	2.914	2.585	3.802	4.770
α_0^s [deg]	60.652	64.448	59.198	66.286	59.587	72.148	71.879
c_d^s [deg m^{-1}]	0.054	0.188	0.066	0.061	0.068	0.073	0.035
c_v^s [deg (m s^{-1})$^{-1}$]	0.010	0.002	0.010	0.009	0.011	0.006	0.015
l_{clr} [m]	0.829	0.877	0.844	0.835	0.826	0.752	0.920
$\alpha_{tgt}^{s\Delta}$ [deg]	0.039	-	-	-	-	-	0.081
measurement parameters							
C_{HAB}^α	0.254	-	-	-	-	-	-
$\alpha_{0,HAB}$	1.205	-	-	-	-	-	-
C_{HAD}^α	0.204	-	-	-	-	-	-
$\alpha_{0,HAD}$	1.054	-	-	-	-	-	-
C_{HFL}^α	0.363	-	-	-	-	-	-
$\alpha_{0,HFL}$	2.068	-	-	-	-	-	-
C_{GLU}^α	0.363	-	-	-	-	-	-
$\alpha_{0,GLU}$	2.068	-	-	-	-	-	-
C_{HAM}^α	0.327	-	-	-	-	-	-
$\alpha_{0,HAM}$	0.758	-	-	-	-	-	-
C_{RF}^α	0.240	-	-	-	-	-	-
$\alpha_{0,RF}$	2.365	-	-	-	-	-	-
C_{BFSH}^α	0.199	-	-	-	-	-	-

$\alpha_{0,BFSH}$	2.948	-	-	-	-	-	-

spinal control parameters

HAB

$S_{HAB,0,St}$	0.004	0.001	0.004	0.004	0.004	0.004	0.005
$S_{HAB,0,Sw}$	0.004	-	-	-	-	-	0.002
$^{F}G_{HAB}^{HAB,1}$	0.237	0.389	0.317	0.356	0.376	0.000	0.308
$^{P}G_{\theta f}^{HAB,3}$	3.835	6.444	4.541	4.207	6.672	2.821	5.333
$^{D}G_{\dot{\theta}f}^{HAB,3}$	0.548	1.224	0.504	0.509	0.588	0.501	1.013
$^{S}G_{HAB_C}^{HAB,4}$	1.759	1.736	1.310	1.250	1.722	1.272	1.502
$^{L}G_{HAB}^{HAB,6}$ $_{\alpha_{tgt}^{f}}$	1.801	-	-	-	-	-	0.954

HAD

$S_{HAD,0,St}$	0.005	0.009	0.008	0.008	0.010	0.008	0.018
$S_{HAD,0,Sw}$	0.000	-	-	-	-	-	0.000
$^{P}G_{\theta f}^{HAD,3}$	0.163	0.235	0.237	0.226	0.276	0.219	0.413
$^{D}G_{\dot{\theta}f}^{HAD,3}$	0.092	0.163	0.075	0.078	0.081	0.110	0.018
$^{S}G_{HAD_C}^{HAD,4}$	0.003	0.001	0.004	0.004	0.004	0.005	0.002
$^{L}G_{HAD}^{HAD,6}$ $_{\alpha_{tgt}^{f}}$	3.784	-	-	-	-	-	2.698

HFL

$S_{HFL,0,St}$	0.001	0.001	0.001	0.001	0.001	0.001	-0.016
$S_{HFL,0,Sw}$	0.001	-	-	-	-	-	0.001
$^{P}G_{\theta s}^{HFL,3}$	0.208	0.102	0.245	0.239	0.250	0.256	0.472
$^{D}G_{\dot{\theta}f}^{HFL,3}$	0.123	0.243	0.108	0.108	0.116	0.112	0.351
$^{S}G_{GLU_C}^{HFL,4}$	0.069	0.093	0.050	0.056	0.062	0.049	0.120
$^{S}G_{HAM_C}^{HFL,4}$	0.002	0.001	0.001	0.002	0.001	0.002	0.005
$^{L}G_{RF}^{HFL,6}$ $_{\alpha_{tgt}^{s}}$	1.175	-	-	-	-	-	5.907
$^{V}G_{RF}^{HFL,6}$	0.416	-	-	-	-	-	0.160

$^{L}_{\alpha^{s}_{tgt}}G^{HFL,10}_{HFL}$	0.128	-	-	-	-	-	0.000
GLU							
$S_{GLU,0,St}$	0.032	0.023	0.033	0.032	0.033	0.047	0.005
$S_{GLU,0,Sw}$	0.065	-	-	-	-	-	0.086
$^{F}G^{GLU,1}_{GLU}$	0.188	0.802	0.371	0.395	0.452	0.250	0.310
$^{P}G^{GLU,3}_{\theta^{s}}$	0.512	0.577	0.418	0.570	0.424	0.533	2.715
$^{D}G^{GLU,3}_{\dot{\theta}^{f}}$	0.214	0.144	0.172	0.223	0.236	0.109	0.262
$^{S}G^{GLU,4}_{HFL_C}$	0.020	0.021	0.016	0.016	0.016	0.015	0.016
$^{S}G^{GLU,4}_{RF_C}$	0.052	0.098	0.048	0.058	0.060	0.061	0.087
$^{L}_{\alpha^{s}_{tgt}}G^{GLU,6}_{HAM}$	0.169	-	-	-	-	-	0.000
$^{V}G^{GLU,6}_{HAM}$	0.659	-	-	-	-	-	1.221
$^{L}_{\alpha^{s}_{tgt}}G^{GLU,10}_{GLU}$	0.283	-	-	-	-	-	0.814
HAM							
$S_{HAM,0,St}$	0.014	0.076	0.018	0.020	0.022	0.017	0.038
$S_{HAM,0,Sw}$	-0.004	-	-	-	-	-	-0.005
$^{F}G^{HAM,2}_{HAM}$	0.213	0.000	0.098	0.107	0.091	0.080	0.103
$^{S}G^{HAM,3}_{GLU,3}$	1.142	1.419	1.140	1.922	1.313	1.121	2.391
$^{S}G^{HAM,4}_{GLU,4}$	1.142	1.419	1.140	1.922	1.313	1.121	2.391
$^{L}_{\alpha^{s\Delta}_{tgt}}G^{HAM,9}_{HAM}$	13.640	-	-	-	-	-	15.603
RF							
$S_{RF,0,St}$	0.000	0.000	0.000	0.000	0.000	0.000	-0.034
$S_{RF,0,Sw}$	0.000	-	-	-	-	-	0.000
$^{L}G^{RF,8}_{VAS}$	0.040	-	-	-	-	-	0.041
VAS							
$S_{VAS,0,St}$	0.010	0.006	0.016	0.015	0.017	0.022	0.015
$S_{VAS,0,Sw}$	0.003	-	-	-	-	-	0.002

$^F G_{VAS}^{VAS,1}$	2.907	10.210	2.963	2.805	2.602	2.948	2.129
$\bar{l}_{off,BFSH}^{VAS,2}$	3.799	3.061	2.933	3.189	2.699	3.354	1.019
$^L G_{BFSH}^{VAS,2}$	0.161	0.053	0.144	0.148	0.135	0.183	0.172
$\bar{l}_{off,VAS}^{VAS,10}$	0.018	-	-	-	-	-	0.022
$^L G_{VAS}^{VAS,10}$	0.184	-	-	-	-	-	0.171

BFSH

$S_{BFSH,0,St}$	0.004	0.003	0.004	0.005	0.005	0.004	0.001
$S_{BFSH,0,Sw}$	0.044	-	-	-	-	-	0.042
$\bar{l}_{off,BFSH}^{BFSH,2}$	1.279	0.826	1.636	1.611	1.354	2.165	1.164
$^L G_{BFSH}^{BFSH,2}$	1.035	1.504	0.894	0.836	1.028	0.944	1.327
$^V G_{RF}^{BFSH,7}$	1.228	-	-	-	-	-	0.382
$^V G_{BFSH}^{BFSH,8}$	3.810	-	-	-	-	-	2.278
$^{[S]_+} G_{HAM,9}^{BFSH,9}$	0.593	-	-	-	-	-	0.000
$S_{thr,HAM}$	0.000	-	-	-	-	-	0.000

GAS

$S_{GAS,0,St}$	0.002	0.003	0.001	0.002	0.001	0.002	0.000
$S_{GAS,0,Sw}$	-0.002	-	-	-	-	-	0.007
$^F G_{GAS}^{GAS,2}$	1.422	3.015	1.362	1.332	1.983	0.887	4.689
$^{[S]_+} G_{HAM,9}^{GAS,9}$	0.140	-	-	-	-	-	0.536
$S_{thr,HAM}$	0.000	-	-	-	-	-	0.000

SOL

$S_{SOL,0,St}$	0.039	0.046	0.030	0.034	0.024	0.042	0.021
$S_{SOL,0,Sw}$	0.008	-	-	-	-	-	0.001
$^F G_{SOL}^{SOL,1}$	1.133	0.674	1.260	1.284	1.217	0.596	2.555

TA

$S_{TA,0,St}$	0.000	0.000	0.000	0.000	0.000	0.000	0.000

$S_{TA,0,Sw}$	-0.001	-	-	-	-	-	-0.001
$\bar{l}_{off,TA}^{TA,5,st}$	0.649	0.843	0.652	0.673	0.612	0.737	0.325
${}^{L}G_{TA}^{TA,5,st}$	0.037	0.000	0.000	0.000	0.000	0.000	0.000
${}^{F}G_{SOL}^{TA,5}$	0.711	0.607	0.914	0.775	0.849	0.741	0.769
$\bar{l}_{off,TA}^{TA,5,sw}$	0.432	-	-	-	-	-	0.413
${}^{L}G_{TA}^{TA,5,sw}$	0.587	-	-	-	-	-	1.647

Table 4.2: Control parameter values of diverse locomotion behaviors. The reported values are the control parameters of the supraspinal control, measurement parameters, and the spinal control. Same values for the measurement parameters, which map the length of contractile elements in muscles to joint and leg angles, are used in all behaviors. Same values for the lower-layer swing control parameters are used in all behaviors except for running.

	walk	robust walk	fast walk	slow walk	ascend slope	descend slope	run
v^f [m s^{-1}]	0.200	0.202	0.184	0.197	0.222	0.236	0.190
$\varphi^f_{R,hip}$ [deg]	-1.000	-1.046	-1.003	-1.050	-0.864	-1.119	-1.000
$\varphi^f_{L,hip}$ [deg]	-1.000	-1.066	-1.120	-0.972	-1.022	-0.937	-1.000
v^s [m s^{-1}]	1.300	1.440	1.539	1.292	1.423	1.569	3.300
$\varphi^s_{R,hip}$ [deg]	194.081	203.769	191.116	197.684	182.901	224.209	206.308
$\varphi^s_{R,knee}$ [deg]	179.115	177.357	184.881	178.794	184.296	172.617	110.558
$\varphi^s_{R,ankle}$ [deg]	85.590	84.255	76.272	84.919	105.940	31.984	70.461
$\varphi^s_{L,hip}$ [deg]	156.775	140.674	154.460	162.413	140.744	167.970	169.551
$\varphi^s_{L,knee}$ [deg]	176.606	173.535	177.039	177.207	173.428	162.249	172.813
$\varphi^s_{L,ankle}$ [deg]	100.092	101.173	105.545	100.329	102.094	92.702	103.512

Table 4.3: Initial configurations of the human model in diverse locomotion behaviors. The reported values define the joint angles and velocities of the human model at the beginning of the simulations. The left foot is placed horizontally in the world frame touching the ground surface. All the muscles are initiated to have slack tendons and have minimum activations.

Chapter 5

Model Evaluation Using Unexpected Disturbances

Most of the material of this chapter has been published in:

- Song and Geyer. Evaluation of a neuromechanical walking control model using disturbance experiments. *Frontiers in Computational Neuroscience*, 2017. [242].

In the previous chapter, a spinal-reflex-based neuromechanical control model that can generate diverse human locomotion behaviors has been proposed. The spinal circuitry of this model is plausible in that it consists of neurophysiologically plausible reflex pathways [88]. However, it may not be the only plausible model. The human nervous system receives input from a vast sensory network, and the afferent pathways that we used to embed specific functions of legged locomotion can probably be replaced by alternative pathways transmitting similar information. Moreover, some of the reflex pathways may be replaced in part by CPGs, while preserving the overall normal behavior [71]. Therefore, to genuinely evaluate the plausibility of the model a more in-depth comparison to experimental results is required.

Disturbance reactions provide such a more in-depth comparison. Studying the reaction to disturbances is a common approach to establish system models and to identify controllers [192].

Specifically for human locomotion, several walking experiments have been conducted that report on the immediate responses of the human spinal control to different types of unexpected disturbances including electrical stimulation [54, 231], mechanical perturbation at individual leg joints [64, 78, 232], and more natural mechanical perturbation of the whole body [221, 234]. Although external disturbances have been used in neuromechanical human walking models to either test the robustness of control models [11, 138, 240] or to study specific high-level recovery strategies [123, 181], comparisons of the reference data on the reactions of the human spinal control to the reactions predicted by the different walking models have so far not been performed.

This chapter presents how we perform the in-depth comparison of disturbance reactions for the proposed neuromechanical spinal control model of human locomotion. How the disturbance experiments are selected from the literature and replicated with the neuromechanical model are described in Section 5.1. Then, the comparison results of the disturbance reactions between the model and humans are presented in Section 5.2, and the implications of the results and future work are discussed in Section 5.3.

5.1 Disturbance Experiments on the Neuromechanical Model

We select a range of unexpected disturbances used in human gait studies from the literature, replicate them in simulation with the neuromechanical model, and compare the models reactions to the reported human experimental data.

5.1.1 Experiment Selection

Five disturbance experiments are selected from the literature: electrical stimulation of the lumbar spinal cord to evoke multisegmental monosynaptic responses (MMR) [54], mechanical tap of tendons to induce tendon tap reflex (TR) [64, 78], actuation of the ankle joint to induce stretch reflexes (SR) [232], and tripping (TRIP) of the swing leg [221] and slipping (SLIP) of the stance
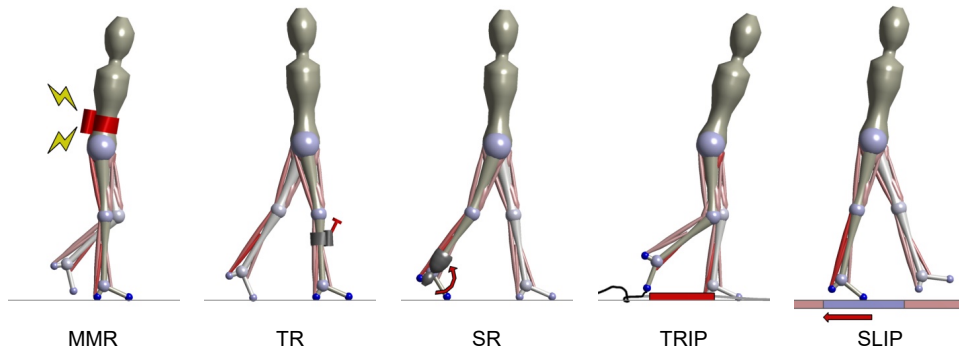
Figure 5.1: Five selected gait disturbance experiments. Details on the experiments can be found in Table 5.1.

leg [234] (Fig. 5.1). In these experiments, the reactions of the spinal control are assessed through the changes that occur in the leg muscle activations within a short time (of about 100 ms) after the disturbances. Specifically, the activation changes are measured by surface EMGs and their trend with respect to gait phase or disturbance magnitude is used to estimate the activity of spinal reflexes.

The five experiments are selected to cover a broad range of disturbances and responses. For instance, from several reports of studies using similar types of disturbances, the ones that include the EMG changes for more leg muscles and across more conditions are selected. Specifically, while both MMR [54] and H-reflex [37, 231] experiments disturb afferent signals using electrical stimulations, the former is selected since MMR disturbs multiple afferents and, as a result, induces responses in more muscles. Similarly, the SR [232], TRIP [221], SLIP [234] and TR [64, 78] experiments were chosen over similar ones that apply disturbances for fewer conditions [22, 47, 55, 76, 261, 270, 284]. (Note that the SLIP experiment by [234] reports on muscle responses with latencies of about 150 ms, which are longer than usual for spinal reflexes. Although it is acknowledged that one cannot completely exclude that these responses are long-latency reflexes, we still included the study, as the authors clarify that these apparent latencies are in part an outcome of their experimental protocol for detecting disturbances, and as we could not find an alternative study reporting responses against a range of disturbance intensities. However, to further

support our analysis on the response amplitudes in the SLIP experiment (compare Sec. 5.2.2), we have verified the consistency of our model results for a similar experiment by [22], in which the reported responses are clearly within the time window of spinal reflexes.)

5.1.2 Replication in Simulation

We adapt the original neuromechanical model [240] for each of the five experiments (Table 5.1). Since all the experiments reported on sagittal plane disturbances, the model is first reduced to its sagittal plane musculoskeletal architecture and spinal control. Then, the musculoskeletal properties are scaled [275] to match the average height and weight of the subjects in each experiment [54, 234]. If this information is not reported [64, 78, 221, 232], the height and weight are set to 1.8 m and 80 kg. Finally, the model's control parameters are optimized with the cost function

$$J = C_E + c_v \left\| v_{avg} - v_{tgt} \right\|, \tag{5.1}$$

which encourages energy efficient walking at a target walking speed. In this equation, C_E is the metabolic energy consumed by the muscles, $c_v = 100$ is a weighting factor, and v_{avg} and v_{tgt} are the average and target walking speeds (Sec. 3.6). The target walking speed, v_{tgt}, is set to the reported speed in each experiment.

The disturbances were simulated for the reported conditions in each experiment, which either included different gait phases (for MMR, TR, SR and TRIP) or different disturbance intensities (for SLIP). The mechanical disturbances of the SR, TRIP and SLIP experiments were directly replicated in the simulation by modeling an unexpected ankle flexion, the encounter of the tripping obstacle, and the shift of the supporting ground with the same parameters as reported in each experiment, respectively.

The MMR and TR experiments were less straightforward to replicate in simulation, as the neuromechanical model does not include the corresponding physiological detail. In the MMR experiment [54], muscle responses (spikes with about 20 ms durations) are induced by percutaneous electrical stimulation (1 ms square pulses) at the lumbar spinal cord, which disturbs the

78

		MMR [%]	TR [%]	SR [%]	TRIP	SLIP
height [m], weight [kg], walking speed [ms^{-1}]	exp	1.75, 64, 0.97	-, -, 0.83	-, -, 0.97	-, -, 1.11	BMI=23, 1.20
	sim		1.8, 80, 0.83	1.8, 80, 0.97	1.8, 80, 1.11	1.8, 75, 1.20
disturbance	exp	1 ms electrical square pulse percutaneously at lumbar spinal cord	tendon tap with 90 g, 1.5 ms^{-1} hammer	ankle flexion of 8° with velocity of 250°s^{-1}	2.2 kg obstacle bumped by swing leg	speed change of split-belt treadmill at 150 ms after heel strike
	sim	10 ms square pulse at afferent signals	muscle length change induced by hammer tap			
conditions	exp	16 equal phases over stride	various phases over stride	8 equal phases over stride	various phases over 5∼75% of swing	speed changes of 0.1 to 0.5 with increments of 0.1 ms^{-1}
	sim		16 equal phases over stride			

(exp: human experiment; sim: simulation replication)

Table 5.1: Experimental setup as described in the human subject studies and as replicated in simulation.

afferent pathways from the legs. Instead of modeling the electrophysiological dynamics such as the filtering effects of the skin layer, the MMR disturbance was simulated as 10 ms square pulses that were simultaneously added to the afferent signals from all muscles. The duration of 10 ms was chosen because it created similar muscle responses (spikes with about 20 ms durations) in the model. The amplitudes of the square pulses were set to be arbitrarily large (maximum isometric forces, F_m, for force afferents; optimum length, l_{ce}, for length afferents; and maximum-contraction-velocity value, $|v_{max}|$, for velocity afferents) to evoke responses much larger than the normal activations seen during walking, as reported in the MMR experiment [54].

For the TR experiment, it is generally observed that the tendon tap reflex amplitude is proportional to the tapping force [167], although the neurophysiological process behind this observation is not well understood [289]. The effect of tendon taps was modeled by simulating the length changes in the muscle tendon unit affected by the tapping. Specifically, we simulated the length change based on the tension of the muscle and the kinetic energy of the tapping hammer. As a

result, the effect of the taps on length change varied over the gait cycle according to the variation of the muscle tension.

5.1.3 Reaction Comparisons

The response trends and amplitudes were compared separately for each experiment and muscle. While the model has nine muscles per leg, data for only six muscles was available in the literature. Similarities of the response trends were quantified as the % of the model responses that lie within ± 1 standard deviation (s.d.) of human responses when linearly scaled to maximize overlap. For example, 12 out of 16 of the model's SOL responses in the MMR experiment lie within ± 1 s.d. of the corresponding human responses and thus the similarity is 12/16=75% (Fig. 5.2).

The response amplitudes are only compared for the SR, TRIP and SLIP experiments. The MMR and TR disturbances induce synchronous and artificially exaggerated muscle activation responses, which is not observed in normal voluntary activations [284]. As the model does not include these artificially synchronized muscle activations, the response amplitudes are not meaningful to compare for these studies.

5.2 Evaluation of Model Responses

5.2.1 Response Trends

The neuromechanical control model and humans react to disturbances with a similar trend for the majority of investigated muscles and experimental conditions. Figure 5.2 summarizes the changes in muscle activation organized by disturbance experiment and leg muscle. The changes observed in humans (gray lines and shaded areas indicating ± 1 s.d.) are normalized to their peak value and overlaid by the corresponding changes of the model (scaled to maximize overlap and compare trends as described in Sec. 5.1.3, black lines). While some of the response trends do not match well ($\leq 50\%$ overlap within one s.d., comparisons marked with $\ast$), for the majority of

the investigated muscles and experimental conditions the scaled model responses lie within one s.d. of the human responses (78% average overlap for unmarked comparisons).

For several of the marked comparisons, simple modifications of either the reflex control or the model tuning could improve the overlap. First, in the model, the RF is used mainly for sensing but not actuation. As a result, it cannot change activation except during swing. In the human experiments, by contrast, RF shows response trends similar to the synergistic vasti muscle group VAS throughout stride, although careful interpretation of these RF responses is needed, since surface EMGs of RF, which are used in the disturbance experiments, are prone to crosstalk from VAS [186]. If fine wire EMG of RF reveal response trends similar to those of VAS, these trends can be reproduced by modifying the model to control RF with the same reflex pathways as VAS. Such modification is tenable in the functional point of view, since RF and VAS share a common role of knee extension.

Second, the difference between human and model responses of the VAS and the GAS during late swing may be an artifact of the model tuning process, which only considered undisturbed walking. The late swing reflexes that control VAS and GAS in the model do not engage during undisturbed locomotion (Sec. 4.2.2), and thus the optimization process sets their parameters to arbitrary values as far as they do not affect normal walking. In other words, these control parameters could be further tuned to improve the overlap with human responses for the two muscles without changing the undisturbed walking behavior.

Finally, the weak overlap for the SOL in the late swing phase of the SR experiment may be the result of natural variability in humans. It is known from human experiments using the H-reflex, the electrically elicited equivalent of the stretch reflex, that the swing phase responses in SOL vary among subjects between no responses (similar to the trend predicted by the model) and the responses shown in the SR experiment [231].

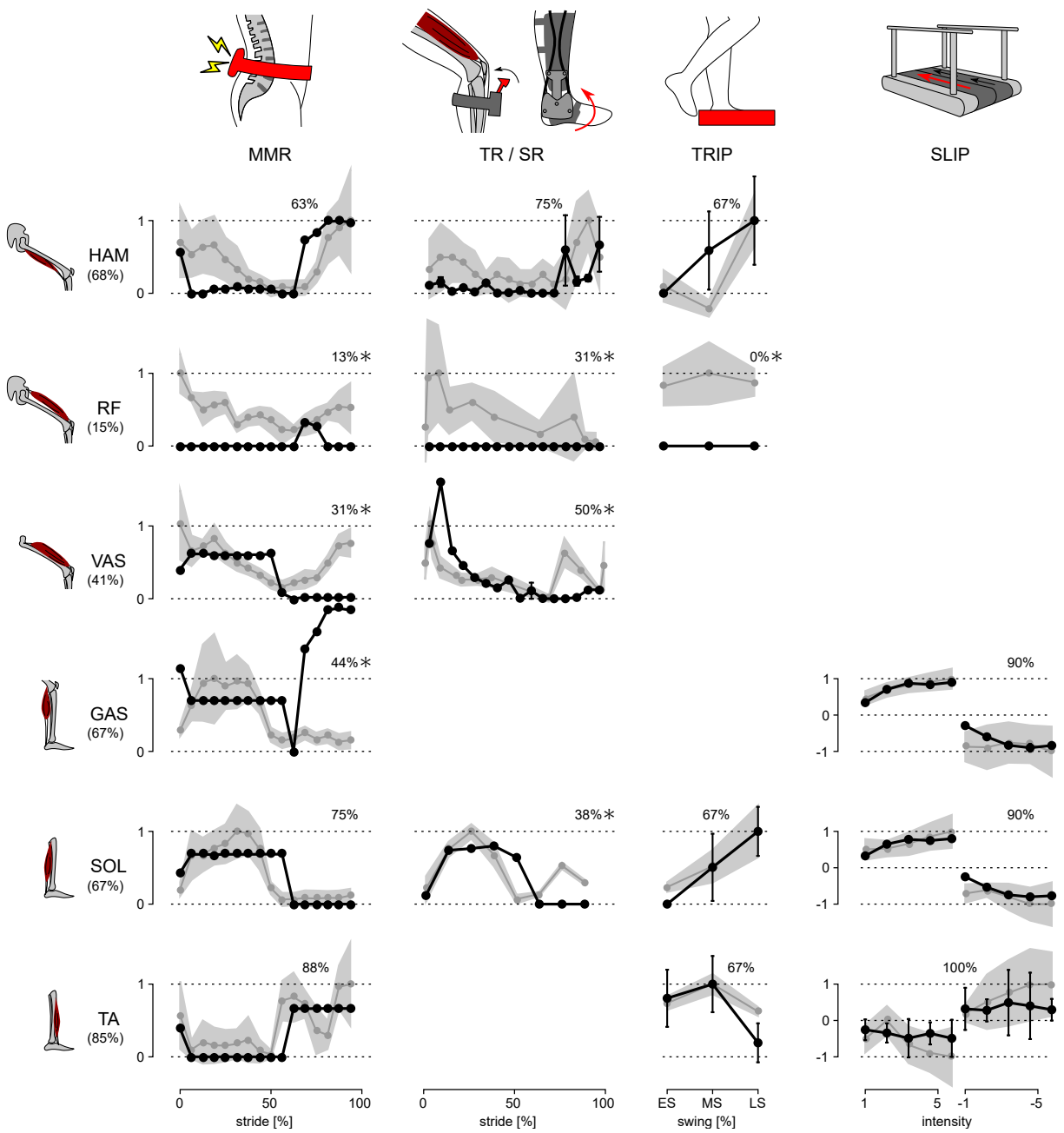**Figure 5.2:** Response trends. The responses of the model and human subjects in all five disturbance experiments are shown. Human responses (gray lines) are normalized with respect to their maximum value in each experiment and for each muscle. The model responses (black lines) are linearly scaled to place as many of the responses as possible within ±1 standard deviation of the human responses (gray shaded area).

5.2.2   Response Amplitudes

Whereas the model captures the majority of the human response trends, it clearly underestimates the response amplitudes for the more natural, whole body disturbances. In the SR experiments, the model reacts with amplitudes in the muscle activation changes that are similar to the ones reported for humans (about 90% of human amplitudes). Yet in the more natural TRIP and SLIP experiments, the response amplitudes are very small in the model (about 20% and 4%, respectively, and 8% for the experiment in [22] as noted in Sec. 5.1.1). The difference occurs as the reflexes of the model only respond to changes in the muscle lengths, velocities and forces, and the SR disturbance induces much larger changes (up to about 100 times) in these proprioceptive signals than the TRIP and SLIP disturbances, which act on the muscles through the entire body and its mechanical inertia.

One explanation for the shortfall in the model's response amplitudes could be the missing integration of reflex pathways from skin receptors. Experimental studies have shown that cutaneous reflexes evoke muscle responses with different trends across the gait cycle depending on the location of the skin receptors [69, 183, 269]. Additional modulation of the model's current proprioceptive reflexes by location-specific cutaneous reflexes (Fig. 5.3), which have been observed in cat experiments [155], could produce human-like muscle response amplitudes in all experiments without altering the response trends. Such additional modulation against specific disturbances, such as those in SLIP and TRIP experiments, is also in agreement with previous observations that cutaneous stimulations are not accountable for the responses against certain joint specific disturbances (for example, in SR experiment) [93] but do evoke muscle responses during human walking [183]. However, the functional relevance of this amplification remains open for speculation. For instance, it could promote the recovery strategies seen during human tripping (elevating and lowering strategies in early and late swing) [76] and slipping (ankle and hip strategies for anterior-posterior and medial-lateral perturbations) [195].

5.3   Implications and Future Work

The spinal-reflex-based neuromechanical model of human locomotion presented in Chapter 4 has been evaluated by comparing its reactions to disturbances with those of humans during walking. The comparison of the response trends reinforces the plausibility of the majority of the model's reflex circuits. However, the observation of smaller response amplitudes of the model for the whole body disturbances suggests that these circuits are selectively amplified in humans.

An extension of the current control model with additional circuits that modulate the current reflex gains would likely be able to better reproduce both the human response trends and amplitudes (Fig. 5.4-A). For example, instead of the abrupt switches in the reflex gains in the current model, either the supraspinal control [126, 240] or CPGs can gradually change these reflex gains (Fig. 5.4-A-a and b) and shape the response trends closer to humans (for example, during the transitions between stance and swing phases in VAS, GAS and SOL, Fig. 5.2). In addition, selective amplifications of response amplitudes for particular disturbances can be realized through additional reflex pathways that modulate the reflex gains based on the detection of those particular disturbances (Fig. 5.4-A-c). These additional reflex gain modulations would be able to
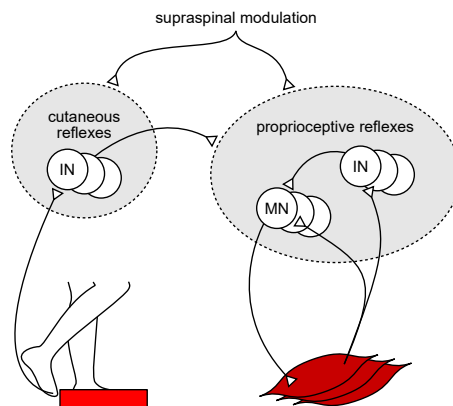

Figure 5.3: Example of proposed cutaneous amplification of proprioceptive reflex control during tripping. Location specific skin sensors at the foot detect an obstacle encounter. Cutaneous reflex pathways return this information to the spinal cord and amplify the proprioceptive reflex control of locomotion.

reproduce the human control during steady walking as well as its reactions against unexpected disturbances.

On the other hand, it remains open whether other types of models, where CPGs generate motor outputs, can reproduce steady and reactive human walking behaviors with a similar level of agreement. It is often hypothesized that CPGs generate some portion or most of the normal (background) muscle activations while reflexes in parallel generate the remaining portion [66, 70, 134] (Fig. 5.4-B). However, it is less likely that the previously proposed human walking models based on this hypothesis [71, 126, 193] can explain human responses observed in the disturbance experiments, because the more of the normal activations is generated in a feed-forward manner by CPGs the smaller the response amplitudes will be, which stands in contrast to the large reactions observed in humans. For example, in a model that generates 90% of the normal activations with CPGs and the remaining 10% with the reflex pathways of the reflex-based model [71], the response trends will remain the same but the response amplitudes will only be a tenth of the reflex-based model. Alternatively, the responsive activations could also be partially generated by CPGs as they get modulated by sensory feedback (Fig. 5.4-C). For example, phase shifts in CPG activations in response to perturbations, which is called phase resetting (Fig. 5.4-C-a), have been observed in cats [52, 223] and have been proposed to increase the robustness of human walking [11, 282]. However, the responses observed in the disturbance experiments considered in this study do not seem to originate from phase resetting of CPGs since they are transient responses rather than persistent phase shifts. Finally, CPGs have also been proposed to be continuously modulated by sensory feedback in many models, where the muscle responses result from more complicated CPG dynamics [102, 162, 193, 249] (Fig. 5.4-C-b). CPGs are usually modeled to consist of mutually inhibiting neurons with internal dynamics [160], and many human walking models [102, 193, 249] incorporate continuous sensory feedback modulation of CPGs by adding afferent signals to this internal dynamics (for example, in the form of $\tau \dot{u} = -u + other\text{-}terms + feedback$, where τ is a time constant and u is the neural out-
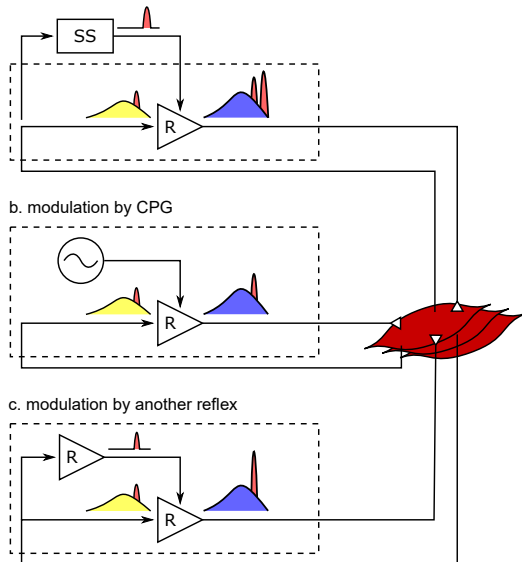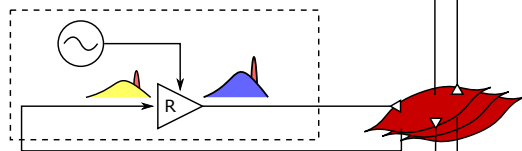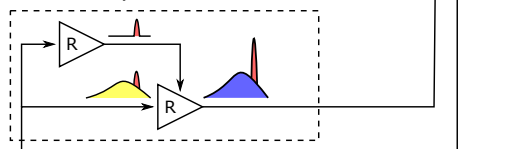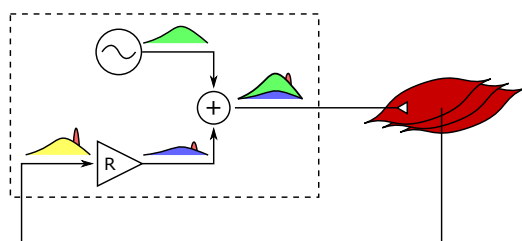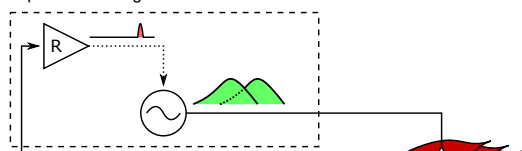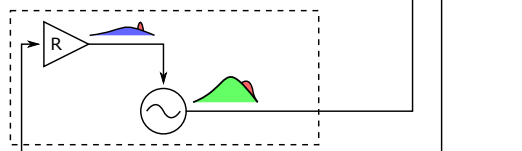
Figure 5.4: Spinal control hypotheses of the generation of muscle activations. Each block diagram represents a spinal mechanism of generating muscle activations, where the spinal control can potentially consist of serial and parallel combinations of the each mechanism. Outputs of reflex circuits and CPGs are marked in blue and green, respectively, afferent signals during normal walking are marked in yellow, and those signals in response to disturbances are marked in red. A-a. Responses through the supraspinal system appear with larger time delays than the spinal responses. This holds true for supraspinal modulations of any spinal control (not shown for B and C). A-b. Modulation of reflex circuits by pure CPGs does not change the responsive activations. A-c. Response activations of reflexes can be selectively modulated by additional reflex circuits. B. If muscle activations are generated mostly by CPGs, in other words, if the reflex circuits generate only a small portion of the activation signals, the response to the change in afferent signals would be small as well. C-a. Phase resetting of CPGs results in persistent phase shifts of the muscle activation signals. C-b. If CPGs are continuously modulated by sensory feedback, all afferent signals, including the disturbance signals, get modulated by CPG dynamics.

put). In this case, the muscle responses are likely to be slower and smaller, since the disturbance signals need to be integrated to appear in the neural outputs of the CPGs. Therefore, in order to explain both steady and reactive behaviors during human walking with control structures in which CPGs generate muscle activations, more complicated reflex circuits may be necessary that selectively amplify the responses not only for the whole body disturbances but also for the other disturbances.

Still, there is clear evidence that CPGs are highly involved in locomotion of many animals including mammals, and it is reasonable to expect human locomotion involves a similar control structure if the functional role of CPGs remained valid in the course of evolution to upright bipedal locomotion [39, 119, 156]. One functional role that has been proposed to be realized by CPGs is the generation of transitional behaviors such as changing gait, as well as locomotion speed and direction. This view is supported by observations on decerebrate animals, where simple supraspinal stimulations control locomotion by modulating the frequency and amplitude of CPGs [13, 96, 233]. It has been shown with a neuromechanical model that human locomotion speed can be controlled in a similar way by modulating CPGs of the hip muscles [265]. On the other hand, transitional behaviors including speed and directional changes also can be realized in the absence of CPGs by changing the reflex gains directly through the supraspinal control [238, 240, 241]. Therefore, the role of CPGs in transitional locomotion behaviors of humans calls for further experimental studies. To this end, investigating the responses of the hip muscles [112], which lack in previous gait disturbance experiments, can be crucial.

Our results also show that solely relying on indirect experimental observations can be misleading when assessing the role of reflexes. First, the changes in muscle responses do not necessarily indicate modulations of reflex gains. For example, in the TR experiment the changes in the model's HAM and VAS responses during stance (Fig. 5.2) result from the changes in muscle configurations while the reflex gains remain constant. Second, the correlation between the muscle states and muscle responses is not sufficient to explain the underlying muscle reflexes.

For instance, in a gait experiment similar to the SR experiment, [284] suggested velocity feedback to contribute about 45% in the generation of SOL activations during the stance phase. The suggested contribution is based on the correlation between the changes in ankle velocity and the responses in SOL activation. However, as noted by the authors of the study, this quantification neglects the potential contributions of different afferent pathways. Performing the same correlation-based analysis in our model suggests a contribution of about 40% of velocity feedback in the stance control of SOL, even though the model uses no velocity feedback but 100% force feedback.

Although the findings of our study may help to construct a model that can explain the steady and reactive spinal control of human walking, it will take further research to settle the actual circuitries in humans. First, neuromechanical simulations with more physiological details will be needed to incorporate other types of experimental studies in the evaluation of control models. For instance, we would be able to compare the response amplitudes of our control model to human responses in MMR and TR experiments if our simulations could more faithfully describe the relationship between cutaneous electrical stimulation and synchronous muscle activation as well as the related neurophysiology. Second, other models which can explain normal human walking should also be subjected to gait disturbance experiments to genuinely evaluate their plausibility and arrive at a consensus about what the human circuitry might be. Finally, the resulting control model should be verified by direct probing of the proposed neural circuits in human experiments. Although it is currently impossible to probe the entire control of humans that involves millions of neurons, a control model that is thoroughly evaluated and specified may substantially reduce the search space. Evaluation beyond steady behavior will play an important role in this quest.

Chapter 6

Applications of the Neuromechanical Model

Computational neuromechanical models can be used in various ways. Versions of the reflex-based neuromechanical model [88, 240, 243] have been applied in different studies due to their capability of generating human-like and robust locomotion; they have been adapted to test walking assistive devices in simulation [226, 251, 266], to control prosthetic legs [74, 219, 252], exoskeleton gait trainers [280], and humanoids [264], and also to generate graphical characters that walk and run like humans [87, 273]. This chapter presents three of our studies where the neuromechanical control model is used either as a simulation testbed to study human locomotion or as a robotic controller for a bipedal robot. In Sec. 6.1, the model is used as a simulation testbed to assess the influence of several components of human feet on energy consumption during walking. In Sec. 6.2, the model is used to investigate the physiological origin of the decline in elderly walking performance. Finally, in Sec. 6.3, the model is adapted to generate robust walking in a high-fidelity simulation of the bipedal robot ATRIAS.

6.1 Simulation Testbed for Studying Foot Biomechanics

Most of the material of this section has been published in:

- Song and Geyer. The energetic cost of adaptive feet in walking. *IEEE ROBIO*, 2011. [237]

- Song, LaMontagna, Collins, and Geyer. The effect of foot compliance encoded in the windlass mechanism on the energetics of human walking. *IEEE EMBC*, 2013. [244].

6.1.1 Introduction

The foot plays a special role in human locomotion. It is the segment that interacts with the environment, taking impacts, securing grip, and transmitting power. Along with this special role, the human foot has evolved, as already Leonardo da Vinci observed, into a "masterpiece of engineering" [58] that comprises about 30 segments and joints, 20 muscles-tendon units, and over 100 ligaments. Not much of the potential benefits of this rich biomechanical design [106, 224] is understood.

One of the unique features of human feet is the windlass mechanism (Fig. 6.1). The windlass mechanism engages the longitudinal foot arch and the toe segment by the PF, a thick tendon that spans from the underside of the heel to the toe [28, 250]. Previous biomechanical studies

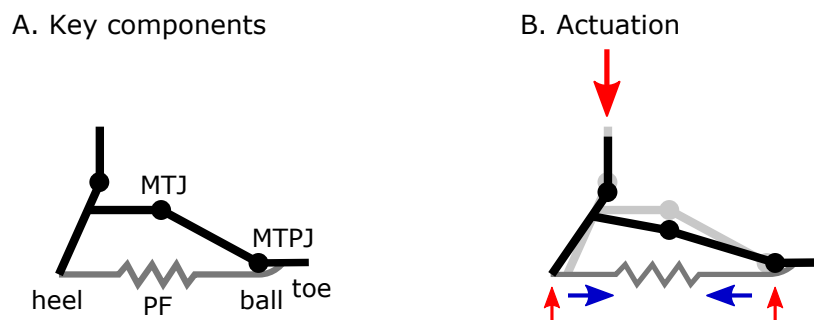**Figure 6.1:** The windlass mechanism of human feet. The key components of the windlass mechanism are the midtarsal joint (MTJ), the metatarsal phalangeal joint (MTPJ), the toe segment, and the plantar fascia (PF), which wraps around the ball and connects the heel to the toe (A). When the foot is loaded (red arrows), the windlass mechanism keeps the foot arch from collapsing by pulling the heel toward the ball (blue arrows) (B).

on the windlass mechanism focus on its functionality of passively articulating the toe segment [85, 107, 132]. Another functionality of the windlass mechanism is to modulate the stiffness of the foot depending on the load the foot is bearing. While the foot segment is flexible at normal configuration, the foot stiffens as it bears weight and the PF gets loaded (Fig. 6.1-B).

In this section, we use our neuromechanical model to investigate the energetic effect of the windlass mechanism. First, we compare the energy consumption of foot designs encoding the windlass mechanism with that of rigid feet (Sec. 6.1.2). In addition, we analyze one of the functional components of the windlass mechanism further using both simulation and human experiments (Sec. 6.1.3). We then discuss how neuromechanical simulations can compensate experimental limitations (Sec. 6.1.4).

6.1.2   Energetic Effect of Adaptive Feet in Walking

To evaluate the energetic cost during walking of the adaptive feet with an additional toe joint, we compare neuromechanical models with different foot designs (Fig. 6.2). Specifically, we adapt a sagittal plan reflex-based neuromechanical model [88] to have three different foot designs, optimize the control parameters for energy efficient walking at speeds between $0.8 \sim 1.8$ ms^{-1} (Sec. 3.6), and compare the resulting cost of transport (COT).

Rigid and adaptive foot designs

The first foot model, which serves as a baseline model when computing the energetic cost of walking, represents the entire foot, including the toe, as a rigid segment (Fig. 6.2-A). It is similar to but 5 cm longer than the one representing from the heel to the ball in Section 3.2.1 (Table 3.1). The second and third designs implement a foot that can flex the arch and adds the windlass mechanism. The flexible foot arch is realized by a spring loaded MTJ ($k_{MTJ} = 0.8$ kNm rad^{-1}). The windlass mechanism combines the flexible arch with the PF ($k_{PF} = 5 \cdot 1000$ kNm^{-2}, $l_{slack} = 16$ cm), a tendon spanning from the heel around the MTPJ to the toe segment [29, 41, 77, 107].
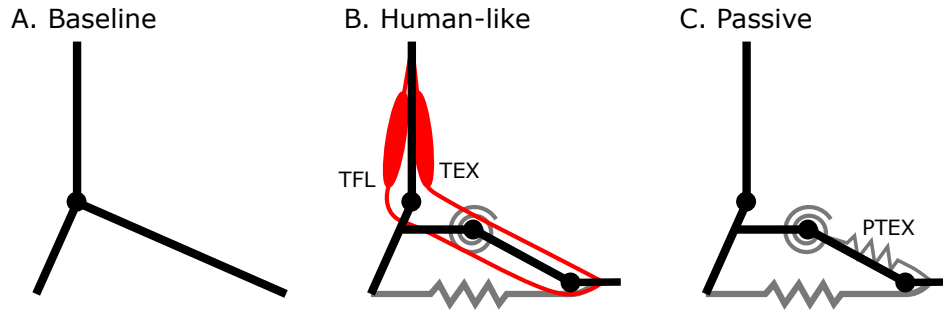
Figure 6.2: Biomechanical foot models. The rigid foot is used as a baseline model for energetic cost comparisons (A). The human-like adaptive foot model includes the windlass mechanism and the toe extension and flexion muscles (B). The passive foot model combines the windlass mechanism and a passive toe extensor spring (C).

	Baseline	**Human & Passive**		
	foot	rearfoot	midfoot	toe
l_{Sx}, l_{Sy} [cm]	25, 0	4, 8	16, 8	5, 0
$d_{G,Sx}, d_{G,Sy}$ [cm]	19, 7	3, 6	15, 7	3, 0
m_S [kg]	1.25	0.35	0.8	0.1
Θ_S [kgm^2]	0.0045	0.0001	0.0007	0.0001

Table 6.1: Mechanical parameters of the three different foot designs (baseline, human and passive).

When the foot rolls over the toe at push-off, the PF tensions and pulls the ball about the MTJ toward the heel, stiffening the foot arch for effective power transfer [27, 57]. On the other hand, the PF also tensions when the body weight loads the foot in stance and the ball and heel get pushed apart, passively exerting toe flexion torque changing the center of pressure. Note that PF stretch is substantial in human walking where it reaches one to two centimeters [29, 107]. All three foot designs share the same overall length (unloaded PF for the adaptive feet) and moment of inertia with respect to the ankle (Table 6.1).

The second and third designs differ in the way the toe joint is actuated. It is implemented in the second, human-like, design by two muscles that originate from the shank (Fig. 6.2-B). Although human feet are actuated by intrinsic foot muscles as well, we neglect these smaller muscles and focus on the large multiarticular toe flexor group (TFL) ($\{F_{max}, v_{max}, l_{opt}, l_{slack}$

| | Human | | | | | | | | | Passive |
| | ankle | | MTJ | | | | MTPJ | | | MTPJ |
	TEX	TFL	TA	TEX	TFL	PF	TEX	TFL	PF	PTEX
r_0 [cm]	4	2	1	1	6	6	1	1	1	1
φ_{max} [deg]	80	110	-	-	-	-	-	-	-	-
φ_{ref} [deg]	90	90	0	0	0	0	20	-10	0	50
ρ	0.7	0.7	0.7	0.7	0.7	0.7	0.7	0.7	1	0.7

Table 6.2: Musculoskeletal attachment parameters of the foot models, which are the moment arm r_0, maximum and reference angle, φ_{max} and φ_{ref}, and scaling factor ρ. Note that the attachments are defined as in [88] which is slightly different from those defined in Sec. 3.2.3.

$\} = \{900$ N, 12 $l_{opt}\text{s}^{-1}$, 4 cm, 9 cm$\}$) and toe extensor group (TEX) ($\{F_{max}, v_{max}, l_{opt}, l_{slack}$ $\} = \{500$ N, 12 $l_{opt}\text{s}^{-1}$, 8 cm, 22 cm$\}$). TFL and TEX originate from the shank and span via long tendons the ankle, MTJ and MTPJ, before inserting in the toe (see Table 6.2 for muscle-skeleton link parameters). The control of these two actuators mirrors the control of SOL and TA (Sec. 4.1.1). The third design, in contrast to the second model as well as to human feet, does not have muscle actuation (Fig. 6.2-C). It relies on passive springs, the PF and a passive toe extensor spring (PTEX) (k_{PTEX} =100 k N m^{-2}, l_{slack} =5 cm), to actuate the toe. The torque balance between PTEX and PF is tuned so that PTEX lifts the toe in swing into about 20 degree toe extension.

Simulation results and conclusions

The energy-optimized walking simulations of the three neuromechanical models with the different foot designs reveal that human-like feet incur about 20% more energetic cost than rigid ones for slow to moderate walking speeds. Figure 6.3 shows the identified minimum energetic cost at the six target speeds and compares the relative cost with the baseline model as the reference. For speeds up to a typical human walking speed of 1.4 ms^{-1}, the minimum energetic cost for the model with the human-like foot are the highest among all three models (Fig. 6.3-A). In particular,

A. Energetic costs of different feet

B. Energy change of different feet
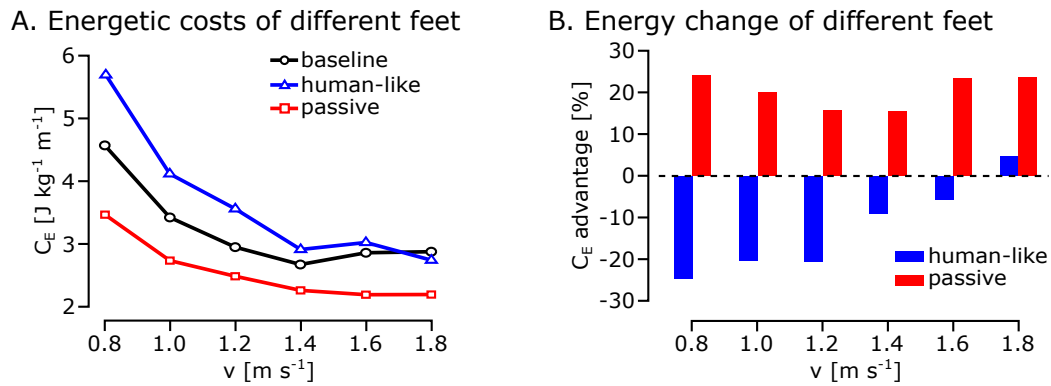
Figure 6.3: Energetic costs of walking with different feet. The energetic costs are shown for the neuromechanical walking models with the baseline, human-like and passive foot configurations (A). The energetic costs of the feet that encode the windlass mechanism (human-like and passive) are compared to that of the baseline model (B).

it is at an energetic disadvantage of about 20% relative to the baseline model with a rigid foot (Fig. 6.3-B). Although the costs are comparable between the two models at speeds larger than 1.4 ms^{-1}, the significant higher cost of human feet at slow to moderate speeds indicates that human evolution may have traded the functional advantages of adaptive feet for energy efficiency.

In contrast, the model with the passive foot design that implements some key features of adaptive feet shows significantly reduced energetic cost throughout all walking speeds. This model has the lowest absolute cost among all three models (Fig. 6.3-A), generating a relative cost advantage of at least 15% over the baseline model (Fig. 6.3-B) and of at least 20% over the human-like model.

Human-like adaptive feet provide advantages, for instance, by reducing impact and securing grip, but their need for actuation and their reduced rigidity could have a negative effect on the energy efficiency of walking. While humans seem to be willing to pay for this extra cost, the passive windlass mechanism helps to keep this extra cost minimal. Moreover, we show that the third foot design that encodes the windlass mechanism of human feet in a fully passive way can save even more energy. This third design lead us to develop a hardware foot (Fig. 6.4) that can be used for humanoids or prosthetic legs to provide passive toe actuation accordingly to the gait phase.
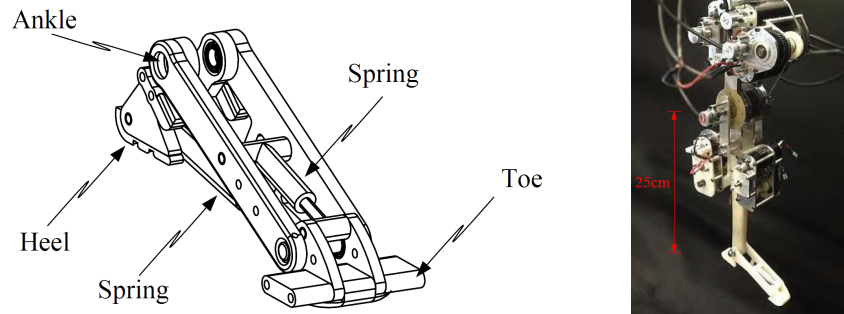
Figure 6.4: Hardware development of the foot designed based on the windlass mechanism. The design of the foot is shown on the left and the foot on a robotic leg [219] is shown on the right.

6.1.3 Energetic Effect of Foot Compliance in Walking

In the previous section, the windlass mechanism's potential of improving the energy efficiency of walking has been investigated. It has been shown that walking with feet that incorporate the windlass mechanism could save more than 15% of the energetic cost as compared to walking without the mechanism. We hypothesize that this energy saving comes either from the foot compliance introduced by the windlass mechanism or from its property of reducing the effective foot length in swing. In this section, we investigate the first option: "Do compliant feet improve the energy efficiency of walking?" To address this question, we develop a foot model, which allows to vary the stiffness of the foot independent of the foot length, and test the influence of foot stiffness on energy efficiency through simulation and experimental studies.

Simulation Setup

The simulation investigation is similar to the previous section but with a new foot design, the so-called compliant foot models (Fig 6.5). Each compliant foot model consists of two rigid segments connected to each other by the MTJ. The first segment represents the front part, from the MTJ to the ball. The second segment represents the hind part including the heel and is connected to the

95
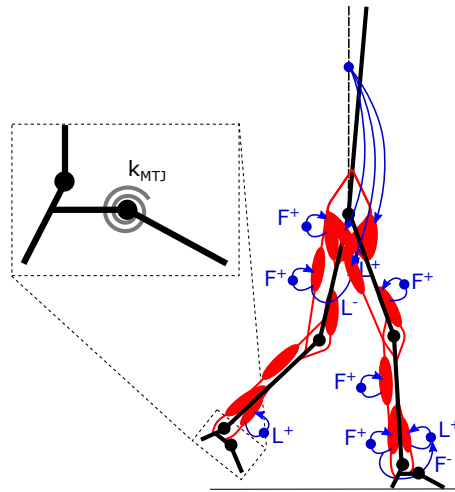
Figure 6.5: Neuromechanical model with compliant feet. The stiffness of the foot is modeled by a linear torsion spring k_{MTJ} at the MTJ. The blue lines represent the reflex pathways of the neural control (see Sec. 4.1.1 for details).

shank by the ankle joint. The MTJ is passively actuated by a linear torsion spring k_{MTJ}. In the neutral configuration, as human feet, the heel and the ball are 20 cm apart, the ankle joint is 8 cm above the sole, and each foot weighs 1.25 kg.

Energy optimal walking simulations at 1.3 ms^{-1} (Sec. 3.6) are found for a range of foot stiffness values, k_{MTJ}. The stiffness values are 250, 500, 1000, 2000, 4000, and ∞ N m rad^{-1}, where ∞ N m rad^{-1} indicates rigid feet. The minimum value 250 N m rad^{-1} is chosen to prevent the foot from collapsing during walking.

Human experiment with compliant feet

An experimental compliant shoe (Fig. 6.6-B) is developed to conduct similar experiments with real human subjects. The experimental shoe consists of a bicycle shoe and a compliant joint mechanism that attaches underneath the bicycle shoe. The bicycle shoe is stiff to isolate internal foot deformations from the compliant joint mechanism. The compliant joint mechanism includes two linear springs, where the hind spring provides comfortable heel strike. The position of the front spring can be adjusted along the fore-aft axis (Fig. 6.6-A), which changes the effective
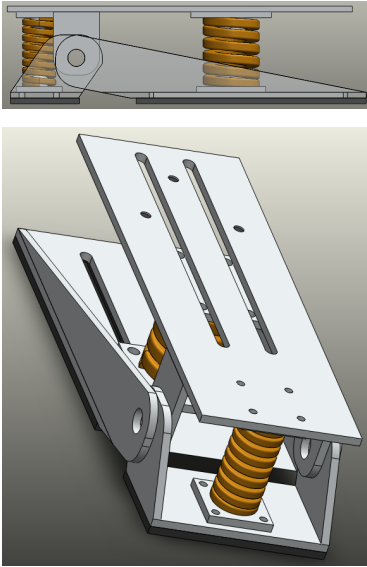
A. Compliant joint mechanism   **B. Compliant shoe**   **C. Elevated shoe**

D. Deflection of the compliant shoe while walking

$k_{MTJ} = 2200 \, \mathrm{N\,m\,rad}^{-1}$

$k_{MTJ} = 500 \, \mathrm{N\,m\,rad}^{-1}$
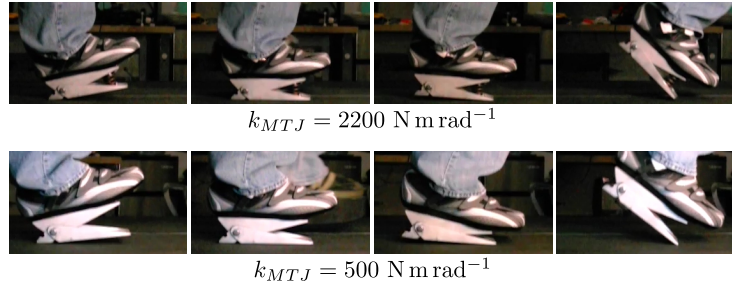
Figure 6.6: Experimental shoes. An experimental compliant shoe is developed (B), which consists of a bicycle shoe and a compliant joint mechanism (A). How the compliant mechanism deforms during walking are shown at the bottom right (D). Human subjects wear an elevated shoe on the other foot to match the height of both legs (C).
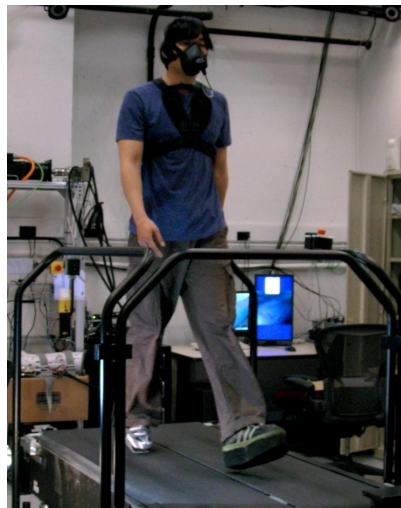
Figure 6.7: Human experiment of compliant feet. The figure shows a subject walking on a treadmill wearing the experimental shoes (the compliant shoe on the right and the elevated shoe on the left) with a respirometry system measuring the oxygen consumption and carbon dioxide production.

moment arm. By changing the moment arm of the front spring, the shoe can emulate k_{MTJ} values between 500 N m rad^{-1} and 2200 N m rad^{-1}, where large energetic differences are observed in simulation (gray region in Fig. 6.8-A). The height of the compliant joint mechanism is about 7 cm, and the entire experimental shoe weighs about 0.9 kg. To match the height of the other leg, an elevated shoe (Fig. 6.6-C) is developed which is about 0.7 kg.

The metabolic energy consumption during walking with three different foot stiffness values, $k_{MTJ} = 500$, 1300, and 2200 N m rad^{-1}, are collected from two male adult subjects (subject1: 178cm, 68kg; subject2: 182cm, 78kg). In a walking trial, a subject walked on a treadmill at a normal walking speed of 1.3 m s^{-1}, with the compliant shoe on the right and the elevated shoe on the left (Fig. 6.7). The experiments for each subject were conducted over two consecutive days, where the first day was used to ensure the subject gets familiar with the experimental set up with all the stiffness values. The metabolic costs were measured on the second day, during the last three minutes of each five-minute walking trail with different k_{MTJ} values, with ten-minute rests between the trials. The metabolic rate was estimated from the rate of oxygen consumption ($\dot{V}_{O2}$) and carbon dioxide production ($\dot{V}_{CO2}$) measured with a respirometry system (Oxycon Mobile, JAEGER [199]) as $\dot{E}$ [W] $= 16.46\dot{V}_{O2}$ [ml s^{-1}] $+ 4.48\dot{V}_{CO2}$ [ml s^{-1}] [31]. The energetic cost, or the COT, is then calculated as C_E $\left[\text{J kg}^{-1}\,\text{m}^{-1}\right] = (\dot{E}_{walk} - \dot{E}_{stand})/(m\,v)$, where $\dot{E}_{walk}$ and $\dot{E}_{stand}$ are the average metabolic rates measured during walking and quiet-standing, and m and v are the subject's mass and walking speed.

Simulation and experimental results and conclusions

The energetic costs of walking with different foot stiffness values (k_{MTJ}) for both the energy optimized model and human subjects are shown in Fig. 6.8. Results of both the simulation and the experiment suggest that walking with stiffer feet is more energy efficient than walking with softer feet. In the experiments, walking with the softest setting of the experimental shoe (500 N m rad^{-1}) incurs about 7% to 10% more energetic costs than walking with the stiffest setting
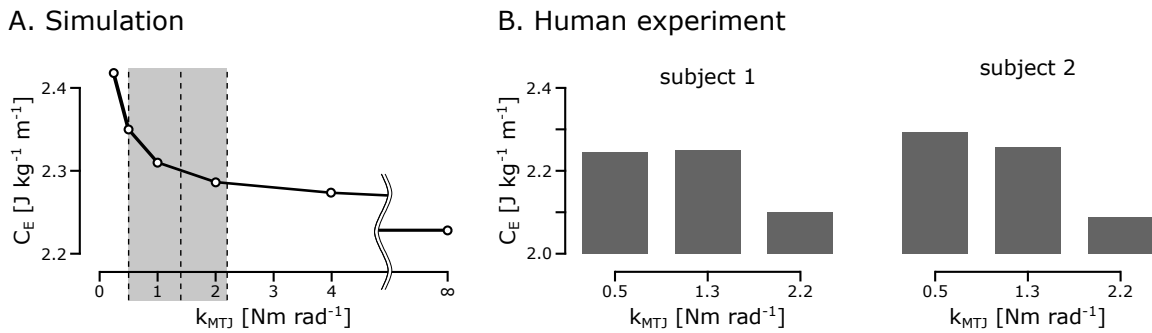
Figure 6.8: Metabolic cost of walking with different foot stiffness. The metabolic energetic cost of the energy optimal model walking with different foot stiffness, k_{MTJ} are shown on the left (A). The dotted lines indicate the k_{MTJ} values that are tested in human subjects with the experimental compliant shoe, while the gray shaded area is the range the shoe can test. The experimental results with two subjects are shown on the right (B).

($2200 \, \mathrm{N\,m\,rad^{-1}}$). The experimental results are preliminary in that the metabolic costs were measured only once at each stiffness value in a small number of subjects. More experiments are necessary to verify whether the current results generalize across more subjects.

Nevertheless, the results from the simulation and experimental studies so far suggest that the energy saved by the windlass mechanism (Sec. 6.1.2) does not originate from the compliance it embeds in the foot. The results actually indicate that stiff feet generate more energy effective locomotion than soft ones. A possible explanation for this observation is that the power transfer of the leg to the ground is more effective with stiff feet. Given our initial hypothesis that the energy saving generated by the windlass mechanism comes either from the foot compliance or from the reduction of the effective foot length in swing, the results suggest that the second option is more likely.

6.1.4   Summary and Discussion

Our simulation results suggest that the windlass mechanism reduces the energetic cost of the adaptive feet of humans during walking. Such observation lead us to a passive foot design that combines the windlass mechanism and a passive toe actuation that can save energy during walk-

99

ing, which may be an alternative for humanoid and prosthetic feet. We further investigated how the foot compliance embedded in the windlass mechanism effect the energy cost of walking. In both simulation and human experiments compliant feet worsen the energy efficiency of walking. These results suggest that the other property of the windlass mechanism of altering the effective foot length between stance and swing is the main energy saving mechanism. Moreover, the foot compliance may serve other functional purposes, such as reducing foot impact during locomotion.

The study of this section shows that neuromechanical simulations can compensate for experimental limitations. First, simulations allow modulating the variable of interest independently from other features, which may be difficult in human experiments. For example, to investigate the effect of foot compliance with real human subjects, we used a compliant shoe which introduces addition height of 7 cm to the foot which affects walking behaviors. Second, the underlying criterion of the model's walking is clearly defined by the optimization cost function. In this study, the control parameters of the model are tuned for energy efficient walking. However, although it is widely accepted that humans walk in an energy efficient way [3, 287], humans may take account of other criteria as well such as pain or muscle fatigue (Sec. 3.5). In the experimental study, one of the subjects reported moderate pain while walking with the stiffest setting. Experimental results will be distorted if the pain is large enough to cause subjects to change their walking behavior.

6.2 Simulation Testbed for Studying Elderly Walking

Most of the material of this section has been submitted to:

- Song and Geyer. Computer simulations imply strength training as the only way to enhance elderly gait. *submitted*. [236]

6.2.1 Introduction

Walking performance declines with age. In our 70-80s, compared to 20-30s, the metabolic cost of walking increases by 15-30% [158, 165], and the regular walking speed reduces by 0.2-0.6 ms^{-1} [83, 108, 149] (Fig. 6.9). At the same time, physiological properties of the neuromusculoskeletal system age as well. For example, the body's mass distribution shifts [86, 122, 202], muscles become weaker [92, 175] and slower [188, 256], and the nervous system becomes slower [30, 214] and noisier [91]. Understanding how these physiological changes relate to the decline in walking performance is essential in improving mobility, and thus, the quality of life of elderly people.

Despite many experiments, the physiological origins of the decline in elderly walking remain obscure. Previous studies have found that neither the mechanical work [165, 175, 197], nor stability measures [157, 198], nor basal metabolism [165] explains the increase in metabolic cost of walking. A change in control strategy (as hinted at by a change in muscle co-activation)
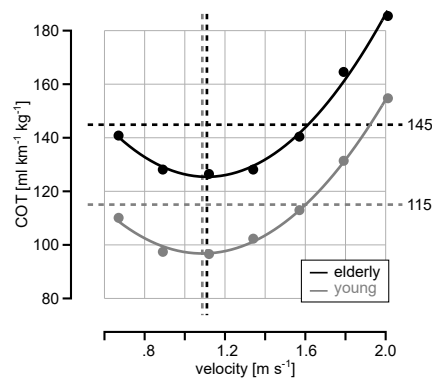
Figure 6.9: Cost of transports of young and elderly people. The data is from [158].

has been suggested to contribute to the increase in metabolic cost [114, 207] but remains debated [175]. A decline in force capacity of muscles, which requires the recruitment of less efficient fast-twitch fibers, has been proposed as one factor but not further investigated [158]. Understanding the decline in regular walking speed seems to be even more complicated since it involves the notion of preference. A common measure used to explain preferred walking speed in legged animals including humans is the metabolic energy used per walking distance, or the COT. In other words, animals prefer to walk and run at speeds at which the COT is minimal. However, the COT-speed relationship does not shift towards slower speed by much with aging (Fig. 6.9) and therefore does not explain the slower walking speeds in elderly people [157, 158, 165, 197]. The difficulty in linking the deteriorations in elderly gait to their physiological origin comes from that most of the age-related physiological changes cannot be independently controlled, nor a correlation between a gait feature and a physiological property necessarily reveals the causal relationship between those factors.

This difficulty disappears in simulation studies. In neuromechanical models of human gait, physiological changes can be independently controlled, and their effect on walking performance can be evaluated with computer simulations. So far, only a few such simulation studies have focused on age-related changes. For instance, it has been found in simulations that the ability to walk with the kinematics of young adults is fairly robust to weakening muscles, although it would increase muscle stress [263], and that weak and stiff muscles do not alter the net mechanical efficiency of the lower limb muscles in elderly gait, although individual muscle efficiencies shift [175]. However, in these previous studies, walking trajectories of young adults or elderly were imposed on the neuromechanical models, leaving it open whether the predicted effects are byproducts or indeed related to the adaptations seen in elderly gait. This ambiguity can be resolved with neuromechanical models that generate walking behavior.

In this section, we use our predictive neuromechanical model to investigate the origin of the higher metabolic energy consumption and reduced preferred walking speed in elderly peo-
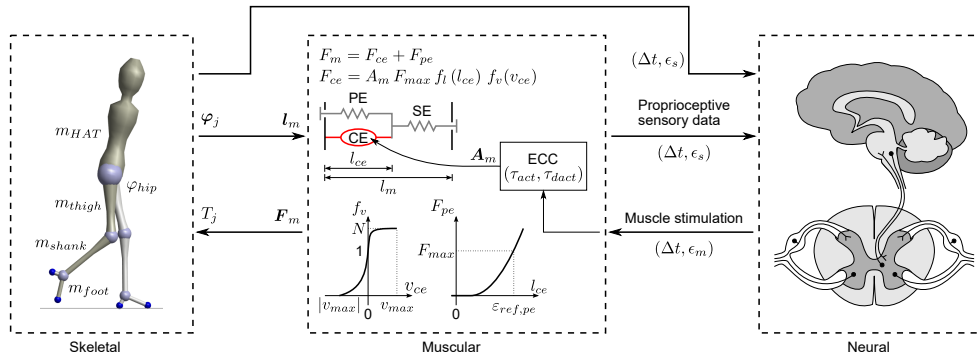
Figure 6.10: Predictive neuromechanical model of human locomotion. The model consists of skeletal, muscular and neural layers. The details of the model are in Chapter 3.

ple. We first adapt our neuromechanical model to represent healthy elderly people (Sec. 6.2.2). Then we investigate the effect of age-related physiological changes by comparing the walking simulation results of the original young model, the elderly model, and models with individual physiological changes (Sec. 6.2.3). We further discuss the implications of the simulation results (Sec. 6.2.4). This work demonstrates how predictive neuromechanical simulations can be used to study pathological gaits and their treatment.

6.2.2 Neuromechanical Model for Elderly Gait

We use our neuromechanical walking model (Fig. 6.10, Chapters 3 and 4) to investigate the origin of the higher metabolic energy consumption and reduced preferred walking speed in elderly people. Specifically, we use our model presented in the previous chapters as a baseline young model and modify it to represent healthy elderly people. The modifications mimic physiological changes that have been observed in elderlies, including the skeletal (S_1: *lighter legs and heavier trunk* and S_2: *reduced range of hip extension*), muscular (M_1: *weaker and smaller muscles* and M_2: *adjusted muscle properties including slower contraction speed*), and neural (N_1: *slower neural conductance speed* and N_2: *higher sensory and motor noise*) changes. We then optimize the control parameters for this elderly model from slow to fast walking speeds (0.8, 1.0, ..., 1.8 ms^{-1}), and analyze which of these physiological changes result in elderly-like walking behaviors.

103

This analysis includes explaining a performance criterion other than the COT, which as we have summarized before, does not indicate a slower preferred walking speed for elderly people.

The details on the age-related modifications to represent healthy adults of age around 80-year-old are summarized in Table 6.3. The modifications are categorized into six groups based on the component of the model they apply to (Fig. 6.10). In the skeletal layer, the body mass distribution changes due to loss of leg muscles and gain of body fat (S_1) [122, 202], and the range of hip extension reduces due to muscle contracture (S_2) [133, 215]. In the muscular layer, the muscles lose strength [175, 256] and mass, with much larger loss in the strength (M_1) [61, 92], and a number of muscle properties change, where the most prominent change is becoming slower (M_2) [151, 175, 188, 256]. Since not much is known about how the control changes in elderly walking, we do not change the neural control structure, but we apply neural changes of reduced neural conductance speed (N_1) [30, 214] and increased sensory and motor noise (N_2) [91]. The specific values of changes are either adopted from previous modeling studies or estimated from available human data.

physiological properties	modification from young model
S_1: body mass distribution [122, 202]	m_{leg}: -10%; $m_{HAT} = m_{total} - m_{leg}$
S_2: range of motion [215]	$\max(\varphi_{hip})$: -20%
M_1: muscle strength and mass [92, 175]	F_{max}: -30%; m_m: -10%
M_2: muscle properties [188, 256]	v_{max}: -20%; N: +30%; $\varepsilon_{ref,pe}$: -15%; τ_{dact}: +20%; p_{ft}: -10%
N_1: neural conductance speed [30, 214]	Δt: +15%
N_2: sensing and motor noise [91]	$\epsilon_s \times \epsilon_m$: +100%

m_{total}: total body mass; $m_{leg} = m_{thigh} + m_{shank} + m_{foot}$; m_m: muscle mass; p_{ft}: proportion of fast-twitch muscle fibers; other parameters are explained in Chapter 3.

Table 6.3: Skeletal, muscular and neural changes in the elderly model.

With the changes applied, the control parameters are reoptimized to minimize the criterion

$$J = \frac{1}{T} \int A_m^2 dt + (v_{avg} - v_{tgt})^2 \tag{6.1}$$

as explained in sections 3.5 and 3.6. All changes are applied together to represent elderly walking, and each change are applied individually to the baseline young model for further analysis.

6.2.3 Elderly Gait Simulation Results

The simulation results of the elderly model are consistent with the observations on elderly gait in the literature. As in young and elderly humans [176, 222], the overall walking behavior of the young and elderly models are similar in that the time-trajectories of joint angles, joint torques, ground reaction forces, and muscle activations have more or less similar shapes at all speeds. Meanwhile, some of the common features of elderly walking, such as more pelvic tilt with less hip extension throughout the gait cycle [133, 176] and smaller ankle plantarflexion torque during stance [63, 133, 175, 176] are observed in the elderly model simulation (Fig. 6.11). Most importantly, the metabolic energy consumptions of the elderly model are, in average, 16% higher than those of the young model across all walking speeds (Fig. 6.12A), suggesting the 15-30% increase observed in elderly people [158, 165] are, at least in part, captured by the modeled physiological changes. Furthermore, in agreement with human data, the walking speed of minimum COT of the elderly model is close to that of the young model.

Change in muscle strength and mass (M_1) dominantly contributes to the increased COT. When the physiological changes are applied individually to the baseline model, only M_1 results in much COT increase (16%), while the other changes do not (<5%) (Fig. 6.12B). This increase in COTs is mainly due to two factors of muscle physiology, where each factor contributes about half of the total increase (Fig. 6.13). One factor is that muscles become much weaker relative to their mass, or, in other words, the quality of muscles declines [61, 92] (Table 6.3-M_1). The total metabolic energy used for walking is the sum of the energy consumed by individual muscles,
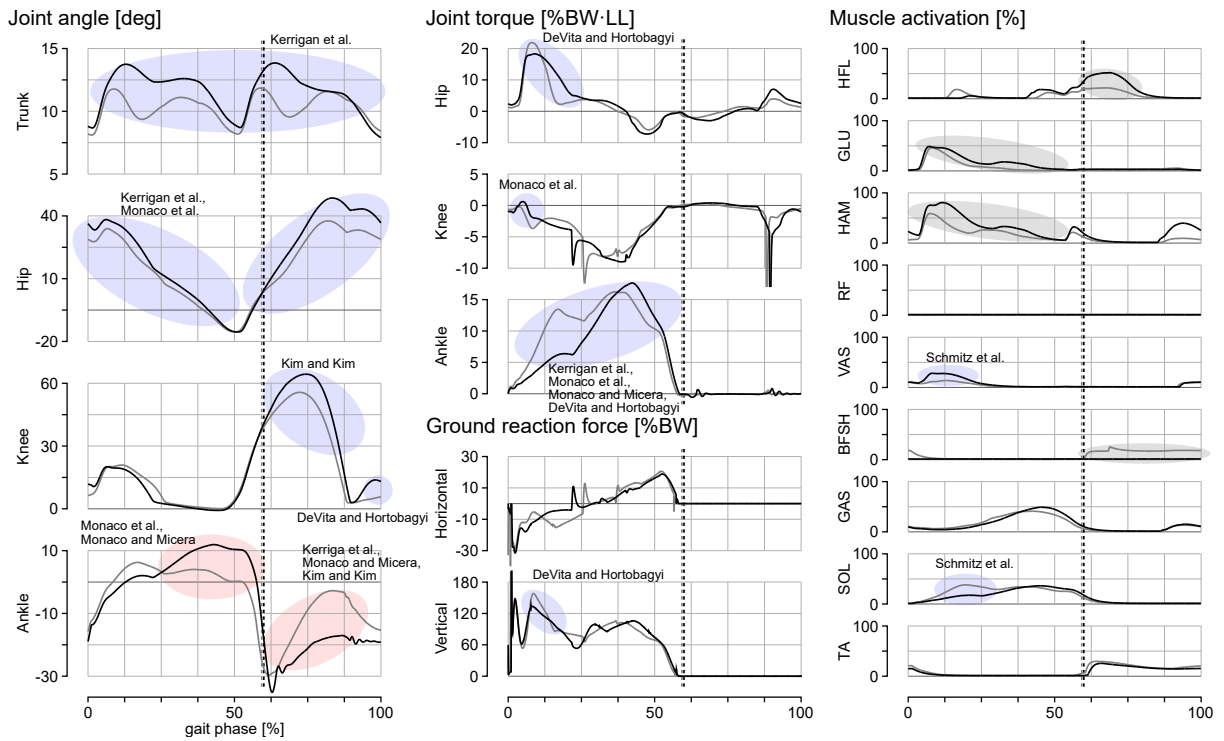
Figure 6.11: Kinematics, dynamics and muscle activations of young and elderly models walking at 1.2 ms^{-1}. The traits that are consistent across walking speeds (at least for 1.0-1.6 ms^{-1}) are marked either in blue, red or gray shades. The blue shades mark the traits that agree with reported human data, the red shades mark the ones that oppose the reported human data, and the gray shades indicate the ones that do not have enough human data to compare with. We refer to human data that allow comparisons between young and elderly walking at similar speeds, which are Kerrigan et al. [133], Monaco et al. [176], Kim and Kim [137], DeVita and Hortobagyi [63], Monaco and Micera [175], and Schmitz et al. [222]. (BW: body weight; LL: leg length)

which is calculated as $E_m = m_m(h_A + h_M + h_S + w_M)$, where m_m is muscle mass, h_A, h_M and h_S are activation, maintenance and shortening heats, and w_M is mechanical work done by the muscle [23]. Weaker muscles need to be activated more to generate enough forces, which results in higher h_A and h_M, while reduced muscle mass, m_m, results in lower energy consumption. Therefore, the muscles becoming much weaker than getting smaller results in more energy consumption. Another factor is the size-principle of motor unit recruitment. According to the size-principle, slow-twitch fibers are first recruited at low activation, and the fast-twitch fibers, which consumes more metabolic energy, are more recruited at higher activations. As this effect

is modeled in h_A and h_M, highly activated weaker muscles of the elderly model result in more energy consumption as well.

In the elderly model, the increase in energy consumption mostly happens at the hip flexors, while the ankle extensor muscles (GAS and SOL) consume even less energy than in the young model (Fig. 6.12C). This is in line with the observations that elderly people tend to use less ankle plantarflexion and more hip flexion [34, 128, 176, 222]. Among the individual changes,

Figure 6.12: Metabolic COT of walking with age-related physiological properties. A. The COTs for walking speeds between 0.8 to 1.8 ms^{-1} of the elderly model and the baseline young model are shown in black and gray, respectively (circle: simulation data; solid line: least-squares fitting quadratic polynomial; vertical dotted line: walking speed at the minimum of the fitted curve; horizontal dotted line: mean value of simulation data, where its value is shown at the right). B. The COTs with individual age-related physiological changes are shown. Applying S_2 or N_2 alone to the baseline model does not affect walking (other than numerical differences), and thus not reported. C. The COTs of the muscles that show meaningful differences in the elderly model compared to the young model are shown for all and individual age-related changes. The COTs of the other muscles in the elderly model change less than 5% of the total COT.

M_2 results in most similar adaptations, suggesting that slower muscles of elderly people are no more suitable for performing fast ankle push off and thus use more hip flexors to propel the limbs forward.

While the metabolic COT does not explain the slower preferred walking speeds observed in elderly people, we find muscle fatigue as a plausible performance criterion of selecting walking speed for both young and elderly models (Fig. 6.14). Although muscle fatigue, which is defined as an inverse of muscle endurance time, has been widely used in modeling studies to solve the muscle-joint redundancy problem [1, 169, 254], interestingly, to our knowledge, it has not been
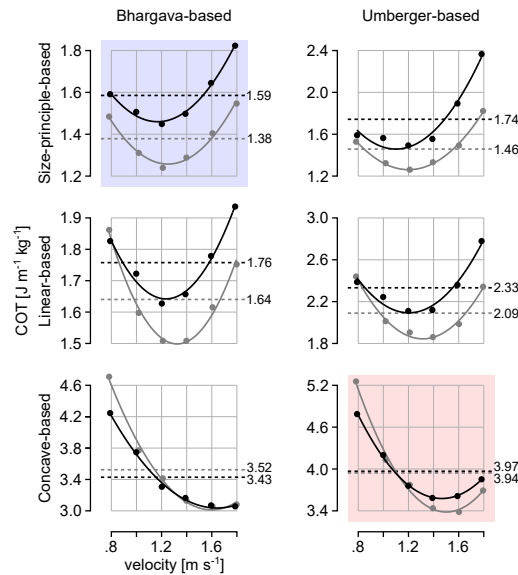
Figure 6.13: Metabolic energy calculations. The COTs are calculated based on Bhargava's [23] and Umberger's [258] muscle metabolics models. The original Bhargava's model (marked in blue shade), which is adopted in the present study (Fig. 6.12), has a convex relationship to the muscle activation based on the size-principle, whereas the original Umberger's model (marked in red shade) has a concave relationship. The activation-metabolics relationship remains debated with competing evidence [45, 118, 218]. To explore the effect of the activation-metabolics relationship, the activation terms in both models are adapted to be convex, linear or concave. It is shown that the activation-metabolics relationship can much affect the COTs in the elderly model. The Bhargava-based model with linear activation relationship (row 2, col 1) shows that the decline in muscle quality (i.e. muscle strength being larger than the reduction of muscle mass) contributes about 7% increase in COT, which is about the half of the 16% increase in the elderly model.
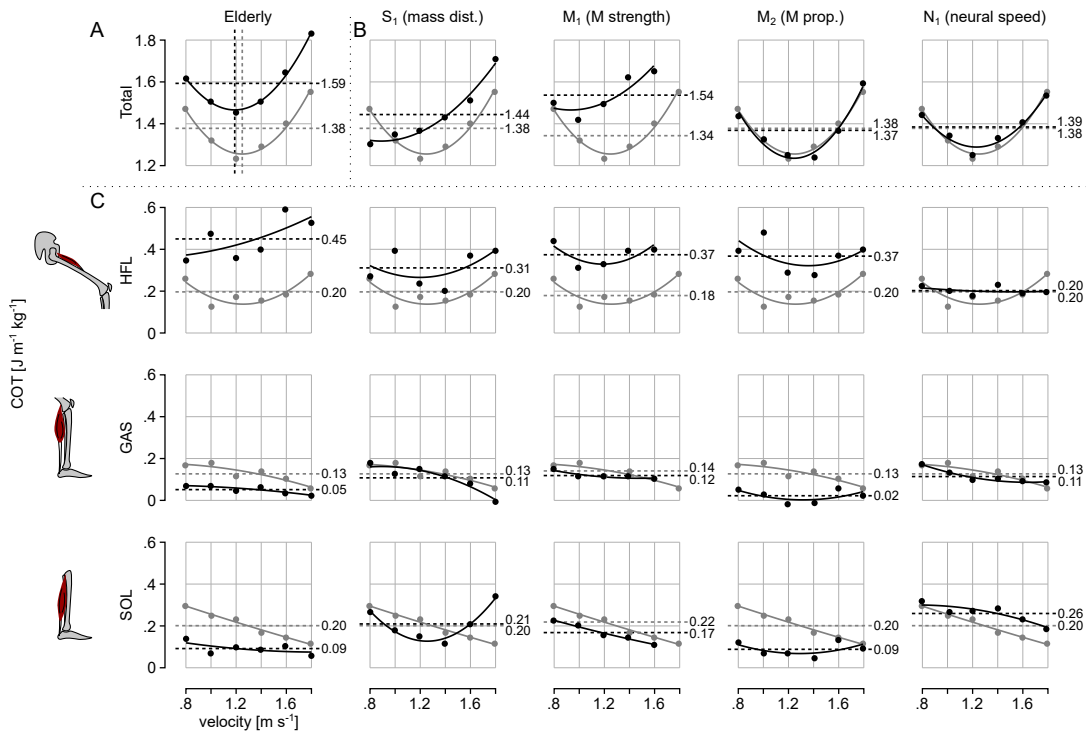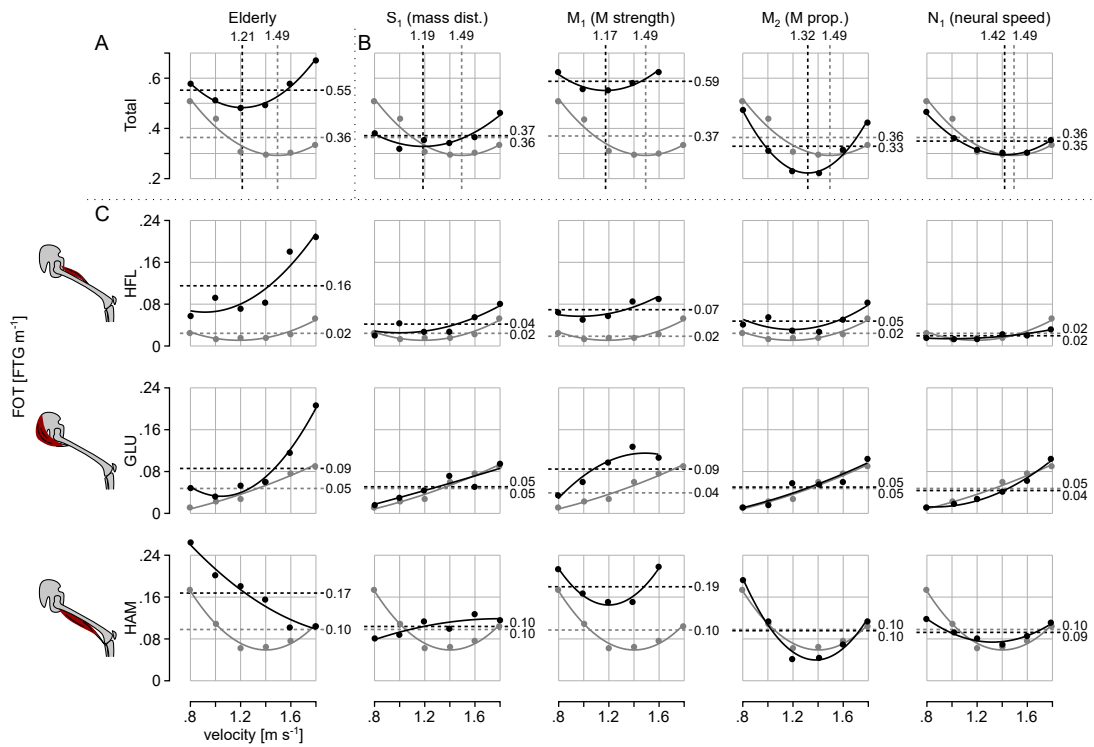
Figure 6.14: Muscle fatigue of transport (FOT) of walking with age-related physiological properties. A. The FOTs for walking speeds between 0.8 to 1.8 ms^{-1} of the elderly model and the baseline young model are shown in black and gray, respectively (circle: simulation data; solid line: least-squares fitting quadratic polynomial; vertical dotted line: walking speed at the minimum of the fitted curve, where its value is shown at the top). B. The FOT with individual age-related physiological changes are shown. C. The FOTs of the muscles that show meaningful differences in the elderly model compared to the young model are shown for all and individual age-related changes. The FOTs of the other muscles in the elderly model change less than 5% of the total FOT. (FTG: fatigue)

investigated as a criterion of selecting walking speeds. We formulate a criterion, so-called, the FOT, defined as the muscle fatigue accumulated per distance traveled, analogously to COT and find that it suggests reasonable walking speeds for both young and elderly models. Selecting a walking speed to minimize the FOT results in 1.49 and 1.21 ms^{-1} for the young and elderly model, respectively. This reduction of 0.28 ms^{-1} in elderly model is within the reported range of 0.2-0.6 ms^{-1} [83, 108, 149]. Individual changes of S_1, M_1 and M_2 all result in much reduction in preferred speed (Fig. 6.14B). (The contributions of selected muscles can be found in Fig. 6.14C.)

6.2.4 Implications of Elderly Gait Simulations

The simulation results suggest training of leg muscles may be the only effective way to enhance the walking performance in healthy elderly people. The increase of the metabolic energy demand is mostly due to muscle weakness or sarcopenia (M_1), and slower preferred walking speed is mostly due to the loss of leg muscles (M_1), which attributes to the loss of fast-twitch fibers (M_2) and results in the loss of leg mass (S_1). Therefore, recovery on other physiological changes, such as the range of joint motions, neural transmission speed and noise may not have much effect on the gait performance in healthy elderly people. It is known that physical training can recover the muscular changes and enhance walking performance in elderly people [154, 166]. However, the effects of different physical trainings vary and the optimal modes, frequency and intensity of training are unclear [154, 166]. Our results suggest to focus on recovering the strength, mass and speed of the leg muscles. For example, trainings that focus on the hypertrophy of the fast-twitch fibers [188] can be more effective than those that do not [211].

The two main factors of the elderly model consuming more metabolic energy are 1) the decline in muscle quality and 2) the recruitment of more costly fast-twitch fibers. The second factor based on the size-principle, which accounts about half of the 16% total energy increase in the elderly model (Fig. 6.13), was previously proposed by Martin et al. [158] but had not been further investigated. We speculate that one reason it had not been investigated is due to the competing evidence for the effect of the size-principle on metabolic consumption [45, 118, 218]. Moreover, there are unmodeled neural [51] and chemical [46] components between the energy consumption and force production that can change with aging. Further studies on the muscular changes in aging are necessary to clarify their effect on the metabolics of elderly walking.

Although the calculation on muscle fatigue awaits for more advancements as well (Fig. 6.15), its potential of explaining the selection of preferred walking speed can have a profound impact on gait studies. Our results show that FOT can explain the preferred walking speeds of both young and elderly people, which cannot be done with the widely accepted COT criterion. Walking at
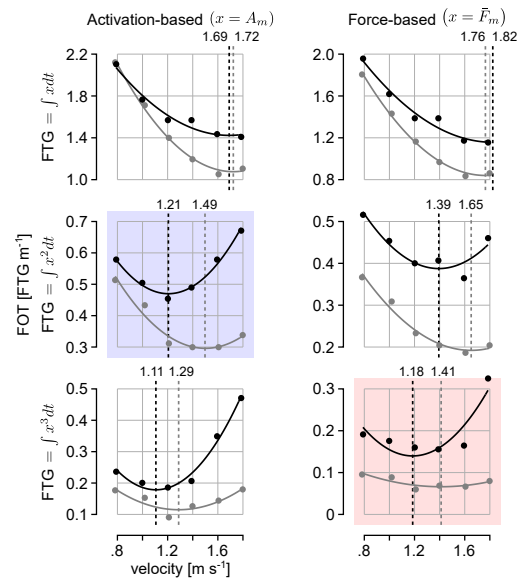
Figure 6.15: Muscle fatigue calculations. In most neuromechanical studies, muscle fatigue is calculated from either muscle activations, $\int A_m{}^p dt$, or muscle stress, $\int \bar{F}_m{}^p dt$, where $\bar{F} = \frac{F_m}{F_{max}}$. Therefore, precisely speaking, the activation and force terms represent the rate of fatigue. While the different calculations on muscle fatigue await further evaluations, most of the neuromechanical studies on human locomotion use $\int A_m{}^2 dt$ (marked in blue) [6, 169, 254], which is adopted in the present study (Fig. 6.14). For the muscle-stress-based calculations, $\int \bar{F}_m{}^3 dt$ (marked in red) is reported to well fit the stress-endurance relationship in constant force sustaining tasks in a single joint [56].

a speed of minimizing FOT rather than COT seems plausible at both the performance and the neural perspectives. It is likely that many people these days care more about muscle fatigue than shortage of energy. This is in line with the observation that fatigued elderly people do not change their walking speeds [104], suggesting that their original preferred speed is already optimal for fatigue. Moreover, muscle activations or stress, which well estimate the rate of fatigue (Fig. 6.15), may be more easily accessed by the central nervous system, especially by the portion located at the spinal cord, than the metabolic rate of individual muscles. Therefore, further investigation on FOT as a criterion for selecting locomotion speed seems promising, and elderly walking is a good task for such investigation since its speed is not explained by COT.

We have investigated the physiological origin of the deterioration in elderly walking using

predictive neuromechanical simulations. The elderly neuromechanical model with skeletal, muscular and neural changes, compared to the young model, consumes 16% more metabolic energy during walking and chooses 2.8 ms^{-1} slower walking speed based on the FOT criterion. Further analysis using simulations with individual physiological changes suggests that, among the modeled age-related changes, a decline of muscle strength mostly contributes to the increase in the metabolic cost of elderly walking. In addition, we propose FOT as a performance criterion for explaining preferred walking speed in both young and elderly people, and that the change in FOT-speed relationship with aging is due to the loss of leg muscles as well as the changes in muscle properties. The results suggest that focusing on recovering these muscular changes can effectively enhance the performance of elderly walking.

6.3 Controller for Bipedal Robots

Some content of this section has been published in:

- Batts, Song, and Geyer. Toward a virtual neuromuscular control for robust walking in bipedal robots. *IEEE IROS*, 2015. [21].

6.3.1 Introduction

State of the art locomotion controllers enable bipedal robots to walk outside the laboratory environment [81, 127, 185, 260]. A typical controller takes high-level goals from a footstep planner, uses a simple dynamics model to plan the corresponding COM trajectories, and generates target joint torques of the full robot that realize these trajectories [130]. Recent implementations of this approach replan the footsteps online to react to unexpected disturbances [260], or account for the full dynamics of the robot to calculate desired joint torques [81, 142]. Other controllers employ more heuristic policies to overcome unexpected disturbances. For example, intuition based policies that adjust the step length, leg thrust, and trunk lean have demonstrated stable locomotion [185, 212]. Despite these advances, walking controllers have not yet reached the robustness of human control in locomotion, which makes it difficult to use bipedal robots in scenarios such as rescuing lives from natural and man-made disasters.

An alternative control strategy is to imitate the human control of locomotion. Although the human control is not fully understood, various neuromechanical models have been proposed to explain fundamental control mechanisms of human locomotion, and some of them have been used to control humanoid robots [105, 180, 184, 286]. In this section, we adapt our neuromechanical model (Chapter 4) to control a bipedal robot ATRIAS (Fig. 6.16). The kinematic structure, mass distribution, and actuation dynamics of ATRIAS are much different from those of humans. We show in a high-fidelity simulation platform that the robust walking of the neuromechanical model can be transferred to this bipedal robot with significantly different dynamics.
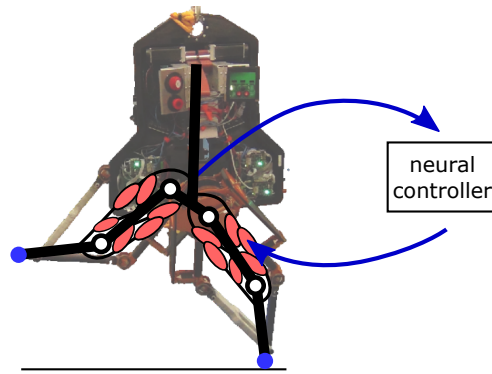
Figure 6.16: Virtual neuromuscular control for bipedal robot locomotion. The neuromuscular layer of a neuromechanical model is mapped to a robot topology (ATRIAS pictured) and emulated to generate desired motor torques.

6.3.2 ATRIAS Simulation Platform

ATRIAS is a human-size (leg length: 1 m; body weight: 63 kg) bipedal robot that is designed to concentrate the mass at the trunk [213], which results in segment dynamics different than those of humans (Table 6.4). Each of ATRIAS' legs is a lightweight four-bar linkage that makes point contact with the ground. Two series elastic actuators (SEAs) located at each hip joint drive the four-bar linkage in the sagittal plan. A third gear-motor controls the leg in the frontal plane, which can be used for 3D locomotion.

We use a high-fidelity simulation of the ATRIAS platform constrained in the sagittal plane, which is developed and tested in [159] (Fig. 6.17, Matlab Simulink/SimMechanics R2014b). The

	trunk		upper leg		lower leg		foot		
	COM to hip	mass	length	mass	length	mass	length	height	mass
ATRIAS	10	57.9	50	1.1	50	1.0	-	-	-
human model	35	53.5	46	8.5	46	3.5	20	8	1.25

(unit: cm, kg)

Table 6.4: Segment properties of ATRIAS and a human model.

ATRIAS model has 10 internal DOFs (4 for the four-bar linkages, 4 for the SEAs, and 2 for the frontal plane motors). In addition, a boom constrains ATRIAS to a circular track, while the trunk is allowed to pitch. The frontal plane motors are regulated to keep both legs in the sagittal plane. Furthermore, the simulation includes the detailed SEA dynamics and control (max torque: 350 Nm), and dynamic ground contact models (Sec. 3.4) that capture stick-slip friction. While we simulate the continuous dynamics of the physical system with a variable time-step solver (ode45, relative error tolerance: 1e-3, absolute error tolerance 1e-4), the control loop runs discretely at 1 kHz to match the control frequency of the actual robot. The simulation includes the encoders used to estimate the position and orientation of the trunk, internal joint angles, and SEA motor torques.

6.3.3 Virtual Neuromuscular Control

The virtual neuromuscular controller (VNMC) emulates a neuromechanical model to derive desired joint torques of the ATRIAS robot for walking (Fig. 6.18). The robot's trunk lean, forward velocity, joint angles and joint torques $(\theta_r, v_r, \boldsymbol{\varphi_r}, \boldsymbol{\tau_r})$ are mapped to virtual measurements re-

A. ATRIAS hardware

B. ATRIAS simulation
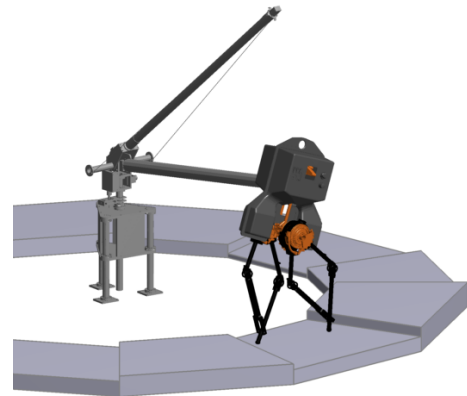
Figure 6.17: 2D experimental testbed of ATRIAS. The left picture shows the actual testbed of ATRIAS constrained to a circular track by a boom (A). We use a high-fidelity simulation of this testbed to investigate virtual neuromuscular control (B).
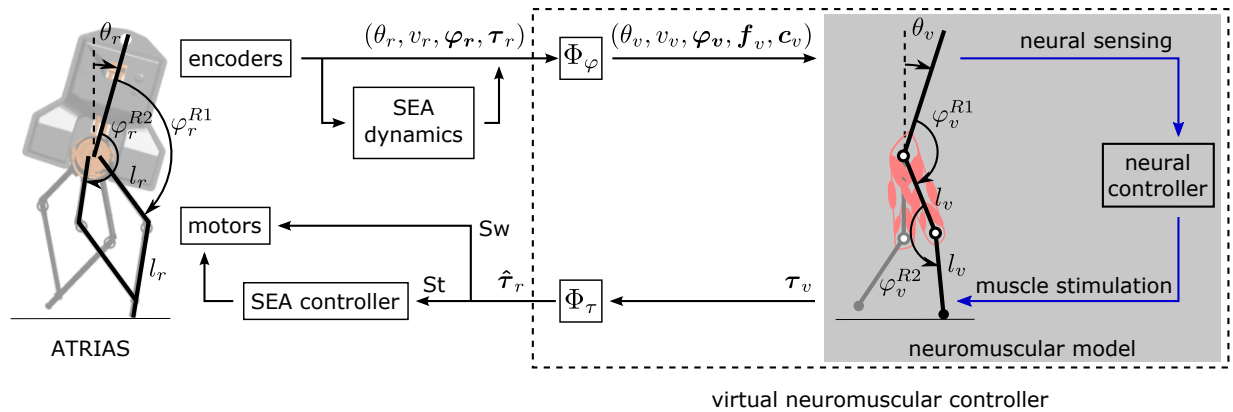
Figure 6.18: Virtual neuromuscular controller on ATRIAS. The encoders on the ATRIAS model measure the states of the robot used by the VNMC. The SEA controller tracks desired torques to drive the ATRIAS model. The desired torques are generated by the VNMC, which emulates a neuromechanical model that is mapped to the robot geometry.

quired to simulate the neuromuscular system, which are the trunk lean, forward velocity, joint angles, loading force on the legs, and the foot contact information $(\theta_v, v_v, \boldsymbol{\varphi_v}, \boldsymbol{f_v}, \boldsymbol{c}_v)$. The neuromuscular model outputs virtual joint torques $(\boldsymbol{\tau}_v)$ that are mapped to desired robot joint torques $(\hat{\boldsymbol{\tau}}_v)$. The desired joint torques $(\hat{\boldsymbol{\tau}}_v)$ are tracked by the SEA controller during stance. Because the torque measurement errors (≈ 20 Nm) and the joint frictions (≈ 20 Nm) are too large to conduct precise torque tracking of the light swing legs (≈ 2 kg), the desired torques for the motors, ignoring the SEA dynamics, are commanded directly to the motor controller during swing, relying on the fact that the spring is very stiff (≈ 3500 N m rad^{-1}) compared to the leg mass.

The neuromechanical model of the VNMC is adapted from the sagittal hip and knee components of the human neuromechanical model presented in Chapter 4. Two changes were made to the original neural controller. First, in the length and velocity feedback pathways, the joint angles and angular velocities are directly used instead of the states of the CEs in muscles. Such feedback pathways are designed to control muscles considering joint positions and velocities, and using CEs' states introduce errors since they do not capture the SEs' states (Fig. 3.4). The neural controller in Chapter 4 still uses muscle states as a biologically plausible controller, but

116

there is no reason for a robotic controller to keep these errors. In addition, using joint angles and velocities is more intuitive for one to hand tune the parameters when optimization trials get stuck in local minima misusing the control parameters [21]. Second, due to similar reasons, the unnecessary neural transmission delays are removed from the virtual neuromuscular model. Only the operation of the positive force feedback pathways utilizes the neural transmission delays in a purposeful way [89]. In other pathways, the delays only deteriorate the control. Therefore, the time delays of all data except the muscle force data are removed from the virtual neuromuscular model. The adapted model is treated as a black box controller that generates virtual joint torques based on the virtual measurements, $\boldsymbol{\tau}_v = \boldsymbol{\tau}_v\left(\theta_v, v_v, \boldsymbol{\varphi}_v, \boldsymbol{f}_v, \boldsymbol{c}_v\right)$.

The remaining part of the VNMC converts the sensory data of the robot to the virtual measurements, $\Phi_\varphi\colon (\theta_r, v_r, \boldsymbol{\varphi}_r, \boldsymbol{\tau}_r) \to (\theta_v, v_v, \boldsymbol{\varphi}_v, \boldsymbol{f}_v, \boldsymbol{c}_v)$, and the virtual torques to desired robot joint torques, $\Phi_\tau\colon \boldsymbol{\tau}_v \to \hat{\boldsymbol{\tau}}_r$. The trunk lean and the forward velocity of the virtual skeleton are identical to that of ATRIAS, $\{\theta_v, v_v\} = \{\theta_r, v_r\}$. The remaining measurements are converted through geometric transformations. The joint angles of the skeletal system, $\boldsymbol{\varphi}_v = \left(\varphi_v^{R1}, \varphi_v^{R2}, \varphi_v^{L1}, \varphi_v^{L2}\right)$, are mapped from the joint angles of the robot, $\boldsymbol{\varphi}_r = \left(\varphi_r^{R1}, \varphi_r^{R2}, \varphi_r^{L1}, \varphi_r^{L2}\right)$. For instance, the kinematic relation for the joints of the right (R) leg (while all the mappings are the same for the left leg) is

$$\varphi_v^{R1} = \frac{1}{2}\left(-\pi + \varphi_r^{R1} + \varphi_r^{R2} + \varphi_v^{R2}\right) \tag{6.2}$$

$$\varphi_v^{R2} = 2\sin^{-1}\left(\frac{l_r}{l_v}\cos\left(\frac{\varphi_r^{R2} - \varphi_r^{R1}}{2}\right)\right) \tag{6.3}$$

where l_r and l_v are the segment lengths (the thigh and shank are equal in length) of the robot and virtual legs, respectively. We model mechanical limits of ATRIAS that prevent the right hand side of Eq. (6.3) from reaching singularity. The loads on the legs, $\boldsymbol{f}_v = \left(f_v^R, f_v^L\right)$, are the components of the ground reaction forces that act in the direction from the feet to the hips. These are estimated, assuming quasi-static equilibrium, from the robot joint torques,

117

$\boldsymbol{\tau}_r = \left(\tau_r^{R1}, \tau_r^{R2}, \tau_r^{L1}, \tau_r^{L2}\right)$, as

$$f_v^R = \frac{\tau_r^{R1} - \tau_r^{R2}}{2\,l_r \sin\left(\frac{\varphi_r^{R2} - \varphi_r^{R1}}{2}\right)}. \tag{6.4}$$

The boolean vector, $\boldsymbol{c}_v = \left(c_v^R, c_v^L\right)$, indicates whether the legs are in contact with the ground. We assume a contact is made if the leg force (f_v^R or f_v^L) exceeds 25% of body-weight. Finally, the virtual joint torques, $\boldsymbol{\tau}_v = \left(\tau_v^{R1}, \tau_v^{R2}, \tau_v^{L1}, \tau_v^{L2}\right)$, are mapped to desired robot actuator torques, $\hat{\boldsymbol{\tau}}_r = \left(\hat{\tau}_r^{R1}, \hat{\tau}_r^{R2}, \hat{\tau}_r^{L1}, \hat{\tau}_r^{L2}\right)$, as

$$[\hat{\tau}_r^{R1}, \hat{\tau}_r^{R2}]^T = \Phi_\tau^T [\tau_v^{R1}, \tau_v^{R2}]^T \tag{6.5}$$

using the Jacobian

$$\Phi_\tau = \begin{bmatrix} \frac{1+k}{2} & \frac{1-k}{2} \\ k & -k \end{bmatrix} \tag{6.6}$$

between virtual and robot joint velocities with

$$k = \frac{l_r \sin\left(\frac{\varphi_r^{R2} - \varphi_r^{R1}}{2}\right)}{l_v \cos\left(\frac{\varphi_v^{R2}}{2}\right)}. \tag{6.7}$$

The virtual knee angles (φ_v^{R2} and φ_v^{L2}) are saturated at 179 deg to avoid singularity in Eq. (6.7), and the desired torques ($\hat{\boldsymbol{\tau}}_r$) are saturated at the maximum actuator torques, ± 350 Nm.

The control parameters of the black box neuromuscular model ($\mathbf{R}^n, n = 48$) are optimized to generate robust walking. Specifically, we simulate ATRIAS walking on a circular track with one-meter-long flat ground tiles of randomly varying heights and use CMA-ES ([100], Sec. 3.6) to find the largest height difference $|\Delta h_{max}|$ that ATRIAS successfully traverses. For that purpose, the cost function below is used:

$$J = \begin{cases} d_{tgt} - d_{walk}, & \text{if } d_{walk} < d_{tgt} \\ -|\Delta h_{max}|, & \text{otherwise} \end{cases}, \tag{6.8}$$

where d_{tgt} is a target travel distance ($d_{tgt} = 30$ m ≈ 2.5 laps), and d_{walk} is the distance the model walks before falling. The cost function was designed considering two possible simulation outcomes: falling and completing the course. First, if the model fails to reach the target distance

($d_{walk} < d_{tgt}$), the cost decreases the further the model walks. Second, if the model success-fully traverses the track ($d_{walk} \geq d_{tgt}$), the cost decreases as the largest ground-height change ($|\Delta h_{max}|$) increases, which is also an optimization parameter. The initial seed parameters for optimization were hand-tuned on flat terrain.

6.3.4   Simulation Results

With the optimized VNMC, ATRIAS can walk on a terrain with maximum height differences of $\pm$ 20 cm. Fig. 6.19 shows kinematic and kinetic data for 10 seconds of this walking behav-ior, during which the robot traverses the maximum height changes. The estimated foot contact information used in the control fairly agrees with the actual contacts. As the robot ascends and descends the tiles, the forward velocity (v_r) across steps does not change much, while the trunk lean (θ_r) and step length do change much. For example, when descending a -20 cm step (the third to the last step in Fig. 6.19), ATRIAS makes a long step (about 95 cm) and the trunk leans forward (about 22 deg) due to a large impact produced at foot contact. The GRFs varies much as the robot traverses the terrain. Human-like double hump vertical GRF is observed in some steps (the second and fourth right steps in Fig. 6.19); while, in some other steps, the stance foot looses contact due to excessive rebound after initial contact (the first, seventh and eighth right steps). The SEA torques match the desired torques well during stance, while they jitter around zero dur-ing swing. This is expected, since, during swing, the desired torque is commanded directly to the motor controller, and the load on the SEA is small. The jitter during swing sometimes appears in the joint angles as well.

6.3.5   Future Work

We proposed the VNMC that adapts the neuromechanical model into a walking controller for bipedal robots. In a high-fidelity simulation of the ATRIAS bipedal robot constrained to the sagittal plane, the VNMC can generate walking on rough terrain with height changes of ±20 cm
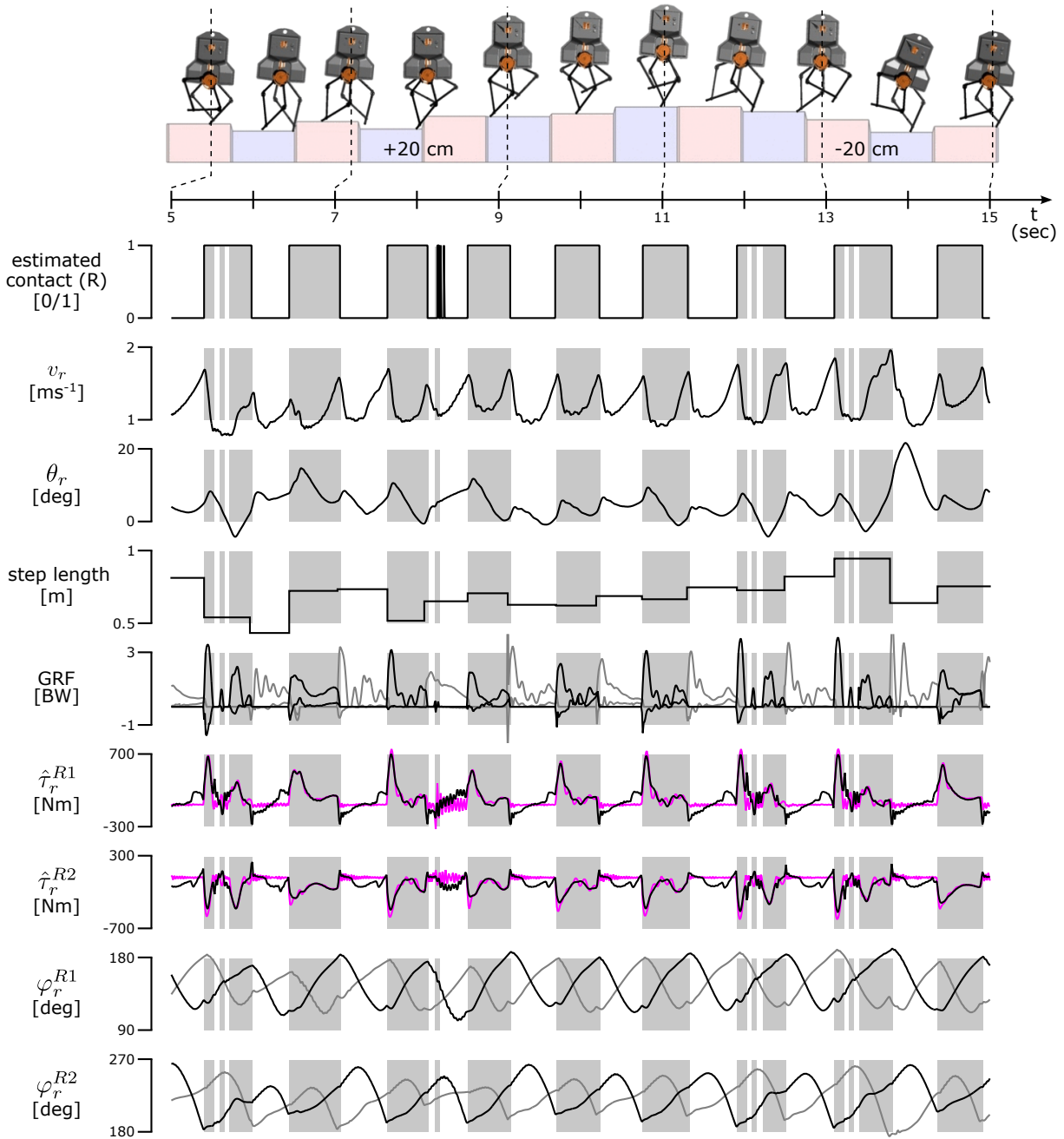
Figure 6.19: Kinematic and kinetic data while walking on rough terrain. The top panel shows snapshots projected to a 2D plane of ATRIAS every 1 sec walking on a ± 20 cm terrain. The panels below show the estimated foot contact of the right leg, forward velocity v_r, trunk lean θ_r, step length, right leg ground reaction forces (gray: left leg; scaled to body weight (BW)), right leg joint angles φ_r^{R1} and φ_r^{R2} (gray: left leg), and right leg desired joint torques $\hat{\tau}_r^{R1}$ and $\hat{\tau}_r^{R2}$ (magenta: SEA torques). The actual stance phases of the right leg, which are different from the estimated contact information, are marked by gray background.

120
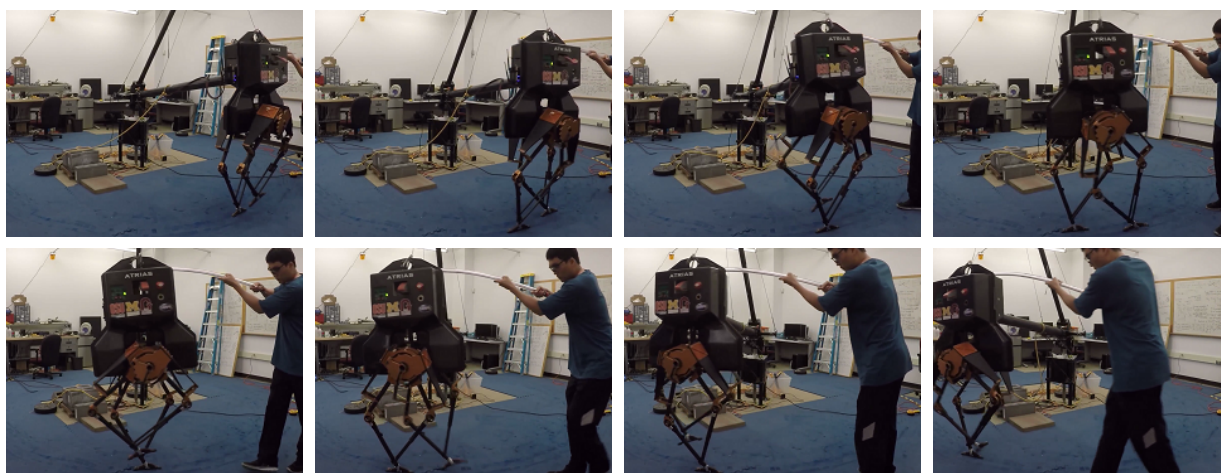
Figure 6.20: ATRIAS making walking steps. The figure shows snapshots (every 500 ms) of ATRIAS making walking steps. The stance leg is controlled by the VNMC, while the swing leg is controlled by a heuristic position-tracking controller. ATRIAS is constrained to the sagittal plane by a boom and is pushed forward by an experimenter.

without changing the control parameters.

An obvious future direction is to extend the current work for 3D walking and to verify the simulation results on the ATRIAS hardware platform. Extension of the current VNMC for straight 3D walking of ATRIAS seems to be straightforward, at least in simulation, since the original neuromechanical model generates robust 3D walking in simulation (Sec. 4.2.2, Fig. 4.5, Table 4.1), and an addition of foot segments with free ankles (i.e. little passive torque at the ankle) has been enough to prevent slipping around the vertical axis in previous walking studies with the ATRIAS hardware [115]. Regarding transferring to hardware, we have done some preliminary work on testing the stance leg control. With hand-selected control parameters, the stance leg control is able to generate stable standing (with the legs splayed, and on the boom) and generate stance leg behavior for sagittal plane walking. For example, with a heuristic position-tracking swing leg controller, the VNMC generates reliable stance leg behavior while ATRIAS makes forward steps by external pushes (Fig. 6.20).

To be useful as a robotic controller, the controller should be able to initiate and terminate

121

walking from and to standing which is lacking in the current VNMC. In the presented simulation study, ATRIAS starts with initial forward velocity and in an appropriately pose for walking, which is difficult to reliably reproduce in hardware. A simple solution, which we have validated in simulation, is to adapt an existing robotic controller [129, 210, 212] for walking initiation then to switch to the VNMC. The proper control parameters of the VNMC, of which basin of attraction covers the walking state of the adapted walking initiation controller, can be found by off-line optimization. An ultimate solution is to extend the original neuromechanical control model to include walking initiation and termination. Once such extension is made in the neuromechanical model in the proposed hierarchical structure (Sec. 4.4), the resulting VNMC would be able to make transitions between standing and walking and even running with simple high-level commands.

Another challenge that emerges in the process of transferring from simulation to hardware is the difficulties in tuning the control parameters. Although we use a high-fidelity simulation that includes some details of motor dynamics and joint frictions, it is not perfect and thus introduces simulation bias. Therefore, the control parameters, which counts about 50, optimized in simulation may not successfully work in hardware, and it is difficult, if not impossible, to run hundreds of trials with the hardware robot to re-optimize the parameters as done in simulation. Basically, there are two ways to overcome this issue. First, one can improve the simulation environment to overcome the model uncertainty. For example, control parameters can be learned in an ensemble of simulations that covers the potential model uncertainty [179], or both the model and the control parameters can be learned iteratively from the differences between the simulated behaviors and those in the hardware experiments [98]. Second, one can use more sample efficient optimization methods that are applicable on hardware. Bayesian optimization with domain specific kernels [7] and preference-based Bayesian optimization [253] have been explored to sample-efficiently tune (although fewer in number) the control parameters of the neuromechanical model ($n = 16$) or the VNMC for a prosthetic leg ($n = 3$), respectively. We suggest to combine both approaches

for setting the control parameters of VNMC for bipedal robots: first, find a set of control parameters using advanced simulation techniques that is good enough to generate stable walking on hardware, and then further tune the parameters on hardware using sample-efficient optimization techniques.

Chapter 7

Conclusions

This thesis proposes a neuromechanical control model that can explain diverse human loco-motion behaviors, evaluates the plausibility of the proposed model using a range of unexpected disturbances, and demonstrate how the model can be adapted to a simulation testbed for studying humans and to a robotic controller for leg machines. The details of the work, their implications to the state of the art, and suggestions for future research are summarized below.

- **Chapter 4: We propose a spinal-reflex-based control model that can generate diverse human locomotion behaviors.**

  - When optimized for energy efficient walking, the model generates kinematics, dy-namics, and muscle activations close to those observed in normal human walking. Only a few previous models generate such human-like walking.

  - The behaviors the model can generate include walking and running, acceleration and deceleration, slope and stair negotiation, turning, and deliberate obstacle avoidance. To our knowledge, no previous model has demonstrated such diverse behaviors.

  - The work demonstrates that CPGs are not necessary for generating human locomo-tion behaviors, which opposes a common view on human locomotion control.

  - The work supports the possibility that a range of human locomotion behaviors may

be generated by a unified spinal controller. The higher-layer brain control may be modulating the unified spinal controller to change locomotion behaviors, instead of switching between multiple controllers.

- For experimental neuroscientists, the model can serve as a guide for searching the neurophysiological origin and circuitry of spinal control in humans. Since each neural circuit of the model embeds a specific function, verifying the circuits in humans can lead to function-oriented rehabilitation treatment.

- Potential future research: The proposed neuromechanical model is incomplete in that only part of the control is in a hierarchical structure. Hierarchizing the full control and developing a higher layer control that can modulate the lower layer control based on high-level locomotion tasks and environmental cues are left as future work, where reinforcement and supervised learning techniques may be effectively used.

- **Chapter 5: We evaluate the plausibility of the proposed control model using a range of unexpected disturbances.**

  - To our knowledge, this is the first work of evaluating a neuromechanical model by comparing its muscle responses to those observed in humans. We show that how the similarities between the model's and humans' responses reinforce the plausibility of the model, and how the differences reveal the shortage of the model providing a better idea about human control.

  - The role of CPGs in human locomotion control remains questionable. Incorporating CPGs into the proposed reflex-based controller to generate some portion of muscle activations is likely to change the response amplitudes to become farther from what is observed in humans.

  - Potential future research: Mutual influences between developing control models and designing human experiments will facilitate our understanding of human control.

Control models should explain more experimental observations, and human experiments should be designed to differentiate more control models. In this iterative process, neuromechanical simulations should include more physiological details, and more existing control models should be evaluated by comparing its behaviors with human experiments.

- **Chapter 6: We show how the proposed neuromechanical model can be used as a simulation testbed for studying human locomotion and as a robotic controller for legged machines.**

  - The model is used to study human foot biomechanics by simulating walking with different foot designs. The simulation results suggest that adaptive feet with additional toe joint costs more energy, the windlass mechanism in human feet partially saves this cost, and this saving does not come from the compliance of the feet which is also supported by real human experiments.

  - The model is used to study the physiological basis of the decline of walking performance in elderly people. The simulation results suggest that the increase in metabolic cost and reduction in regular walking speed in elderly people is attributed to the loss of leg muscles as well as the changes in muscle properties. In addition, we propose muscle fatigue as a plausible performance criterion for selecting walking speed in both young and elderly people.

  - Potential future research for better simulation testbeds: The ultimate simulation testbed for human locomotion, which I call the *digital locomotor clones*, should be able to predict locomotion behaviors and their adaptations to internal (ex. injury and surgery) and external (ex. assistive devices and external disturbances) changes of any individual, from young to old and from healthy to ill. Toward this goal, much work should be done to 1) increase modeling details of the neuromechanical simulation environment (ex. physiological details and interaction with assistive devices), 2) model the

127

physiological features of different ages and pathologies, and 3) customize simulation models to individual human subjects.

- We propose a framework for adapting a neuromechanical control model to a robotic controller. The framework, which we call the virtual neuromuscular controller, is tested on a bipedal robot ATRIAS. With the controller, ATRIAS could generate robust walking in physics simulation. Our work is novel in that we replaced unnecessary biological components with robotics ones (ex. removal of unnecessary neural delays, replacement of biological sensory data with joint encoder data, etc.) reasoning about their functional necessity.

- Potential future research for better robotic controllers: The neuromechanical control model can be further adapted into a robotic controller. In other words, the functional principles encoded in the neuromechanical model can be interpreted directly for a specific robot, based on its kinematic structure and its motor dynamics, and emulating virtual muscles would not be necessary.

Human control of locomotion has been investigated for the past century but still remains a grand challenge. This thesis shows that neuromechanical simulations may play an essential role in advancing our knowledge of human control. As the neuronal-to-circuitry layer is better understood by neuroscientists and the circuitry-to-behavior layer is better explained by neuromechanical simulation models, we will eventually come to fully understand the human locomotion control. This understanding will change the way we design rehabilitation treatment and engineer assistive devices.

Bibliography

[1] Marko Ackermann and Antonie J van den Bogert. Optimality principles for model-based prediction of human gait. *Journal of biomechanics*, 43(6):1055–1060, 2010. 3.5, 4.2.1, 6.2.3

[2] R McN Alexander. Three uses for springs in legged locomotion. *The International Journal of Robotics Research*, 9(2):53–61, 1990. 2.2.1

[3] R McNeill Alexander. Energetics and optimization of human walking and running: the 2000 raymond pearl memorial lecture. *American Journal of Human Biology*, 14(5):641–648, 2002. 1.2, 2.2.1, 6.1.4

[4] Jessica L Allen and Richard R Neptune. Three-dimensional modular control of human walking. *Journal of biomechanics*, 45(12): 2157–2163, 2012. 2.3

[5] Frank C Anderson and Marcus G Pandy. Dynamic optimization of human walking. *Journal of biomechanical engineering*, 123(5): 381–390, 2001. 2.3

[6] Frank C Anderson and Marcus G Pandy. Static and dynamic optimization solutions for gait are practically equivalent. *Journal of biomechanics*, 34(2):153–161, 2001. 3.5, 3.5, 6.15

[7] Rika Antonova, Akshara Rai, and Christopher G Atkeson. Sample efficient optimization for learning controllers for bipedal locomotion. In *Humanoid Robots (Humanoids), 2016 IEEE-RAS 16th International Conference on*, pages 22–28. IEEE, 2016. 6.3.5

[8] Shinya Aoi and Tetsuro Funato. Neuromusculoskeletal models based on the muscle synergy hypothesis for the investigation of adaptive motor control in locomotion via sensory-motor coordination. *Neuroscience research*, 104:88–95, 2016. 2.2

[9] Shinya Aoi and Kazuo Tsuchiya. Generation of bipedal walking through interactions among the robot dynamics, the oscillator dynamics, and the environment: Stability characteristics of a five-link planar biped robot. *Autonomous Robots*, 30(2):123–141, 2011. 2.2

[10] Shinya Aoi, Naomichi Ogihara, Yasuhiro Sugimoto, and Kazuo Tsuchiya. Simulating adaptive human bipedal locomotion based on phase resetting using foot-contact information. *Advanced Robotics*, 22(15):1697–1713, 2008. 2.2, 2.3, 2.3.1, 2.3.2

[11] Shinya Aoi, Naomichi Ogihara, Tetsuro Funato, Yasuhiro Sugimoto, and Kazuo Tsuchiya. Evaluating functional roles of phase resetting in generation of adaptive human bipedal walking with a physiologically based model of the spinal pattern generator. *Biological cybernetics*, 102(5):373–387, 2010. 2.2, 2.3, 5, 5.3

[12] Shinya Aoi, Naomichi Ogihara, Tetsuro Funato, and Kazuo Tsuchiya. Sensory regulation of stance-to-swing transition in generation of adaptive human walking: A simulation study. *Robotics and Autonomous Systems*, 60(5):685–691, 2012. 2.2, 2.3

[13] David Malet Armstrong. The supraspinal control of mammalian locomotion. *The Journal of Physiology*, 405(1):1–37, 1988. 2.1.2, 5.3

[14] Edith M Arnold, Samuel R Ward, Richard L Lieber, and Scott L Delp. A model of the lower limb for analysis of human movement. *Annals of biomedical engineering*, 38(2):269–279, 2010. 3.2.2, 3.2.3

[15] Yu I Arshavsky, IN Beloozerova, GN Orlovsky, Yu V Panchin, and GA Pavlova. Control of locomotion in marine mollusc clione limacina i. efferent activity during actual and fictitious swimming. *Experimental brain research*, 58(2):255–262, 1985. 2.1, 2.1.1

[16] Yu I Arshavsky, IN Beloozerova, GN Orlovsky, Yu V Panchin, and GA Pavlova. Control of locomotion in marine mollusc clione limacina ii. rhythmic neurons of pedal ganglia. *Experimental brain research*, 58(2):263–272, 1985. 2.1.1, 2.3

[17] Yu I Arshavsky, GN Orlovsky, and Yu V Panchin. Control of locomotion in marine molluscclione limacina. v. photoinactivation of efferent neurons. *Experimental brain research*, 59(1):203–205, 1985. 2.1.1

[18] YuI Arshavsky, TG Deliagina, GN Orlovsky, YuV Panchin, GA Pavlova, and LB Popova. Control of locomotion in marine mollusc clione limacina. vi. activity of isolated neurons of pedal ganglia. *Experimental brain research*, 63(1):106–112, 1985. 2.1.1

[19] YUI ARSHAVSKY, TG Deliagina, and GN ORLOVSKY23. Interneurones mediating the escape reaction of the marine mollusc clione limacina. *The Journal of Experimental Biology*, 164:307–314, 1992. 2.1.1

[20] John V Basmajian. Control of individual motor units. *American Journal of Physical Medicine & Rehabilitation*, 46(1):480–486, 1967. 2.1.4

[21] Zachary Batts, Seungmoon Song, and Hartmut Geyer. Toward a virtual neuromuscular control for robust walking in bipedal robots. In *Intelligent Robots and Systems (IROS), 2015 IEEE/RSJ International Conference on*, pages 6318–6323. IEEE, 2015. 6.3, 6.3.3

[22] W Berger, V Dietz, and J Quintern. Corrective reactions to stumbling in man: neuronal co-ordination of bilateral leg muscle activity during gait. *The Journal of physiology*, 357:109, 1984. 2.2.2, 5.1.1, 5.2.2

[23] Lindsay J Bhargava, Marcus G Pandy, and Frank C Anderson. A phenomenological model for estimating metabolic energy consumption in muscle contraction. *Journal of biomechanics*, 37(1):81–88, 2004. 6.2.3, 6.13

[24] Emilio Bizzi and Vincent CK Cheung. The neural origin of muscle synergies. *Frontiers in computational neuroscience*, 7, 2013. 1.2, 2.1.4, 2.2.2

[25] Emilio Bizzi, Matthew C Tresch, Philippe Saltiel, and Andrea d'Avella. New perspectives on spinal motor systems. *Nature Reviews Neuroscience*, 1(2):101–108, 2000. 2.1.4

[26] Reinhard Blickhan. The spring-mass model for running and hopping. *Journal of biomechanics*, 22(11):1217–1227, 1989. 2.3

[27] F Bojsen-Møller. Calcaneocuboid joint and stability of the longitudinal arch of the foot at high and low gear push off. *Journal of Anatomy*, 129(Pt 1):165, 1979. 6.1.2

[28] FINN Bojsen-Moller and KE Flagstad. Plantar aponeurosis and internal architecture of the ball of the foot. *Journal of Anatomy*, 121(Pt 3):599, 1976. 6.1.1

[29] Lori A Bolgla and Terry R Malone. Plantar fasciitis and the windlass mechanism: a biomechanical link to clinical practice. *Journal of athletic training*, 39(1):77, 2004. 6.1.2

[30] P Bouche, F Cattelin, O Saint-Jean, JM Leger, S Queslati, D Guez, A Moulonguet, Y Brault, JP Aquino, and P Simunek. Clinical and electrophysiological study of the peripheral nervous system in the elderly. *Journal of neurology*, 240(5):263–268, 1993. 6.2.1, 6.2.2, 6.3

[31] JM Brockway. Derivation of formulae used to calculate energy expenditure in man. *Human nutrition. Clinical nutrition*, 41(6):463–471, 1987. 6.1.3

[32] T Graham Brown. The intrinsic factors in the act of progression in the mammal. *Proceedings of the Royal Society of London. Series B, containing papers of a biological character*, pages 308–319, 1911. 2.1.3

[33] T Graham Brown. On the nature of the fundamental activity of the nervous centres; together with an analysis of the conditioning of rhythmic activity in progression, and a theory of the evolution of function in the nervous system. *The Journal of Physiology*, 48(1):18, 1914. 2.1.3

[34] Harsh H Buddhadev and Philip E Martin. Effects of age and physical activity status on redistribution of joint work during walking. *Gait & Posture*, 50:131–136, 2016. 6.2.3

[35] Jean-Marie Cabelguen, Céline Bourcier-Lucas, and Réjean Dubuc. Bimodal locomotion elicited by electrical stimulation of the midbrain in the salamander notophthalmus viridescens. *The Journal of Neuroscience*, 23(6):2434–2439, 2003. 2.1.2

[36] Blair Calancie, Belinda Needham-Shropshire, Patrick Jacobs, Keith Willer, Gregory Zych, and Barth A Green. Involuntary stepping after chronic spinal cord injury. *Brain*, 117(5):1143–1159, 1994. 2.2.2

[37] C Capaday and RB Stein. Amplitude modulation of the soleus h-reflex in the human during walking and standing. *The Journal of neuroscience*, 6(5):1308–1313, 1986. 2.2.2, 5.1.1

[38] C Capaday and RB Stein. Difference in the amplitude of the human soleus h reflex during walking and running. *The Journal of physiology*, 392(1):513–522, 1987. 1.2, 2.2.2, 2.1

[39] Charles Capaday. The special nature of human walking and its neural control. *Trends in neurosciences*, 25(7):370–376, 2002. 2, 2.2, 2.3, 5.3

[40] Germana Cappellini, Yuri P Ivanenko, Richard E Poppele, and Francesco Lacquaniti. Motor patterns in human walking and running. *Journal of neurophysiology*, 95(6):3426–3437, 2006. 2.1.4, 2.2.1, 2.2.2

[41] Paolo Caravaggi, Todd Pataky, John Y Goulermas, Russel Savage, and Robin Crompton. A dynamic model of the windlass mechanism of the foot: evidence for early stance phase preloading of the plantar aponeurosis. *Journal of Experimental Biology*, 212(15):2491–2499, 2009. 6.1.2

[42] RF Chandler and CE Clauser. Investigation of inertial properties of the human body. *Us Department of Transportation, Report# DOT HS-801 430 Washington DC*, 1975. 3.2.1

[43] Vincent CK Cheung, Andrea d'Avella, Matthew C Tresch, and Emilio Bizzi. Central and sensory contributions to the activation and organization of muscle synergies during natural motor behaviors. *The Journal of neuroscience*, 25(27):6419–6434, 2005. 2.1.4

[44] Lars OD Christensen, P Johannsen, Thomas Sinkjær, N Petersen, HS Pyndt, and Jens Bo Nielsen. Cerebral activation during bicycle movements in man. *Experimental Brain Research*, 135(1):66–72, 2000. 2.2.2

[45] Anita D Christie, Anne Tonson, Ryan G Larsen, Jacob P DeBlois, and Jane A Kent. Human skeletal muscle metabolic economy in vivo: effects of contraction intensity, age, and mobility impairment. *American Journal of Physiology-Regulatory, Integrative and Comparative Physiology*, 307(9):R1124–R1135, 2014. 6.13, 6.2.4

[46] Anita D Christie, Stephen A Foulis, and Jane A Kent. Atp cost of muscle contraction is associated with motor unit discharge rate in humans. *Neuroscience Letters*, 629:186–188, 2016. 6.2.4

[47] Stacie A Chvatal and Lena H Ting. Voluntary and reactive recruitment of locomotor muscle synergies during perturbed walking. *The*

Journal of Neuroscience, 32(35):12237–12250, 2012. 2.2.2, 5.1.1

[48] François Clarac. Some historical reflections on the neural control of locomotion. *Brain research reviews*, 57(1):13–21, 2008. 2.1.3, 2.1.3

[49] Steven H Collins, Peter G Adamczyk, and Arthur D Kuo. Dynamic arm swinging in human walking. *Proceedings of the Royal Society of London B: Biological Sciences*, page rspb20090664, 2009. 2.2.1, 2.2.1

[50] Wikimedia Commons. Clione limacina, 2005. URL https://commons.wikimedia.org/wiki/File:Clione_limacina5.jpg. 2.1

[51] Kevin E Conley, Sharon A Jubrias, M Elaine Cress, and Peter Esselman. Exercise efficiency is reduced by mitochondrial uncoupling in the elderly. *Experimental physiology*, 98(3):768–777, 2013. 6.2.4

[52] BA Conway, H Hultborn, and O Kiehn. Proprioceptive input resets central locomotor rhythm in the spinal cat. *Experimental Brain Research*, 68(3):643–656, 1987. 5.3

[53] Stelian Coros, Philippe Beaudoin, and Michiel van de Panne. Robust task-based control policies for physics-based characters. *ACM Trans. Graph. (Proc. SIGGRAPH Asia)*, 28(5):Article 170, 2009. 4.4

[54] Grégoire Courtine, Susan J Harkema, Christine J Dy, Yuri P Gerasimenko, and Poul Dyhre-Poulsen. Modulation of multisegmental monosynaptic responses in a variety of leg muscles during walking and running in humans. *The Journal of physiology*, 582(3):1125–1139, 2007. 5, 5.1.1, 5.1.1, 5.1.2, 5.1.2

[55] Neil J Cronin, Masaki Ishikawa, Michael J Grey, Richard Af Klint, Paavo V Komi, Janne Avela, Thomas Sinkjaer, and Michael Voigt. Mechanical and neural stretch responses of the human soleus muscle at different walking speeds. *The Journal of physiology*, 587(13):3375–3382, 2009. 2.2.2, 5.1.1

[56] Roy D Crowninshield and Richard A Brand. A physiologically based criterion of muscle force prediction in locomotion. *Journal of biomechanics*, 14(11):793–801, 1981. 6.15

[57] Joseph M Czerniecki. Foot and ankle biomechanics in walking and running: A review. *American journal of physical medicine & rehabilitation*, 67(6):246–252, 1988. 6.1.2

[58] Leonardo da Vinci. URL http://www.great-quotes.com/quote/52031. 6.1.1

[59] Mohsen Damavandi, Philippe C Dixon, and David J Pearsall. Ground reaction force adaptations during cross-slope walking and running. *Human movement science*, 31(1):182–189, 2012. 4.3

[60] Tatiana G Deliagina, Yuri I Arshavsky, and Grigori N Orlovsky. Control of spatial orientation in a mollusc. *Nature*, 393(6681):172–175, 1998. 2.1, 2.1.1

[61] Matthew J Delmonico, Tamara B Harris, Marjolein Visser, Seok Won Park, Molly B Conroy, Pedro Velasquez-Mieyer, Robert Boudreau, Todd M Manini, Michael Nevitt, Anne B Newman, et al. Longitudinal study of muscle strength, quality, and adipose tissue infiltration. *The American journal of clinical nutrition*, 90(6):1579–1585, 2009. 6.2.2, 6.2.3

[62] Ruta Desai and Hartmut Geyer. Muscle-reflex control of robust swing leg placement. In *Robotics and Automation (ICRA), 2013 IEEE International Conference on*, pages 2169–2174. IEEE, 2013. 4.1.1

[63] Paul DeVita and Tibor Hortobagyi. Age causes a redistribution of joint torques and powers during gait. *Journal of applied physiology*, 88 (5):1804–1811, 2000. 6.2.3, 6.11

[64] V Dietz, M Bischer, M Faist, and M Trippel. Amplitude modulation of the human quadriceps tendon jerk reflex during gait. *Experimental brain research*, 82(1):211–213, 1990. 2.2.2, 5, 5.1.1, 5.1.1, 5.1.2

[65] Volker Dietz, Roland Müller, and Gery Colombo. Locomotor activity in spinal man: significance of afferent input from joint and load receptors. *Brain*, 125(12):2626–2634, 2002. 2.2.2

[66] Nadia Dominici, Yuri P Ivanenko, Germana Cappellini, Andrea dAvella, Vito Mondì, Marika Cicchese, Adele Fabiano, Tiziana Silei, Ambrogio Di Paolo, Carlo Giannini, et al. Locomotor primitives in newborn babies and their development. *Science*, 334(6058):997–999, 2011. 2.1.4, 5.3

[67] J Maxwell Donelan, Rodger Kram, and Arthur D Kuo. Mechanical work for step-to-step transitions is a major determinant of the metabolic cost of human walking. *Journal of Experimental Biology*, 205(23):3717–3727, 2002. 2.3

[68] J Duysens, AAM Tax, M Trippel, and V Dietz. Phase-dependent reversal of reflexly induced movements during human gait. *Experimental brain research*, 90(2):404–414, 1992. 2.1

[69] Jaak Duysens, F Clarac, and Holk Cruse. Load-regulating mechanisms in gait and posture: comparative aspects. *Physiological reviews*, 80(1):83–133, 2000. 5.2.2

[70] Jacques Duysens and Henry WAA Van de Crommert. Neural control of locomotion; part 1: The central pattern generator from cats to humans. *Gait & posture*, 7(2):131–141, 1998. 5.3

[71] Florin Dzeladini, Jesse Van Den Kieboom, and Auke Ijspeert. The contribution of a central pattern generator in a reflex-based neuromuscular model. *Frontiers in human neuroscience*, 8, 2014. 5, 5.3

[72] JC Eccles, Rosamond M Eccles, and A Lundberg. The convergence of monosynaptic excitatory afferents on to many different species of alpha motoneurones. *The Journal of Physiology*, 137(1):22–50, 1957. 2.1.3

131

[73] John Carew Eccles, P Fatt, and K Koketsu. Cholinergic and inhibitory synapses in a pathway from motor-axon collaterals to motoneurones. *The Journal of Physiology*, 126(3):524–562, 1954. 2.1.3

[74] Michael F Eilenberg, Hartmut Geyer, and Hugh Herr. Control of a powered ankle–foot prosthesis based on a neuromuscular model. *Neural Systems and Rehabilitation Engineering, IEEE Transactions on*, 18(2):164–173, 2010. 6

[75] Janice J Eng and David A Winter. Kinetic analysis of the lower limbs during walking: what information can be gained from a three-dimensional model? *Journal of biomechanics*, 28(6):753–758, 1995. 4.3

[76] Janice J Eng, David A Winter, and Aftab E Patla. Strategies for recovery from a trip in early and late swing during human walking. *Experimental Brain Research*, 102(2):339–349, 1994. 2.2.1, 2.2.1, 2.2.2, 5.1.1, 5.2.2

[77] Ahmet Erdemir, Andrew J Hamel, Andrew R Fauth, Stephen J Piazza, and Neil A Sharkey. Dynamic loading of the plantar aponeurosis in walking. *J Bone Joint Surg Am*, 86(3):546–552, 2004. 6.1.2

[78] Michael Faist, Christian Blahak, Jacques Duysens, and Wiltrud Berger. Modulation of the biceps femoris tendon jerk reflex during human locomotion. *Experimental brain research*, 125(3):265–270, 1999. 2.2.2, 5, 5.1.1, 5.1.1, 5.1.2

[79] Claire T Farley and Octavio Gonzalez. Leg stiffness and stride frequency in human running. *Journal of biomechanics*, 29(2):181–186, 1996. 2.2.1, 2.3

[80] Brent Fedirchuk, J Nielsen, Nicolas Petersen, and Hans Hultborn. Pharmacologically evoked fictive motor patterns in the acutely spinalized marmoset monkey (callithrix jacchus). *Experimental brain research*, 122(3):351–361, 1998. 2.1.3

[81] Siyuan Feng, Eric Whitman, X Xinjilefu, and Christopher G Atkeson. Optimization based full body control for the atlas robot. In *Humanoid Robots (Humanoids), 2014 14th IEEE-RAS International Conference on*, pages 120–127. IEEE, 2014. 6.3.1

[82] Reed Ferber, Sean T Osis, Jennifer L Hicks, and Scott L Delp. Gait biomechanics in the era of data science. *Journal of Biomechanics*, 49 (16):3759–3761, 2016. 4.4

[83] Anne-Marie Ferrandez, Jean Pailhous, and Madeleine Durup. Slowness in elderly gait. *Experimental aging research*, 16(2):79–89, 1990. 6.2.1, 6.2.3

[84] Daniel P Ferris, Micky Louie, and Claire T Farley. Running in the real world: adjusting leg stiffness for different surfaces. *Proceedings of the Royal Society of London. Series B: Biological Sciences*, 265(1400):989–994, 1998. 4.2.3

[85] Eric A Fuller. The windlass mechanism of the foot. a mechanical model to explain pathology. *Journal of the American Podiatric Medical Association*, 90(1):35–46, 2000. 6.1.1

[86] Dympna Gallagher, Marjolein Visser, Ronald E De Meersman, Dennis Sepúlveda, Richard N Baumgartner, Richard N Pierson, Tamara Harris, and Steven B Heymsfield. Appendicular skeletal muscle mass: effects of age, gender, and ethnicity. *Journal of applied physiology*, 83(1):229–239, 1997. 6.2.1

[87] Thomas Geijtenbeek, Michiel van de Panne, and A Frank van der Stappen. Flexible muscle-based locomotion for bipedal creatures. *ACM Transactions on Graphics (TOG)*, 32(6):206, 2013. 3.6, 6

[88] Hartmut Geyer and Hugh Herr. A muscle-reflex model that encodes principles of legged mechanics produces human walking dynamics and muscle activities. *Neural Systems and Rehabilitation Engineering, IEEE Transactions on*, 18(3):263–273, 2010. 1.2, 2.2, 2.3, 2.3.1, 2.3.2, 3.2.1, 3.2.2, 3.2.2, 3.2.3, 3.4, 4.1.1, 4.2.1, 5, 6, 6.1.2, 6.2

[89] Hartmut Geyer, Andre Seyfarth, and Reinhard Blickhan. Positive force feedback in bouncing gaits? *Proceedings of the Royal Society of London B: Biological Sciences*, 270(1529):2173–2183, 2003. 2.3.2, 6.3.3

[90] Hartmut Geyer, Andre Seyfarth, and Reinhard Blickhan. Compliant leg behaviour explains basic dynamics of walking and running. *Proceedings of the Royal Society of London B: Biological Sciences*, 273(1603):2861–2867, 2006. 2.3, 2.3.2

[91] Daniel J Goble, James P Coxon, Nicole Wenderoth, Annouchka Van Impe, and Stephan P Swinnen. Proprioceptive sensibility in the elderly: degeneration, functional consequences and plastic-adaptive processes. *Neuroscience & Biobehavioral Reviews*, 33(3):271–278, 2009. 6.2.1, 6.2.2, 6.3

[92] Bret H Goodpaster, Seok Won Park, Tamara B Harris, Steven B Kritchevsky, Michael Nevitt, Ann V Schwartz, Eleanor M Simonsick, Frances A Tylavsky, Marjolein Visser, and Anne B Newman. The loss of skeletal muscle strength, mass, and quality in older adults: the health, aging and body composition study. *The Journals of Gerontology Series A: Biological Sciences and Medical Sciences*, 61(10): 1059–1064, 2006. 6.2.1, 6.2.2, 6.3, 6.2.3

[93] Michael J Grey, Michel Ladouceur, Jacob B Andersen, Jens Bo Nielsen, and Thomas Sinkjær. Group ii muscle afferents probably contribute to the medium latency soleus stretch reflex during walking in humans. *The Journal of physiology*, 534(3):925–933, 2001. 2.2, 2.3.1, 3.3, 5.2.2

[94] Michael J Grey, Jens Bo Nielsen, Nazarena Mazzaro, and Thomas Sinkjær. Positive force feedback in human walking. *The Journal of physiology*, 581(1):99–105, 2007. 2.1

[95] S. Grillner. Locomotion in vertebrates: central mechanisms and reflex interaction. *Physiol Rev*, 55(2):247–304, 1975. 2.1.3

[96] Sten Grillner, AP Georgopoulos, LM Jordan, PSG Stein, and S Grillner. Neurons, networks, and motor behavior, 1997. 2.1.2, 5.3

[97] Michael Günther and Hanns Ruder. Synthesis of two-dimensional human walking: a test of the λ-model. *Biological cybernetics*, 89(2): 89–106, 2003. 2.2, 2.3, 3.2.1

[98] Sehoon Ha and Katsu Yamane. Reducing hardware experiments for model learning and policy optimization. In *Robotics and Automation (ICRA), 2015 IEEE International Conference on*, pages 2620–2626. IEEE, 2015. 6.3.5

[99] Samuel R Hamner, Ajay Seth, and Scott L Delp. Muscle contributions to propulsion and support during running. *Journal of biomechanics*, 43(14):2709–2716, 2010. 2.3

[100] Nikolaus Hansen. The cma evolution strategy: a comparing review. In *Towards a new evolutionary computation*, pages 75–102. Springer, 2006. 3.6, 6.3.3

[101] Kazunori Hase and Nobutoshi Yamazaki. Computational evolution of human bipedal walking by a neuro-musculo-skeletal model. *Artificial Life and Robotics*, 3(3):133–138, 1999. 2.2

[102] Kazunori Hase and Nobutoshi Yamazaki. Computer simulation study of human locomotion with a three-dimensional entire-body neuro-musculo-skeletal model. i. acquisition of normal walking. *JSME International Journal Series C Mechanical Systems, Machine Elements and Manufacturing*, 45(4):1040–1050, 2002. 2.2, 2.3.1, 5.3

[103] Kazunori Hase, Kazuo Miyashita, Sooyol Ok, and Yoshiki Arakawa. Human gait simulation with a neuromusculoskeletal model and evolutionary computation. *The Journal of Visualization and Computer Animation*, 14(2):73–92, 2003. 1.1, 2.2, 2.3, 2.3.1

[104] Jorunn L Helbostad, Sara Leirfall, Rolf Moe-Nilssen, and Olav Sletvold. Physical fatigue affects gait characteristics in older persons. *The Journals of Gerontology Series A: Biological Sciences and Medical Sciences*, 62(9):1010–1015, 2007. 6.2.4

[105] Rodolphe Héliot and Bernard Espiau. Multisensor input for cpg-based sensory—motor coordination. *Robotics, IEEE Transactions on*, 24(1):191–195, 2008. 6.3.1

[106] JH Hicks. The mechanics of the foot: I. the joints. *Journal of Anatomy*, 87(Pt 4):345, 1953. 6.1.1

[107] JH Hicks. The mechanics of the foot: Ii. the plantar aponeurosis and the arch. *Journal of anatomy*, 88(Pt 1):25, 1954. 6.1.1, 6.1.2

[108] Joan E Himann, David A Cunningham, Peter A Rechnitzer, and Donald H Paterson. Age-related changes in speed of walking. *Medicine and science in sports and exercise*, 20(2):161–166, 1988. 6.2.1, 6.2.3

[109] Richard N Hinrichs. Upper extremity function in running. 11: Angular momentum considerations. *International Journal of Sport Biomechanics*, 3:242–263, 1987. 2.2.1

[110] Richard N Hinrichs, Peter R Cavanagh, and Keith R Williams. Upper extremity function in running. i: Center of mass and propulsion considerations. *International Journal of Sport Biomechanics*, 3:222–241, 1987. 2.2.1

[111] Eishi Hirasaki, Steven T Moore, Theodore Raphan, and Bernard Cohen. Effects of walking velocity on vertical head and body movements during locomotion. *Experimental brain research*, 127(2):117–130, 1999. 2.2.1

[112] AL Hof and Jaak Duysens. Responses of human hip abductor muscles to lateral balance perturbations during walking. *Experimental brain research*, 230(3):301–310, 2013. 2.2.1, 2.2.1, 5.3

[113] JA Hoffer, N Sugano, GE Loeb, WB Marks, MJ O'Donovan, and CA Pratt. Cat hindlimb motoneurons during locomotion. ii. normal activity patterns. *Journal of Neurophysiology*, 57(2):530–553, 1987. 2.3

[114] Tibor Hortobágyi, Adria Finch, Stanislaw Solnik, Patrick Rider, and Paul DeVita. Association between muscle activation and metabolic cost of walking in young and old adults. *The Journals of Gerontology Series A: Biological Sciences and Medical Sciences*, 66(5):541–547, 2011. 6.2.1

[115] Christian Hubicki, Andy Abate, Patrick Clary, Siavash Rezazadeh, Mikhail Jones, Andrew Peekema, Johnathan Van Why, Ryan Domres, Albert Wu, William Martin, Hartmut Geyer, and Jonathan Hurst. Walking and running with passive compliance: Lessons from engineering a live demonstration of the atrias biped. *IEEE Robotics and Automation Magazine*, 2(4.1):4–1, 2016. 6.3.5

[116] H Hultborn and Jens Bo Nielsen. Spinal control of locomotion–from cat to man. *Acta Physiologica*, 189(2):111–121, 2007. 2.1.3, 2.2.2

[117] Hans Hultborn. Spinal reflexes, mechanisms and concepts: from eccles to lundberg and beyond. *Progress in neurobiology*, 78(3):215–232, 2006. 2.1.3, 2.1.3

[118] Gary R Hunter, Brad R Newcomer, D Enette Larson-Meyer, Marcas M Bamman, and Roland L Weinsier. Muscle metabolic economy is inversely related to exercise intensity and type ii myofiber distribution. *Muscle & nerve*, 24(5):654–661, 2001. 6.13, 6.2.4

[119] Auke Jan Ijspeert. Central pattern generators for locomotion control in animals and robots: a review. *Neural Networks*, 21(4):642–653, 2008. 2.1.3, 2.1.3, 5.3

[120] Yuri P Ivanenko, Germana Cappellini, Nadia Dominici, Richard E Poppele, and Francesco Lacquaniti. Coordination of locomotion with voluntary movements in humans. *The Journal of neuroscience*, 25(31):7238–7253, 2005. 2.1.4, 2.2.2

[121] Yuri P Ivanenko, Richard E Poppele, and Francesco Lacquaniti. Motor control programs and walking. *The Neuroscientist*, 12(4):339–348, 2006. 2.1.4

[122] Robert K Jensen and Paula Fletcher. Distribution of mass to the segments of elderly males and females. *Journal of biomechanics*, 27(1): 89–96, 1994. 6.2.1, 6.2.2, 6.3

[123] Sungho Jo. A neurobiological model of the recovery strategies from perturbed walking. *Biosystems*, 90(3):750–768, 2007. 2.2, 5

[124] Sungho Jo. Hypothetical neural control of human bipedal walking with voluntary modulation. *Medical & biological engineering &*

computing, 46(2):179–193, 2008. 2.2, 2.3.1

[125] Sungho Jo and Steve G Massaquoi. A model of cerebellum stabilized and scheduled hybrid long-loop control of upright balance. *Biological cybernetics*, 91(3):188–202, 2004. 2.2

[126] Sungho Jo and Steve G Massaquoi. A model of cerebrocerebello-spinomuscular interaction in the sagittal control of human walking. *Biological cybernetics*, 96(3):279–307, 2007. 2.2, 2.3, 5.3, 5.3

[127] Matthew Johnson, Brandon Shrewsbury, Sylvain Bertrand, Tingfan Wu, Daniel Duran, Marshall Floyd, Peter Abeles, Douglas Stephen, Nathan Mertins, Alex Lesman, et al. Team ihmc's lessons learned from the darpa robotics challenge trials. *Journal of Field Robotics*, 32 (2):192–208, 2015. 6.3.1

[128] James Oat JudgeRoy, B Davis, and Sylvia Õunpuu. Step length reductions in advanced age: the role of ankle and hip kinetics. *The Journals of Gerontology Series A: Biological Sciences and Medical Sciences*, 51(6):M303–M312, 1996. 6.2.3

[129] Shuuji Kajita, Fumio Kanehiro, Kenji Kaneko, Kazuhito Yokoi, and Hirohisa Hirukawa. The 3d linear inverted pendulum mode: A simple modeling for a biped walking pattern generation. In *Intelligent Robots and Systems, 2001. Proceedings. 2001 IEEE/RSJ International Conference on*, volume 1, pages 239–246. IEEE, 2001. 2.3, 4.1.2, 6.3.5

[130] Shuuji Kajita, Fumio Kanehiro, Kenji Kaneko, Kiyoshi Fujiwara, Kensuke Harada, Kazuhito Yokoi, and Hirohisa Hirukawa. Biped walking pattern generation by using preview control of zero-moment point. In *Robotics and Automation, 2003. Proceedings. ICRA'03. IEEE International Conference on*, volume 2, pages 1620–1626. IEEE, 2003. 6.3.1

[131] Eric R Kandel, James H Schwartz, Thomas M Jessell, Steven A Siegelbaum, and A James Hudspeth. *Principles of neural science*, volume 4. McGraw-hill New York, 2000. 2.3

[132] Alexandria Kappel-Bargas, Richard D Woolf, Mark W Cornwall, and Thomas G McPoil. The windlass mechanism during normal walking and passive first metatarsalphalangeal joint extension. *Clinical Biomechanics*, 13(3):190–194, 1998. 6.1.1

[133] D Casey Kerrigan, Mary K Todd, Ugo Della Croce, Lewis A Lipsitz, and James J Collins. Biomechanical gait alterations independent of speed in the healthy elderly: evidence for specific limiting impairments. *Archives of physical medicine and rehabilitation*, 79(3):317–322, 1998. 6.2.2, 6.2.3, 6.11

[134] Ole Kiehn. Decoding the organization of spinal circuits that control locomotion. *Nature Reviews Neuroscience*, 2016. 5.3

[135] Jung-Yup Kim, Ill-Woo Park, and Jun-Ho Oh. Walking control algorithm of biped humanoid robot on uneven and inclined floor. *Journal of Intelligent and Robotic Systems*, 48(4):457–484, 2007. 2.3

[136] Seyoung Kim and Sukyung Park. Leg stiffness increases with speed to modulate gait frequency and propulsion energy. *Journal of Biomechanics*, 44(7):1253–1258, 2011. 2.2.1

[137] Woo Sub Kim and Eun Young Kim. Comparing self-selected speed walking of the elderly with self-selected slow, moderate, and fast speed walking of young adults. *Annals of rehabilitation medicine*, 38(1):101–108, 2014. 6.11

[138] Youngwoo Kim, Yusuke Tagawa, Goro Obinata, and Kazunori Hase. Robust control of cpg-based 3d neuromusculoskeletal walking model. *Biological cybernetics*, 105(3-4):269–282, 2011. 2.2, 2.3.1, 5

[139] Hiroshi Kinoshita. Effects of different loads and carrying systems on selected biomechanical parameters describing walking gait. *Ergonomics*, 28(9):1347–1362, 1985. 2.2.1

[140] Maria Knikou and William Zev Rymer. Effects of changes in hip joint angle on h-reflex excitability in humans. *Experimental brain research*, 143(2):149–159, 2002. 2.2, 3.3

[141] Rodger Kram, Antoinette Domingo, and Daniel P Ferris. Effect of reduced gravity on the preferred walk-run transition speed. *The Journal of Experimental Biology*, 200(4):821–826, 1997. 2.3

[142] Scott Kuindersma, Frank Permenter, and Russ Tedrake. An efficiently solvable quadratic program for stabilizing dynamic locomotion. In *Robotics and Automation (ICRA), 2014 IEEE International Conference on*, pages 2589–2594. IEEE, 2014. 6.3.1

[143] Arthur D Kuo. Stabilization of lateral motion in passive dynamic walking. *The International journal of robotics research*, 18(9):917–930, 1999. 2.2

[144] Arthur D Kuo. A simple model of bipedal walking predicts the preferred speed–step length relationship. *Journal of biomechanical engineering*, 123(3):264–269, 2001. 2.3

[145] Jason J Kutch and Francisco J Valero-Cuevas. Challenges and new approaches to proving the existence of muscle synergies of neural origin. *PLoS Comput. Biol*, 8(5), 2012. 2.1.4

[146] Francesco Lacquaniti, Yuri P Ivanenko, and Myrka Zago. Patterned control of human locomotion. *The Journal of physiology*, 590(10): 2189–2199, 2012. 2.1.4

[147] Michail G Lagoudakis and Ronald Parr. Least-squares policy iteration. *The Journal of Machine Learning Research*, 4:1107–1149, 2003. 4.4

[148] Yves Laporte and David PC Lloyd. Nature and significance of the reflex connections established by large afferent fibers of muscular origin. *American Journal of Physiology–Legacy Content*, 169(3):609–621, 1952. 2.1.3

[149] Fulvio Lauretani, Cosimo Roberto Russo, Stefania Bandinelli, Benedetta Bartali, Chiara Cavazzini, Angelo Di Iorio, Anna Maria Corsi,

Taina Rantanen, Jack M Guralnik, and Luigi Ferrucci. Age-associated changes in skeletal muscles and their effect on mobility: an operational diagnosis of sarcopenia. *Journal of applied physiology*, 95(5):1851–1860, 2003. 6.2.1, 6.2.3

[150] Sergey Levine, Chelsea Finn, Trevor Darrell, and Pieter Abbeel. End-to-end training of deep visuomotor policies. *Journal of Machine Learning Research*, 17(39):1–40, 2016. 4.4

[151] Jan Lexell. Human aging, muscle mass, and fiber type composition. *The Journals of Gerontology Series A: Biological Sciences and Medical Sciences*, 50(Special Issue):11–16, 1995. 6.2.2

[152] Susanne W Lipfert, Michael Günther, Daniel Renjewski, Sten Grimmer, and Andre Seyfarth. A model-experiment comparison of system dynamics for human walking and running. *Journal of Theoretical Biology*, 292:11–17, 2012. 4.2.3

[153] M Llewellyn, JF Yang, and A Prochazka. Human h-reflexes are smaller in difficult beam walking than in normal treadmill walking. *Experimental brain research*, 83(1):22–28, 1990. 2.1

[154] Rosalie B Lopopolo, Melissa Greco, Dorianne Sullivan, Rebecca L Craik, and Kathleen K Mangione. Effect of therapeutic exercise on gait speed in community-dwelling elderly people: a meta-analysis. *Physical Therapy*, 86(4):520, 2006. 6.2.4

[155] A Lundberg, K Malmgren, and ED Schomburg. Reflex pathways from group ii muscle afferents. 3. secondary spindle afferents and the fra: a new hypothesis. *Experimental Brain Research*, 65(2):294–306, 1987. 5.2.2

[156] Marilyn MacKay-Lyons. Central pattern generation of locomotion: a review of the evidence. *Physical therapy*, 82(1):69–83, 2002. 1.2, 2.1.3, 2.2.2, 2.3, 5.3

[157] Davide Malatesta, David Simar, Yves Dauvilliers, Robin Candau, Fabio Borrani, Christian Préfaut, and Corinne Caillaud. Energy cost of walking and gait instability in healthy 65-and 80-yr-olds. *Journal of applied physiology*, 95(6):2248–2256, 2003. 6.2.1

[158] PHILIP E Martin, DEBRA E Rothstein, and DOUGLAS D Larish. Effects of age and physical activity status on the speed-aerobic demand relationship of walking. *Journal of applied physiology*, 73(1):200–206, 1992. 6.2.1, 6.9, 6.2.1, 6.2.3, 6.2.4

[159] William C Martin, Albert Wu, and Hartmut Geyer. Robust spring mass model running for a physical bipedal robot. In *Robotics and Automation (ICRA), 2015 IEEE International Conference on*, pages 6307–6312. IEEE, 2015. 2.3, 6.3.2

[160] Kiyotoshi Matsuoka. Sustained oscillations generated by mutually inhibiting neurons with adaptation. *Biological cybernetics*, 52(6): 367–376, 1985. 2.1.3, 5.3

[161] Jonathan S Matthis and Brett R Fajen. Visual control of foot placement when walking over complex terrain. *Journal of Experimental Psychology: Human Perception and Performance*, 40(1):106–115, 2013. 2.2.1, 2.2.1

[162] David A McCrea and Ilya A Rybak. Organization of mammalian locomotor rhythm and pattern generation. *Brain research reviews*, 57 (1):134–146, 2008. 2.1.3, 5.3

[163] Matthew BA McCullough, Stacie I Ringleb, Kenichiro Arai, Harold B Kitaoka, and Kenton R Kaufman. Moment arms of the ankle throughout the range of motion in three planes. *Foot & Ankle International*, 32(3):300–306, 2011. 3.2.3

[164] S Meunier, A Penicaud, E Pierrot-Deseilligny, and A Rossi. Monosynaptic ia excitation and recurrent inhibition from quadriceps to ankle flexors and extensors in man. *The Journal of physiology*, 423(1):661–675, 1990. 2.2, 3.3

[165] Omar S Mian, Jeanette M Thom, Luca P Ardigò, Marco V Narici, and Alberto E Minetti. Metabolic cost, mechanical work, and efficiency during walking in young and older men. *Acta physiologica*, 186(2):127–139, 2006. 6.2.1, 6.2.1, 6.2.3

[166] Omar S Mian, Vasilios Baltzopoulos, Alberto E Minetti, and Marco V Narici. The impact of physical training on locomotor function in older people. *Sports medicine*, 37(8):683–701, 2007. 6.2.4

[167] Robyn L Mildren, Martin Zaback, Allan L Adkin, James S Frank, and Leah R Bent. Reliability of the achilles tendon tap reflex evoked during stance using a pendulum hammer. *Gait & posture*, 43:182–186, 2016. 5.1.2

[168] Ross H Miller. A comparison of muscle energy models for simulating human walking in three dimensions. *Journal of biomechanics*, 47 (6):1373–1381, 2014. 3.5

[169] Ross H Miller, Brian R Umberger, Joseph Hamill, and Graham E Caldwell. Evaluation of the minimum energy hypothesis and other potential optimality criteria for human running. *Proceedings of the Royal Society of London B: Biological Sciences*, page rspb20112015, 2011. 3.5, 3.5, 6.2.3, 6.15

[170] Karen Minassian, Ursula S Hofstoetter, Florin Dzeladini, Pierre A Guertin, and Auke Ijspeert. The human central pattern generator for locomotion: Does it exist and contribute to walking? *The Neuroscientist*, page 1073858417699790, 2017. 2.2.2

[171] Seiichi Miyakoshi, Gentaro Taga, Yasuo Kuniyoshi, and Akihiko Nagakubo. Three dimensional bipedal stepping motion using neural oscillators-towards humanoid motion in the real world. In *Intelligent Robots and Systems, 1998. Proceedings., 1998 IEEE/RSJ International Conference on*, volume 1, pages 84–89. IEEE, 1998. 2.3, 2.2

[172] Volodymyr Mnih, Koray Kavukcuoglu, David Silver, Andrei A Rusu, Joel Veness, Marc G Bellemare, Alex Graves, Martin Riedmiller, Andreas K Fidjeland, Georg Ostrovski, et al. Human-level control through deep reinforcement learning. *Nature*, 518(7540):529–533, 2015. 4.4

[173] Volodymyr Mnih, Adria Puigdomenech Badia, Mehdi Mirza, Alex Graves, Timothy P Lillicrap, Tim Harley, David Silver, and Koray Kavukcuoglu. Asynchronous methods for deep reinforcement learning. In *International Conference on Machine Learning*, 2016. 4.4

[174] Simon Mochon and Thomas A McMahon. Ballistic walking. *Journal of biomechanics*, 13(1):49–57, 1980. 4.2.2

[175] Vito Monaco and Silvestro Micera. Age-related neuromuscular adaptation does not affect the mechanical efficiency of lower limbs during walking. *Gait & posture*, 36(3):350–355, 2012. 6.2.1, 6.2.1, 6.2.2, 6.3, 6.2.3, 6.11

[176] Vito Monaco, Lucio A Rinaldi, Giovanna Macrì, and Silvestro Micera. During walking elders increase efforts at proximal joints and keep low kinetics at the ankle. *Clinical Biomechanics*, 24(6):493–498, 2009. 6.2.3, 6.11, 6.2.3

[177] Igor Mordatch and Emo Todorov. Combining the benefits of function approximation and trajectory optimization. In *Robotics: Science and Systems*, 2014. 4.4

[178] Igor Mordatch, Kendall Lowrey, Galen Andrew, Zoran Popovic, and Emanuel V Todorov. Interactive control of diverse complex characters with neural networks. In *Advances in Neural Information Processing Systems*, pages 3132–3140, 2015. 4.4

[179] Igor Mordatch, Kendall Lowrey, and Emanuel Todorov. Ensemble-cio: Full-body dynamic motion planning that transfers to physical humanoids. In *Intelligent Robots and Systems (IROS), 2015 IEEE/RSJ International Conference on*, pages 5307–5314. IEEE, 2015. 6.3.5

[180] Jun Morimoto, Gen Endo, Jun Nakanishi, and Gordon Cheng. A biologically inspired biped locomotion strategy for humanoid robots: Modulation of sinusoidal patterns by a coupled oscillator model. *Robotics, IEEE Transactions on*, 24(1):185–191, 2008. 6.3.1

[181] Akihiko Murai and Katsu Yamane. A neuromuscular locomotion controller that realizes human-like responses to unexpected disturbances. In *Robotics and Automation (ICRA), 2011 IEEE International Conference on*, pages 1997–2002. IEEE, 2011. 5

[182] MP Murray, LA Mollinger, GM Gardner, and SB Sepic. Kinematic and emg patterns during slow, free, and fast walking. *Journal of Orthopaedic Research*, 2(3):272–280, 1984. 4.2.3

[183] Tsuyoshi Nakajima, Shinya Suzuki, Genki Futatsubashi, Hiroyuki Ohtsuska, Rinaldo Andre Mezzarane, Trevor S Barss, Taryn Klarner, E Paul Zehr, and Tomoyoshi Komiyama. Regionally distinct cutaneous afferent populations contribute to reflex modulation evoked by stimulation of the tibial nerve during walking. *Journal of neurophysiology*, pages jn–01011, 2016. 2.2.2, 5.2.2

[184] John Nassour, Patrick Hénaff, Fethi Benouezdou, and Gordon Cheng. Multi-layered multi-pattern cpg for adaptive locomotion of humanoid robots. *Biological cybernetics*, 108(3):291–303, 2014. 6.3.1

[185] Gabe Nelson, Aaron Saunders, Neil Neville, Ben Swilling, Joe Bondaryk, Devin Billings, Chris Lee, Robert Playter, and Marc Raibert. Petman: A humanoid robot for testing chemical protective clothing. *Journal of the Robotics Society of Japan*, 30(4):372–377, 2012. 6.3.1

[186] A Nene, C Byrne, and H Hermens. Is rectus femoris really a part of quadriceps?: Assessment of rectus femoris function during gait in able-bodied adults. *Gait & posture*, 20(1):1–13, 2004. 5.2.1

[187] Jens Bo Nielsen. How we walk: central control of muscle activity during human walking. *The Neuroscientist*, 9(3):195–204, 2003. 1.2, 2.2, 2.2.2

[188] Rachel Nilwik, Tim Snijders, Marika Leenders, Bart BL Groen, Janneau van Kranenburg, Lex B Verdijk, and Luc JC van Loon. The decline in skeletal muscle mass with aging is mainly attributed to a reduction in type ii muscle fiber size. *Experimental gerontology*, 48 (5):492–498, 2013. 6.2.1, 6.2.2, 6.3, 6.2.4

[189] Tom F Novacheck. The biomechanics of running. *Gait & posture*, 7(1):77–95, 1998. 2.2.1, 2.2.1

[190] Marie Engelene J Obien, Kosmas Deligkaris, Torsten Bullmann, Douglas J Bakkum, and Urs Frey. Revealing neuronal function through microelectrode array recordings. *Frontiers in neuroscience*, 8, 2015. 2.3

[191] G Obinata, K Hase, and A Nakayama. Controller design of musculoskeletal model for simulating bipedal walking. In *Annual Conference of the International FES Society*, 2004. 2.2, 2.3.1

[192] Katsuhiko Ogata and Yanjuan Yang. *Modern control engineering*. Prentice-Hall Englewood Cliffs, 1970. 5

[193] Naomichi Ogihara and Nobutoshi Yamazaki. Generation of human bipedal locomotion by a bio-mimetic neuro-musculo-skeletal model. *Biological cybernetics*, 84(1):1–11, 2001. 2.2, 2.3, 2.3.1, 2.3.2, 5.3

[194] Sooyol Ok and DuckSool Kim. Evolution of the cpg with sensory feedback for bipedal locomotion. In *Advances in Natural Computation*, pages 714–726. Springer, 2005. 2.2, 2.3.1

[195] Anderson Souza Castelo Oliveira, Leonardo Gizzi, Uwe Gustav Kersting, and Dario Farina. Modular organization of balance control following perturbations during walking. *Journal of neurophysiology*, 108(7):1895–1906, 2012. 5.2.2

[196] Grigoriĭ Nikolaevich Orlovskiĭ, TG Deliagina, and Sten Grillner. *Neuronal control of locomotion: from mollusc to man*. Oxford University Press, 1999. 1.1, 2, 2.1.1, 2.1.2, 2.2, 2.2.2

[197] Justus D Ortega and Claire T Farley. Individual limb work does not explain the greater metabolic cost of walking in elderly adults. *Journal of applied physiology*, 102(6):2266–2273, 2007. 6.2.1

[198] Justus D Ortega, Leslie A Fehlman, and Claire T Farley. Effects of aging and arm swing on the metabolic cost of stability in human walking. *Journal of biomechanics*, 41(16):3303–3308, 2008. 6.2.1

[199] Oxycon mobile device. URL http://www.carefusion.com. 6.1.3

[200] Yu V Panchin, RI Sadreev, and Yu I Arshavsky. Control of locomotion in marine mollusc clione limacina x. effects of acetylcholine antagonists. *Experimental brain research*, 106(1):135–144, 1995. 2.1.1

[201] Aftab E Patla and Joan N Vickers. How far ahead do we look when required to step on specific locations in the travel path during locomotion? *Experimental brain research*, 148(1):133–138, 2003. 2.2.1

[202] Michael J Pavol, Tammy M Owings, and Mark D Grabiner. Body segment inertial parameter estimation for the general population of older adults. *Journal of biomechanics*, 35(5):707–712, 2002. 6.2.1, 6.2.2, 6.3

[203] Xue Bin Peng, Glen Berseth, and Michiel van de Panne. Dynamic terrain traversal skills using reinforcement learning. *ACM Transactions on Graphics (to appear)*, 2015. 4.4

[204] Xue Bin Peng, Glen Berseth, and Michiel van de Panne. Terrain-adaptive locomotion skills using deep reinforcement learning. *ACM Transactions on Graphics (TOG)*, 35(4):81, 2016. 4.4

[205] Jacquelin Perry and Judith M. Burnfield. *Gait analysis: normal and pathological function*. SLACK Incorporated, 2nd edition, 2010. 1.1, 2.2.1, 2.2.1, 4.4, 4.2.2

[206] Nicolas T Petersen, Jane E Butler, Veronique Marchand-Pauvert, Rebecca Fisher, Annick Ledebt, Henrik S Pyndt, Naja L Hansen, and Jens B Nielsen. Suppression of emg activity by transcranial magnetic stimulation in human subjects during walking. *The Journal of Physiology*, 537(2):651–656, 2001. 2.2.2

[207] Daniel S Peterson and Philip E Martin. Effects of age and walking speed on coactivation and cost of walking in healthy adults. *Gait & posture*, 31(3):355–359, 2010. 6.2.1

[208] Joelle Pineau, Geoff Gordon, Sebastian Thrun, et al. Point-based value iteration: An anytime algorithm for pomdps. In *IJCAI*, volume 3, pages 1025–1032, 2003. 4.4

[209] T Pozzo, A Berthoz, and L Lefort. Head stabilization during various locomotor tasks in humans. *Experimental Brain Research*, 82(1): 97–106, 1990. 2.2.1

[210] Jerry Pratt, Chee-Meng Chew, Ann Torres, Peter Dilworth, and Gill Pratt. Virtual model control: An intuitive approach for bipedal locomotion. *The International Journal of Robotics Research*, 20(2):129–143, 2001. 6.3.5

[211] Gisela Pyka, Elizabeth Lindenberger, Susan Charette, and Robert Marcus. Muscle strength and fiber adaptations to a year-long resistance training program in elderly men and women. *Journal of Gerontology*, 49(1):M22–M27, 1994. 6.2.4

[212] Marc H Raibert. *Legged robots that balance*. MIT press, 1986. 4.1.2, 6.3.1, 6.3.5

[213] Alireza Ramezani, Jonathan W Hurst, Kaveh Akbari Hamed, and JW Grizzle. Performance analysis and feedback control of atrias, a three-dimensional bipedal robot. *Journal of Dynamic Systems, Measurement, and Control*, 136(2):021012, 2014. 6.3.2

[214] Michael H Rivner, Thomas R Swift, and Khalid Malik. Influence of age and height on nerve conduction. *Muscle & nerve*, 24(9): 1134–1141, 2001. 6.2.1, 6.2.2, 6.3

[215] Kathryn E Roach and Toni P Miles. Normal hip and knee active range of motion: the relationship to age. *Physical therapy*, 71(9): 656–665, 1991. 6.2.2, 6.3

[216] Jessica Rose, James Gibson Gamble, and Janet M Adams. *Human walking*. Lippincott Williams & Wilkins Philadelphia, 2006. 1.1, 4.3

[217] Serge Rossignol. Neural control of stereotypic limb movements. *Comprehensive Physiology*, 1996. 2.1.3

[218] E Saugen and NK Vollestad. Nonlinear relationship between heat production and force during voluntary contractions in humans. *Journal of Applied Physiology*, 79(6):2043–2049, 1995. 6.13, 6.2.4

[219] Alexander Schepelmann, Jessica Austin, and Hartmut Geyer. Evaluation of decentralized reactive swing-leg control on a powered robotic leg. In *Intelligent Robots and Systems (IROS), 2015 IEEE/RSJ International Conference on*, pages 381–386. IEEE, 2015. 6, 6.4

[220] Marco Schieppati. The hoffmann reflex: a means of assessing spinal reflex excitability and its descending control in man. *Progress in neurobiology*, 28(4):345–376, 1987. 2.2.2

[221] AM Schillings, BMH Van Wezel, TH Mulder, and J Duysens. Widespread short-latency stretch reflexes and their modulation during stumbling over obstacles. *Brain research*, 816(2):480–486, 1999. 2.2.2, 5, 5.1.1, 5.1.1, 5.1.2

[222] Anne Schmitz, Amy Silder, Bryan Heiderscheit, Jane Mahoney, and Darryl G Thelen. Differences in lower-extremity muscular activation during walking between healthy older and young adults. *Journal of Electromyography and Kinesiology*, 19(6):1085–1091, 2009. 6.2.3, 6.11, 6.2.3

[223] ED Schomburg, N Petersen, I Barajon, and Hans Hultborn. Flexor reflex afferents reset the step cycle during fictive locomotion in the cat. *Experimental brain research*, 122(3):339–350, 1998. 5.3

[224] Stephen H Scott and David A Winter. Biomechanical model of the human foot: kinematics and kinetics during the stance phase of walking. *Journal of biomechanics*, 26(9):1091–1104, 1993. 6.1.1

[225] Justin E Seipel and Philip Holmes. Running in three dimensions: Analysis of a point-mass sprung-leg model. *The International Journal of Robotics Research*, 24(8):657–674, 2005. 2.2

[226] Keehong Seo, SeungYong Hyung, Byung Kwon Choi, Younbaek Lee, and Youngbo Shim. A new adaptive frequency oscillator for gait assistance. In *Robotics and Automation (ICRA), 2015 IEEE International Conference on*, pages 5565–5571. IEEE, 2015. 6

[227] André Seyfarth, Michael Günther, and Reinhard Blickhan. Stable operation of an elastic three-segment leg. *Biological cybernetics*, 84

(5):365–382, 2001. 4.1.1

[228] André Seyfarth, Hartmut Geyer, and Hugh Herr. Swing-leg retraction: a simple control model for stable running. *Journal of Experimental Biology*, 206(15):2547–2555, 2003. 2.3

[229] Charles Sherrington. *The integrative action of the nervous system*, volume 2. CUP Archive, 1906. 1.1, 2.1.3

[230] Charles Scott Sherrington. Flexion-reflex of the limb, crossed extension-reflex, and reflex stepping and standing. *The Journal of physiology*, 40(1-2):28–121, 1910. 2.1.3

[231] Erik Bruun Simonsen and Poul Dyhre-Poulsen. Amplitude of the human soleus h reflex during walking and running. *The Journal of Physiology*, 515(3):929–939, 1999. 1.2, 2.2.2, 2.1, 5, 5.1.1, 5.2.1

[232] Thomas Sinkjaer, JACOB B Andersen, and BIRGIT Larsen. Soleus stretch reflex modulation during gait in humans. *Journal of neurophysiology*, 76(2):1112–1120, 1996. 2.2.2, 5, 5.1.1, 5.1.1, 5.1.2

[233] Mikhail G Sirota, Gonzalo Viana Di Prisco, and Réjean Dubuc. Stimulation of the mesencephalic locomotor region elicits controlled swimming in semi-intact lampreys. *European Journal of Neuroscience*, 12(11):4081–4092, 2000. 2.1.2, 5.3

[234] Lizeth H Sloot, Josien C van den Noort, Marjolein M van der Krogt, Sjoerd M Bruijn, and Jaap Harlaar. Can treadmill perturbations evoke stretch reflexes in the calf muscles? *PloS one*, 10(12):e0144815, 2015. 2.2.2, 5, 5.1.1, 5.1.1, 5.1.2

[235] Seungmoon Song. Towards a hierarchical neuromuscular control model with reflex-based spinal control - study with a simple running model. In *The 16th International Symposium on Advanced Intelligent Systems*, pages 1358–1365, 2015. 4, 4.4

[236] Seungmoon Song and Hartmut Geyer. Computer simulations imply strength training as the only way to enhance elderly gait. *submitted*. 6.2

[237] Seungmoon Song and Hartmut Geyer. The energetic cost of adaptive feet in walking. In *Robotics and Biomimetics (ROBIO), 2011 IEEE International Conference on*, pages 1597–1602. IEEE, 2011. 6.1

[238] Seungmoon Song and Hartmut Geyer. Regulating speed and generating large speed transitions in a neuromuscular human walking model. In *Robotics and Automation (ICRA), 2012 IEEE International Conference on*, pages 511–516. IEEE, 2012. 4, 4.4, 5.3

[239] Seungmoon Song and Hartmut Geyer. Generalization of a muscle-reflex control model to 3d walking. In *Engineering in Medicine and Biology Society (EMBC), 2013 35th Annual International Conference of the IEEE*, pages 7463–7466. IEEE, 2013. 3

[240] Seungmoon Song and Hartmut Geyer. A neural circuitry that emphasizes spinal feedback generates diverse behaviours of human locomotion. *The Journal of physiology*, 2015. 3, 4, 5, 5.1.2, 5.3, 5.3, 6

[241] Seungmoon Song and Hartmut Geyer. Regulating speed in a neuromuscular human running model. In *Humanoid Robots (Humanoids), 2015 IEEE-RAS 15th International Conference on*, pages 217–222. IEEE, 2015. 4, 4.2.3, 4.4, 5.3

[242] Seungmoon Song and Hartmut Geyer. Evaluation of a neuromechanical walking control model using disturbance experiments. *Frontiers in Computational Neuroscience*, 11:15, 2017. 5

[243] Seungmoon Song, Ruta Desai, and Hartmut Geyer. Integration of an adaptive swing control into a neuromuscular human walking model. In *Engineering in Medicine and Biology Society (EMBC), 2013 35th Annual International Conference of the IEEE*, pages 4915–4918. IEEE, 2013. 6

[244] Seungmoon Song, Christopher LaMontagna, Steven H Collins, and Hartmut Geyer. The effect of foot compliance encoded in the windlass mechanism on the energetics of human walking. In *Engineering in Medicine and Biology Society (EMBC), 2013 35th Annual International Conference of the IEEE*, pages 3179–3182. IEEE, 2013. 6.1

[245] VP Stokes, C Andersson, and Hm Forssberg. Rotational and translational movement features of the pelvis and thorax during adult human locomotion. *Journal of Biomechanics*, 22(1):43–50, 1989. 4.2.3

[246] J B Sunders, Verne T Inman, and Howard D Eberhart. The major determinants in normal and pathological gait. *The journal of bone & joint surgery*, 35(3):543–558, 1953. 2.2.1

[247] Gentaro Taga. A model of the neuro-musculo-skeletal system for human locomotion. *Biological cybernetics*, 73(2):97–121, 1995. 1.1, 2.3, 2.2

[248] Gentaro Taga. A model of the neuro-musculo-skeletal system for anticipatory adjustment of human locomotion during obstacle avoidance. *Biological Cybernetics*, 78(1):9–17, 1998. 2.3, 2.2, 2.3.1

[249] Gentaro Taga, Yoko Yamaguchi, and Hiroshi Shimizu. Self-organized control of bipedal locomotion by neural oscillators in unpredictable environment. *Biological cybernetics*, 65(3):147–159, 1991. 2.3, 2.2, 5.3

[250] Patrick A Tansey and Peter J Briggs. Active and passive mechanisms in the control of heel supination. *Foot and ankle surgery*, 7(3):131–136, 2001. 6.1.1

[251] Nitish Thatte and Hartmut Geyer. Towards local reflexive control of a powered transfemoral prosthesis for robust amputee push and trip recovery. In *Intelligent Robots and Systems (IROS 2014), 2014 IEEE/RSJ International Conference on*, pages 2069–2074. IEEE, 2014. 6

[252] Nitish Thatte and Hartmut Geyer. Toward balance recovery with leg prostheses using neuromuscular model control. *IEEE Transactions on Biomedical Engineering*, 63(5):904–913, 2016. 6

[253] Nitish Thatte, Helei Duan, and Hartmut Geyer. A sample-efficient black-box optimizer to train policies for human-in-the-loop systems with user preferences. *IEEE Robotics and Automation Letters*, 2(2):993–1000, 2017. 6.3.5

[254] Darryl G Thelen and Frank C Anderson. Using computed muscle control to generate forward dynamic simulations of human walking from experimental data. *Journal of biomechanics*, 39(6):1107–1115, 2006. 3.5, 6.2.3, 6.15

[255] Darryl G Thelen, Frank C Anderson, and Scott L Delp. Generating dynamic simulations of movement using computed muscle control. *Journal of biomechanics*, 36(3):321–328, 2003. 3.2.2, 3.5

[256] Darryl G Thelen et al. Adjustment of muscle mechanics model parameters to simulate dynamic contractions in older adults. *Transactions-American Society Of Mechanical Engineers Journal Of Biomechanical Engineering*, 125(1):70–77, 2003. 6.2.1, 6.2.2, 6.3

[257] Matthew C Tresch and Anthony Jarc. The case for and against muscle synergies. *Current opinion in neurobiology*, 19(6):601–607, 2009. 2.1.4

[258] Brian R Umberger. Stance and swing phase costs in human walking. *Journal of The Royal Society Interface*, 7(50):1329–1340, 2010. 3.5, 4.2.1, 6.13

[259] Brian R Umberger, Karin GM Gerritsen, and Philip E Martin. A model of human muscle energy expenditure. *Computer methods in biomechanics and biomedical engineering*, 6(2):99–111, 2003. 3.5

[260] Junichi Urata, Koichi Nshiwaki, Yuto Nakanishi, Kei Okada, Satoshi Kagami, and Masayuki Inaba. Online walking pattern generation for push recovery and minimum delay to commanded change of direction and speed. In *Intelligent Robots and Systems (IROS), 2012 IEEE/RSJ International Conference on*, pages 3411–3416. IEEE, 2012. 6.3.1

[261] HWAA Van de Crommert, M Faist, W Berger, and J Duysens. Biceps femoris tendon jerk reflexes are enhanced at the end of the swing phase in humans. *Brain research*, 734(1):341–344, 1996. 5.1.1

[262] Herman Van Der Kooij and Robert J Peterka. Non-linear stimulus-response behavior of the human stance control system is predicted by optimization of a system with sensory and motor noise. *Journal of computational neuroscience*, 30(3):759–778, 2011. 3.3

[263] Marjolein M van der Krogt, Scott L Delp, and Michael H Schwartz. How robust is human gait to muscle weakness? *Gait & posture*, 36 (1):113–119, 2012. 6.2.1

[264] Nicolas Van der Noot, Luca Colasanto, Allan Barrea, Jesse van den Kieboom, Renaud Ronsse, and Auke J Ijspeert. Experimental validation of a bio-inspired controller for dynamic walking with a humanoid robot. In *Intelligent Robots and Systems (IROS), 2015 IEEE/RSJ International Conference on*, pages 393–400. IEEE, 2015. 6

[265] Nicolas Van der Noot, Auke J Ijspeert, and Renaud Ronsse. Biped gait controller for large speed variations, combining reflexes and a central pattern generator in a neuromuscular model. In *Robotics and Automation (ICRA), 2015 IEEE International Conference on*, pages 6267–6274. IEEE, 2015. 5.3

[266] Wietse van Dijk and Herman van der Kooij. Optimization of human walking for exoskeletal support. In *Rehabilitation Robotics (ICORR), 2013 IEEE International Conference on*, pages 1–6. IEEE, 2013. 6

[267] JL Van Leeuwen. Muscle function in locomotion. *Mechanics of animal locomotion*, 11:191–249, 1992. 3.2.2

[268] Arthur J van Soest and Maarten F Bobbert. The contribution of muscle properties in the control of explosive movements. *Biological cybernetics*, 69(3):195–204, 1993. 3.2.2

[269] Bart MH Van Wezel, Frans AM Ottenhoff, and Jacques Duysens. Dynamic control of location-specific information in tactile cutaneous reflexes from the foot during human walking. *The Journal of neuroscience*, 17(10):3804–3814, 1997. 2.2.2, 5.2.2

[270] Dario Villarreal, David Quintero, and Robert Gregg. A perturbation mechanism for investigations of phase-dependent behavior in human locomotion. *Access, IEEE*, 4:893–904, 2016. 2.2.2, 5.1.1

[271] JJ Visser, JE Hoogkamer, MF Bobbert, and PA Huijing. Length and moment arm of human leg muscles as a function of knee and hip-joint angles. *European journal of applied physiology and occupational physiology*, 61(5-6):453–460, 1990. 3.2.3

[272] Jack M Wang, David J Fleet, and Aaron Hertzmann. Optimizing walking controllers. *ACM Transactions on Graphics (TOG)*, 28(5):168, 2009. 3.6

[273] Jack M Wang, Samuel R Hamner, Scott L Delp, and Vladlen Koltun. Optimizing locomotion controllers using biologically-based actuators and objectives. *ACM Trans. Graph.*, 31(4):25, 2012. 2.3.2, 6

[274] David A Winter. Human balance and posture control during standing and walking. *Gait & posture*, 3(4):193–214, 1995. 2.2.1, 2.3

[275] David A Winter. *Biomechanics and motor control of human movement*. John Wiley & Sons, 2009. 5.1.2

[276] Jack M Winters. Hill-based muscle models: a systems engineering perspective. In *Multiple muscle systems*, pages 69–93. Springer, 1990. 3.2.2

[277] Jack M Winters and Lawrence Stark. Analysis of fundamental human movement patterns through the use of in-depth antagonistic muscle models. *IEEE transactions on biomedical engineering*, (10):826–839, 1985. 3.2.2

[278] Tishya AL Wren, K Patrick Do, Susan A Rethlefsen, and Bitte Healy. Cross-correlation as a method for comparing dynamic electromyography signals during gait. *Journal of biomechanics*, 39(14):2714–2718, 2006. 4.3, 4.2.1

[279] Albert Wu and Hartmut Geyer. The 3-d spring–mass model reveals a time-based deadbeat control for highly robust running and steering in uncertain environments. *IEEE Transactions on Robotics*, 29(5):1114–1124, 2013. 4.1.2

[280] Amy R Wu, Florin Dzeladini, Tycho JH Brug, Federica Tamburella, Nevio L Tagliamonte, Edwin van Asseldonk, Herman van der Kooij, and Auke J Ijspeert. A versatile neuromuscular exoskeleton controller for gait assistance: A preliminary study on spinal cord injury patients. In *Wearable Robotics: Challenges and Trends*, pages 163–167. Springer, 2017. 6

[281] GT Yamaguchi, AGU Sawa, DW Moran, MJ Fessler, and JM Winters. A survey of human musculotendon actuator parameters. *Multiple muscle systems: Biomechanics and movement organization*, pages 717–773, 1990. 3.2.2

[282] Taiga Yamasaki, Taishin Nomura, and Shunsuke Sato. Possible functional roles of phase resetting during walking. *Biological cybernetics*, 88(6):468–496, 2003. 5.3

[283] JAYNIE F Yang and RICHARD B Stein. Phase-dependent reflex reversal in human leg muscles during walking. *Journal of Neurophysiology*, 63(5):1109–1117, 1990. 2.1

[284] JF Yang, RB Stein, and KB James. Contribution of peripheral afferents to the activation of the soleus muscle during walking in humans. *Experimental Brain Research*, 87(3):679–687, 1991. 2.2.2, 2.1, 5.1.1, 5.1.3, 5.3

[285] KangKang Yin, Kevin Loken, and Michiel van de Panne. Simbicon: Simple biped locomotion control. *ACM Transactions on Graphics (TOG)*, 26(3):105(1–10), 2007. 4.1.2

[286] Riadh Zaier and Shinji Kanda. Adaptive locomotion controller and reflex system for humanoid robots. In *Intelligent Robots and Systems, 2008. IROS 2008. IEEE/RSJ International Conference on*, pages 2492–2497. IEEE, 2008. 6.3.1

[287] MY Zarrugh, FN Todd, and HJ Ralston. Optimization of energy expenditure during level walking. *European Journal of Applied Physiology and Occupational Physiology*, 33(4):293–306, 1974. 1.2, 2.2.1, 6.1.4

[288] E Paul Zehr and Richard B Stein. What functions do reflexes serve during human locomotion? *Progress in neurobiology*, 58(2):185–205, 1999. 2.2.2

[289] Li-Qun Zhang, Haiyun Huang, James A Sliwa, and W Zev Rymer. System identification of tendon reflex dynamics. *Rehabilitation Engineering, IEEE Transactions on*, 7(2):193–203, 1999. 5.1.2